

**Study of Surface Cracks in a Simulated Solid Rocket  
Propellant Grain with an Internal Star Perforation**

by

Lei Wang

Dissertation submitted to the Faculty of the  
Virginia Polytechnic Institute and State University  
in partial fulfillment of the requirements for the degree of

DOCTOR OF PHILOSOPHY  
in  
Engineering Mechanics

APPROVED:



\_\_\_\_\_  
C.W. Smith, Chairman



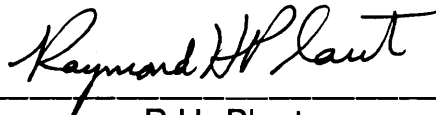
\_\_\_\_\_  
D. Post



\_\_\_\_\_  
L. Meirovitch



\_\_\_\_\_  
D.H. Morris



\_\_\_\_\_  
R.H. Plaut

December, 1992  
Blacksburg, Virginia

**Study of Surface Cracks in a Simulated Solid Rocket  
Propellant Grain with an Internal Perforation**

by

Lei Wang

C.W. Smith, Chairman

Engineering Science and Mechanics

(Abstract)

Solid propellant research has mainly been directed towards more accurate characterization of the propellant material nature and more reliable structural analysis of the grain. Internal star grain design is among the most popular grain shapes that are used in today's propulsion system. Due to its complex geometry, stress concentrations are inevitably present around the highly curved area. Furthermore, this geometric effect together with various loading conditions throughout the grain's service life actually causes numerous defects inside its body. However, little is known concerning the three-dimensional fracture mechanism of the surface cracks which are the most common defects detected in the real rocket motor grain.

After a brief evaluation of the current status of solid propellant research, stress analysis of a star grain model under internal pressure was performed by both photoelastic experiments and finite element calculations. These results illustrated the stress concentration effect around the star finger tip in addition to the

global stress distribution across the whole section. Meanwhile, the deformation of the grain's outer surface was also obtained from the finite element results.

A series of photoelastic experiments was conducted on cracked specimens with surface flaws emanating both on and off the axis of symmetry starting from the star finger tip. For the symmetric crack problem, cracks with different depths were intensively studied and the three-dimensional stress intensity factor (SIF) distribution was obtained for each test. These experimental data were further used to construct three analytical models, the "equivalent" radius model, the weight function model and the notch-root crack model, to expand the application range of the experimental data base so that a symmetric crack's SIF distribution with an arbitrary depth can be predicted.

Moreover, surface cracks initiated off the axis of symmetry were also investigated by considering two off-axis angles. The crack shape and propagation path were achieved through a series of experiments and two methods were developed to effectively predict the possible crack growth path under sufficient pressure. The SIF distribution around the crack border was obtained for different off-axis angles and the factors that might influence the distributions were addressed based on the comparisons between the symmetric and asymmetric cracks, and the asymmetric cracks with different geometries.

## Acknowledgment

The author wishes to express his sincere gratitude and respect to his major advisor, Prof. C.W. Smith, for his guidance, support and understanding throughout the years. Prof. Smith's spectacular and unique laughter that can be heard miles away has made the author believe how enjoyable the research and life could be. His rigorous attitude towards research is believed to be influential to the author's future professional career. Prof. Smith's fatherly care about the author's non-technical matters is also greatly appreciated.

Many thanks should go to Dr. Daniel Post whose constant encouragement and concern have inspired the author with a positive attitude towards scientific exploration. His life philosophy and mind of creativity are believed to be beneficial to the author not only in the past, at present, but also in the future.

The author is also grateful to:

- His committee members, Dr. L. Meirovitch, Dr. D.H. Morris and Dr. R.H. Plaut for their participation and valuable suggestions on the dissertation.

- Dr. C.T. Liu for his valuable suggestions and support.

- His former and present lab partners, Dr. C.W. Chang, Dr. M. Rezvani, Mr. C.C. Chang, Mr. Hervé Mouille and Mr. Martin L. Tanaka for their cooperation and friendship.

- Doris Smith and Frieda Post for their encouragement and concern.

- His friends, Dr. Shih-Yung Lin, Dr. Jau-Je Wu, Dr. Peter Ifju, Dr. Ray Boeman, Dr. Bongtae Han, Dr. Joosik Lee, M.C. Li, Jerry Shyy, Tsu-Sheng Chang, Tseng-Hsing Hsu, Kuen Tat Teh, Lily Lin, Kin Shum, Joan Shen, Yan Wang, Qing Shao, Jun Liu, and Jia Li for all the wonderful time that was shared together.

- Phillips Laboratory, AFMC for financial support.

Special appreciation ought to be passed to the author's parents, Pei-fang Zhu and Zheng-guo Wang, sister and brother-in-law, Qin Wang and Yao-gui Du, brother, Lance F. Wang, whose love and understanding are the most precious treasure that anyone could possibly have in the whole world.

This dissertation, as a small part of the author's gratitude, is dedicated to all the people who have helped and cared about him throughout the years. They have made this dissertation possible.

# Table of Contents

1.0 Introduction.....	1
1.1 Propellant Fundamentals .....	1
1.2 Propellant Evaluation and Testing.....	5
1.3 Design and Testing of Solid Propellant Grain.....	8
1.4 Motivations and Objectives of the Present Research.....	12
2.0 Stress Analysis of the Internal Star Grain .....	18
2.1 Introduction to the Star-Shaped Grain.....	18
2.2 Specimen Description and Preparation.....	23
2.3 Stress Analysis of the Motor Grain.....	29
2.3.1 Experimental Stress Analysis.....	29
2.3.2 Finite Element Stress Analysis.....	36
3.0 Stress Intensity Factors (SIF's) Prediction for Symmetric Surface Cracks .....	58
3.1 Problem Definition .....	58
3.2 Experimental Procedure and Analyzed Results.....	59
3.3 "Equivalent" Radius Model.....	66
3.4 Weight Function Model .....	75

3.5 Notch-Root Crack Model .....	84
3.6 Summary.....	90
4.0 Off-Axis Crack Problem.....	94
4.1 Problem Definition .....	94
4.2 Experimental Procedure and Data Extraction .....	98
4.3 Crack Propagation Characteristics.....	101
4.4 SIF Determination for Off-Axis Cracks.....	116
5.0 Closure.....	126
5.1 Summary.....	126
5.2 Recommendations and Future Work.....	131
Appendix A.....	135
Appendix B.....	139
References.....	143
Vita.....	152

# List of Figures

Fig.1.1 Basic elements of solid and liquid propellant systems (2) .....	3
Fig.1.2 Typical solid propellant grain design process (25).....	10
Fig.1.3 Various grain configurations (28).....	14
Fig.2.1 Solid rocket with internal star grain (26).....	19
Fig.2.2 Classification of grains according to thrust-time profile (28).....	20
Fig.2.3 Star grain geometry definition.....	21
Fig.2.4 Geometry of the tested internal star grain model.....	24
Fig.2.5 Prepared internal star grain model.....	28
Fig.2.6 Isochromatic fringe pattern in a transverse slice of the propellant model subjected to internal pressure.....	31
Fig.2.7 $\sigma_1$ , $\sigma_2$ and $\tau_{\max}$ variations along the inner periphery of the star grain model under a 47.4kPa (6.9psi) pressure .....	33
Fig.2.8 Local coordinate system along the inner boundary of the grain model.....	34
Fig.2.9 Boundary conditions used in FEM model.....	38
Fig.2.10 Finite element mesh for stress analysis of the uncracked grain model subjected to internal pressure.....	40



Fig.2.11 $\sigma_x$ contour map of the pressurized uncracked grain model by FEM analysis.....	42
Fig.2.12 $\sigma_y$ contour map of the pressurized uncracked grain model by FEM analysis.....	43
Fig.2.13 $\tau_{xy}$ contour map of the pressurized uncracked grain model by FEM analysis.....	44
Fig.2.14 Comparison of $\sigma_1$ variation between experimental and FEM analysis along the inner periphery of the star grain model under a 47.4kPa (6.9psi) pressure.....	45
Fig.2.15 Comparison of $\sigma_1$ and $\sigma_2$ variations between FEM results of the internal star grain and relevant Lamé solution to the circular cylinder along the axis of symmetry.....	48
Fig.2.16 Comparison of the maximum shear stress along the axis of symmetry between the FEM data and experimental results.....	50
Fig.2.17 Force balance diagram of the internal star grain model.....	51
Fig.2.18 Outer surface deformation of the grain model subjected to internal pressure.....	53
Fig.2.19 Refined finite element mesh for stress analysis of an uncracked star-shaped cylinder section under internal pressure.....	54
Fig.2.20 Comparison of the principal stress variations along the axis of symmetry by using two sets of meshes	

shown in figures 2.10 and 2.19.....	56
Fig.3.1 Internal star grain model containing a surface crack emanating from the star finger tip along the axis of symmetry.....	60
Fig.3.2 Fixtures for making a symmetric crack.....	62
Fig.3.3 Schematic demonstration of the slice-cutting process.....	63
Fig.3.4 Analyzed results showing SIF distributions for symmetric cracks with different depths.....	64
Fig.3.5 Definition of the "equivalent" circular cylinder.....	68
Fig.3.6 Geometry used by Newman and Raju (49).....	70
Fig.3.7 Comparison of SIF distributions of deep surface cracks in the internal star cylinder and the "equivalent" circular cylinder.....	72
Fig.3.8 Comparison of SIF distributions of moderate depth surface cracks in the internal star cylinder and the "equivalent" circular cylinder.....	73
Fig.3.9 Ring specimen with a radial crack used in constructing the weight function.....	79
Fig.3.10 Variation of the correction function, $f(a)$ , used in the weight function model.....	85
Fig.3.11 Geometry of a small semi-elliptical notch-root crack used by Murakami et. al. (53).....	87
Fig.4.1 Misaligned crack propagation path from the star finger tip.....	95

Fig.4.2 Definition of the off-axis crack problem.....	97
Fig.4.3 Fixtures for making off-axis cracks.....	99
Fig.4.4 Isochromatic fringe pattern of a slice cut from the internal star grain model with an off-axis crack.....	102
Fig.4.5 Off-axis cracks' mid-points propagation paths under internal pressure loading.....	104
Fig.4.6 Comparison of a 30° crack propagation path between the experiment and predictions.....	109
Fig.4.7 Off-axis crack shape and definitions of the geometric parameters.....	112
Fig.4.8 Normalized SIF distributions for three 30° off-axis cracks.....	121
Fig.4.9 Normalized SIF distributions for two 45° off-axis cracks.....	122
Fig.4.10 Comparison of crack shape and location between the two penetrated cracks, E2 and E5.....	125
Fig.A.1 Near-tip general problem geometry and notations.....	136
Fig.B.1 Geometry used in the deformation analysis.....	140

# List of Tables

Table 2.1 Material properties of PLM-9 provided by .....	25
Table 3.1 Tested symmetric crack geometries.....	65
Table 3.2 Comparison between $K_{ex}$ and $K_{wt}$ without correction.....	82
Table 3.3 Comparison of SIF's from the experiments and the notch-root crack model at the mid-point of the surface cracks.....	89
Table 4.1 Geometric parameters of the off-axis cracks.....	114
Table 4.2 Linear zones and SIF values for three 30° off-axis cracks.....	119
Table 4.3 Linear zones and SIF values for two 45° off-axis cracks.....	120

# Chapter 1: Introduction

## **1.1 *Propellant Fundamentals***

The original use of propellants can be dated back to several hundred years ago when the Chinese first designed the so-called "fire-arrows" (1) in their warfare to increase the effective range of the arrows. However, later developments in propellants were impeded by several undesirable characteristics of the material nature, among which were low thrust, accompanying flash and smoke during firing and hygroscopicity (2). It was only after Vieille first proved the effectiveness of nitrocellulose which was mainly used in the early single-base propellants and Nobel further introduced nitrocellulose-nitroglycerin, or double-base propellants, did the research on propellants become practical. Modern propellant studies were initiated around World War II, and after the Germans had launched their V-2 liquid propellant missile to London, the whole world started to be aware of the importance of propellants to the future. In fact, the present use of propellants has been broadened to not only the military applications, but also commercial operations,

such as satellite communications, outer-space explorations, etc.

The most significant difference between propellants and regular fuels is that the burning of propellants does not require the presence of air because the chemical compounds inside the propellants, called oxidizers, serve as the source of oxygen and the propellant is considered as a system for converting the potential energy inside the ingredients into the kinetic energy of the whole rocket. Technically speaking, propellants can be classified in several different ways, among which the separation of solid propellants from liquid propellants is the most popular one. Liquid propellant has the advantage of providing large and varying thrust through the controllable mixing process of the fuel and oxidizer. However, because of the necessity of precise control, a liquid propellant system usually requires a more complex mechanism to operate and a larger number of mechanical components compared with the solid propellant system (figure 1.1). Also, the liquid propellant system is not quite suitable for long-term storage because of the tedious assembling and disassembling processes. Solid propellant, on the other hand, is credited for its advantages of easy handling, endurance for long time storage, and relatively simple operating system. In the present research, attention will be focused on solid propellants.

Nowadays, solid propellants can be generally categorized into three types: double-base, composite and composite double-base

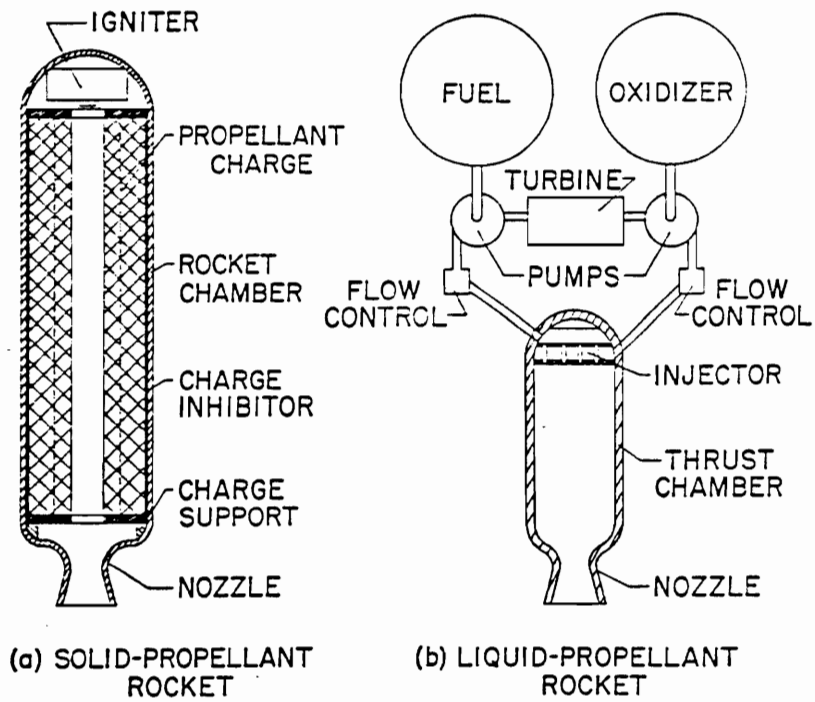


Fig.1.1: Basic elements of solid and liquid propellant systems  
(2).

propellants. Double-base propellant is basically a homogeneous mixture of two explosives which most commonly are nitroglycerin in nitrocellulose. In this type of propellant, the major ingredients serve to be not only the fuel, but also the oxidizer and binder. Because of the hazardous nature of the material itself, extreme care has to be taken during the manufacturing process. Composite propellants, on the other hand, are heterogeneous mixtures of metal powder (usually aluminum) serving as the fuel, fine ground crystalline oxidizer (usually potassium perchlorate,  $\text{KClO}_4$ , ammonium perchlorate,  $\text{NH}_4\text{ClO}_4$ , and ammonium nitrate,  $\text{NH}_4\text{NO}_3$ ) and polymeric binder (such as polystyrene, urea-aldehydes and polybutadiene). Since the first appearance of composite rockets around 1945, extensive research has been performed towards better characterizing and further developing various kinds of composite propellants which are playing a major role in current propellant applications. Composite double-base propellants come from a combination of the first two kinds of propellants with crystalline oxidizer and metal fuel embedded in the matrix of the double-base propellant material, which makes the manufacturing process more hazardous than that of "pure" composite propellants.

After the solid propellant material is extruded, cast or molded into a shaped mass, the so-called solid propellant grain is formed. The grain is usually bonded to a stiff case and serves as not only the fuel but also part of the whole rocket structure. Thus, it is very important to insure the quality control so as to keep the integrity of



the grain during manufacturing, processing, transportation, storage and operational stages. Accordingly, to account for the functions and geometries of the grain, studies should emphasize not only the material characterization but also the structural analysis.

## ***1.2 Propellant Evaluation and Testing***

Facing various applications of different rockets and so many factors that can alter the propellants' behavior, the research on propellant evaluation and testing has been and still will be a broad field to be explored. Generally speaking, propellant studies can be divided into two branches, chemistry and mechanics, although interactions between the two are inevitable. From a chemical point of view, changing the propellant composition can alter the reactions among the constituents and further influence the performance of the whole rocket. Oxidizers, fuels and binders are certainly the elements that can be manipulated for different applications, such as the uses of higher energy, low density and toxic propellants for upper-stage propulsion, while lower energy, denser and non-toxic propellants are used for early stage launching (3). Limitations in chemical reactions, hazards and difficulties in manufacturing and processing, mechanical integrity of the formed grain (e.g. aging and

failure endurance, etc.), desired burning rate or time, thrust, and the production and maintenance cost are all crucial factors in selecting a proper kind of propellant material.

Once the propellant is produced, the next step is to test its physical and mechanical properties, among which are tensile, shear, and compressive strength and moduli, stress-strain relationship, hardness, creep compliance, stress relaxation modulus, temperature dependency, loading rate sensitivity, damage endurance and failure mechanism. From the material point of view, one of the major concerns is to examine the characteristics of the cured binder due to its critical role in influencing the mechanical behavior of the whole propellant. No matter whether it is double-base, or composite, or composite modified double-base propellant, the elastomers binder content, in each case, is large enough to cause the whole mixture to possess significant time-dependent properties. The determination of the propellant's stress-strain constitutive relationships is believed to be essential in material characterization, and three factors, temperature, strain rate and pressure, have been proved to have significant effects in altering the propellant's mechanical behavior. The reality of the propellants experiencing temperature change, strain rate upsurge and pressure alternation from initial manufacturing until final firing has motivated a long-term effort (4-12) in quantifying the effects from the three factors. In these studies, different testing methods and conditions were applied to various kinds of propellants, which has provided a valuable

experimental data base for propellant grain design. Meanwhile, mechanical computations, such as the adoption of the finite element method, combined with both linear and nonlinear viscoelastic theories have pushed the analytical developments to a more comprehensive and practical level.

Upon the completion of the first stage material characterizations and engineering analysis, which is really a direct application of the test data and developed theories, the next step is to examine the failure mechanism of the propellant material and develop certain quality control procedures. In this field, damage mechanics, fracture mechanics and statistical analysis (13-18) have been proposed to evaluate the factors influencing the failure of propellants, such as the time, the instantaneous state of stress, specimen geometry, damage history, and the composition of the propellant material. Certain crack propagation laws, service life prediction procedures, stress intensity factor (SIF) measurements and failure envelopes have also been presented based on the accomplished material characterizations. It is noted that, although the analysis has provided enormous test data, empirical formulations and theoretical assessment, further efforts ought to be made towards the following directions which can considerably extend the application of the failure analysis. These include:

- 1) More accurate and general material characterization
- 2) Further considerations on complex state of stresses

- 3) Evaluations of both material and geometry nonlinearities
- 4) Material-independent failure envelope generation
- 5) Expanded experimental data base, especially on the real-shaped grains under the conditions of various aging history, temperature loading and loading rates.

It is worth mentioning that, in the development of analytical models for predicting solid propellants' failure, Schapery's theory and its applications (19-24) have found encouraging success in correlating the theoretical predictions to the test data. The presented micro structural model based on linear and nonlinear viscoelasticity theories is believed to be one of the most promising and practical formulations so far, despite its restrictions on particle shape, crack locations and orientations.

### ***1.3 Design and Testing of Solid Propellant Grain***

Once solid propellant grain is shaped, it serves as not only the fuel to provide propulsive force for the rocket, but also a structural element inside the whole rocket system. Due to this unique dual-purpose characteristic, solid propellant grain design should not be limited to the research of the propellant material itself, but its

interactions with other relevant structural components ought to be considered. Although the efforts of formulating a comprehensive and practical design package started over thirty years ago, it was not until recent rapid developments in computing techniques and equipment, especially the access to large commercial computing packages and high speed, high accuracy super-computers, has the design process become a quicker and more realistic step. Recent progress in this area has been well documented in a lecture series (25-27) organized by the Advisory Group for Aerospace Research and Development (AGARD) under NATO, and a typical propellant grain design procedure is illustrated in figure 1.2 (25).

Like any other design, the selection of a specific solid propellant grain has to satisfy various requirements and fulfill different tasks. The demands of providing higher thrust, longer burning time, better aging endurance, easier manufacturing and lower-cost propellant grains have fundamentally set up the final goals of the present research. Generally speaking, the propellant design can be divided into two stages: preliminary design and secondary design. In each stage, one also has to take into account both the ballistic design and the structural design requirements. As to the preliminary design, evaluation of the requirements, selection of propellant material and determination of the grain configuration are nearly accomplished, while the detailed design optimizations, propellant characterization and tailoring, and analysis of the design are expected to be polished in the second stage. The ballistic design

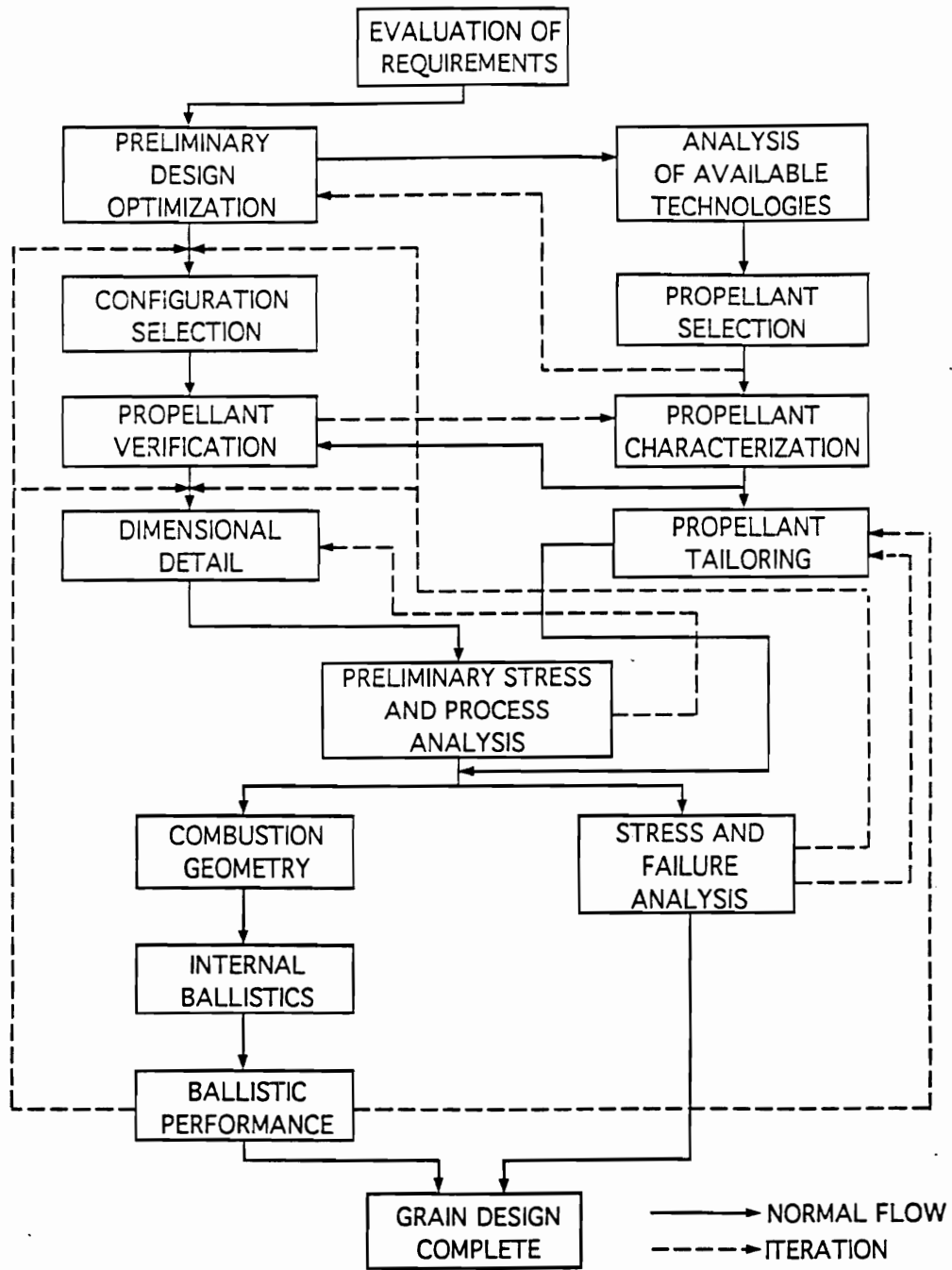


Fig.1.2: Typical solid propellant grain design process (25).

is more or less related to the propellant grain itself and usually involves the considerations of physical constraints on the motor, the total impulse requirement, the environmental limits, etc. (27). In this step, the limits imposed on storage temperature and operating parameters, such as ignition time, peak pressure, and specified total impulse, are significantly influenced by the propellant material and the grain geometry. In order to achieve a quick selection of the propellant grain based on some essential requirements, an enormous amount of work has been performed on testing different types of propellant materials and grain configurations, and categorized information (26,28) can provide excellent insight into the mechanical characteristics of the propellants and indispensable guidelines for engineering design.

In structural design, the integrity of the propellant grain itself and its interactions with other components, such as the liner, the motor case, the ignitor and the nozzle, are important features to be considered. Various loading conditions including thermal loads, acceleration loads, vibration loads and ignition pressurization can be imposed on the propellant grain throughout its service life, and measurements on the loading endurance, deformation and even failure mode are critical for quality control of the propellant grain. Extensive research (29-36) has been conducted towards better understanding of the grain behavior by using experimental and numerical methods, and the analysis has provided valuable information on stress (and/or strain) distributions inside the grain,

which serves as one of the critical design inputs by highlighting the stress (and/or strain) concentration areas. As the requirements for optimal and accurate assessment of a specified propellant grain were advanced, failure analysis (37,38) and detection inevitably came into play and the strain energy release rate was adopted in predicting critical conditions of the existing flaws inside the motor grain. Recently developed damage evaluation techniques (39, 40) undoubtedly provided crucial knowledge for safety margin determination and service life evaluation.

One thing that needs to be pointed out is that the ballistic design and structural design of the propellant grain are not performed separately, and the designer should keep an overall point of view at all time. Usually, the ballistic requirements are studied initially and a certain design scheme is presented. Then the structural design is used to evaluate the integrity of the initial design and conduct necessary changes to improve the structural endurance of the whole motor without significantly changing the original ballistic design.

#### ***1.4 Motivations and Objectives of the Present Research***



It has been mentioned that there is a variety of propellant grain geometries (figure 1.3) designed for progressive, regressive, dual level and neutral burning purposes. Among all these designs, the internal star-shape configuration has been proved to be one of the most popular choices, especially in neutral burning grain applications. One of the most important practical examples is the selection of star-shaped grain in the well-known Minuteman strategic missile propulsion system. However, as the specified ballistic requirements are fulfilled by the use of star-shaped grain, the complex geometry inevitably brings about the inherent weakness of stress concentrations around the finger tips of the internal star which could be multiples of those occurring in a simple thick-wall cylinder. Hence, accurate stress analysis is necessary to provide reliable guidelines for optimizing the grain design to meet different ballistic and structural requirements, such as generating maximum total impulse within a certain burning time, eliminating any susceptibility of the propellant grain to mechanical failure and so on. Earlier work (41-44) showed some encouraging efforts in optimizing star grain configuration based on loading conditions and the tradeoffs among volumetric loading, silver fraction (see page 22) and neutrality. Seven independent variables used to define the geometry of a specific internal star grain were shown to play their own roles in altering the grain's ballistic and structural behavior.

In the next chapter, stress analysis of an internal star grain model will be performed by using the finite element method (FEM).

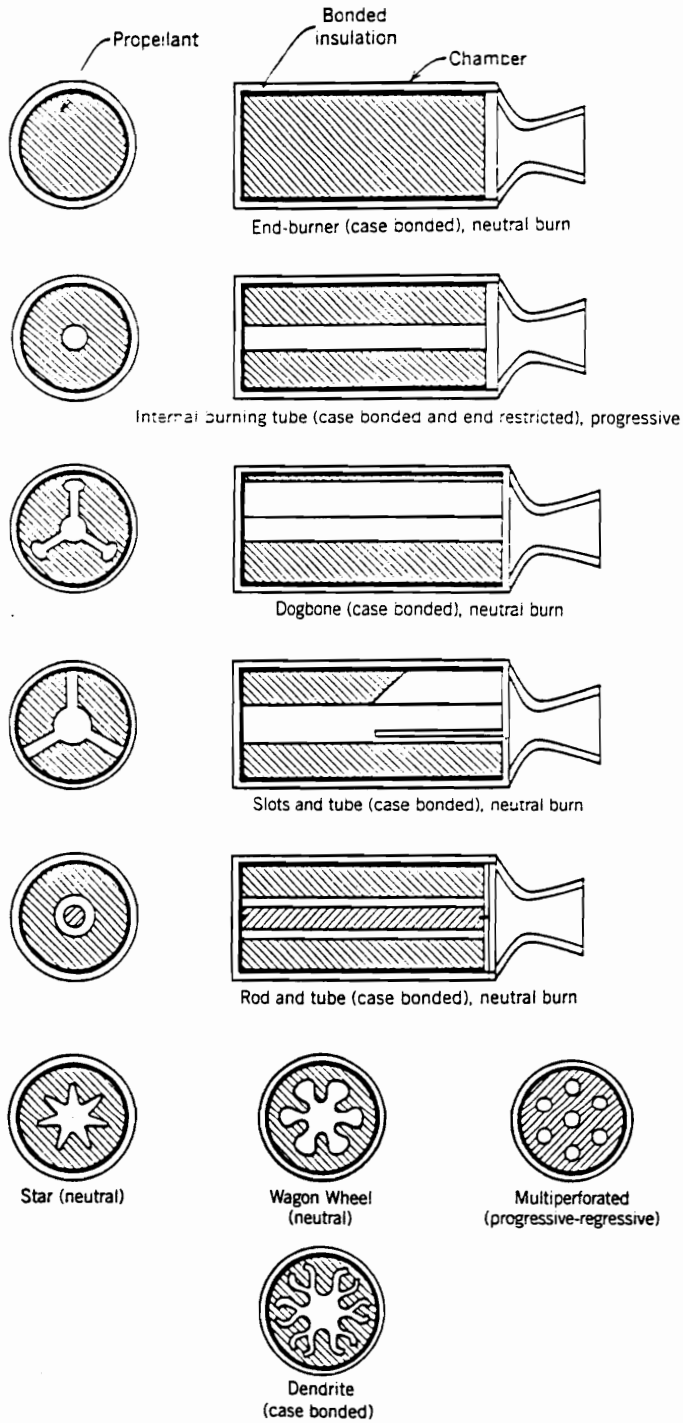


Fig.1.3: Various grain configurations (28).

The results will not only demonstrate the stress concentration effect due to the presence of the star, which can be used as one of the informative inputs in a conventional design process, but will be used further in the fracture analysis.

As was pointed out above, earlier research on solid propellant grain has been focused on non-damage design, or at most two-dimensional fracture analysis. In reality, numerous cracks and defects, especially surface flaws, have been detected inside the grain as a result of manufacture, transportation, storage and operation processes. These imperfections enlarge the designed burning area, provide a progressive burning rate to destroy the neutrality of the grain, shorten the designed burning time, or even lead to the catastrophic failure of the whole structure. Hence, it becomes imperative to further push the propellant research into the field where the adoption of fracture mechanics concepts is an inevitable trend.

However, due to the complex geometry of the internal star grain, little is known of the three-dimensional effects accompanying the surface flaws which are one of the major types of cracks inside the grain. Meanwhile, the non-uniform stress distribution field will further complicate the problem, especially for the cracks off the symmetric axis of the grain. The present research is motivated to fill this unknown void so as to reduce the uncertainty in structural integrity assessment and provide a cost

effective approach to rational analysis and design of the motor grain.

Generally speaking, both the propellant material and the grain shape are crucial in determining a motor grain's final performance. Hence, in order to accurately assess the surface cracks' behavior, comprehensive research should be directed towards these two directions, i.e. trying to characterize the failure mechanism of the grain with a complex geometry by considering the material's viscoelastic nature. Up to now, the failure analysis of viscoelastic propellant material is still in a stage where specimens with simple geometries are tested and the experiments are usually designed to simulate the stress conditions in the real grain geometry, such as the biaxial and triaxial tensile tests. Fortunately, experiments have shown that when the propellant is under hydrostatic pressure, which is approximately the case when it is fired, the material tends to behave pseudo-elastically. This observation opens the door to separately consider the viscoelastic material behavior and the complex geometric effect of the grain. In the present research, geometric effects are to be emphasized and surface cracks at different locations will be considered. Stress intensity factors (SIF's) around the border of the cracks are to be extracted to reveal the three-dimensional effects, and the crack propagation path will also be determined.

Based on the experimental data base, analytical and numerical

models will be developed to serve as a practical rationale for wider applications, and at the same time, the advantages and shortcomings of these models will be addressed.

## Chapter 2: Stress Analysis of the Internal Star Grain

### ***2.1 Introduction to the Star-Shaped Grain***

The term star-shaped grain comes from the shape of the grain's internal perforation. Usually, the cross-section of the star-shaped grain is kept constant along the motor's longitudinal direction, while some slight evolvement may be present for manufacturing ease (figure 2.1). One of the most important features of the internal star grain is its neutrality, for the thrust generated by the burning of the grain is kept constant or very close to constant throughout its operation (figure 2.2), which is controlled by the designed constant burning area as the grain burns.

There are seven independent geometric parameters that define the configuration of a star grain (figure 2.3), and the most common ones are:

R: grain outer radius

N: number of star points

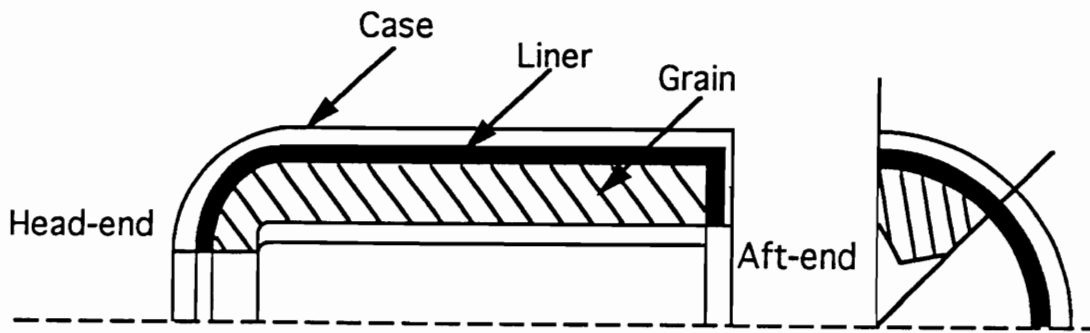


Fig.2.1: Solid rocket with internal star grain (26).

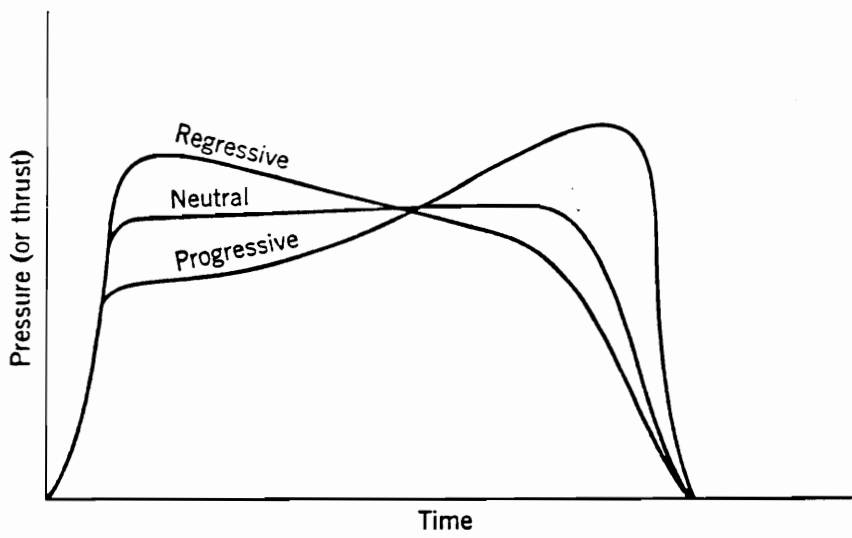


Fig.2.2: Classification of grains according to thrust-time profile (28).



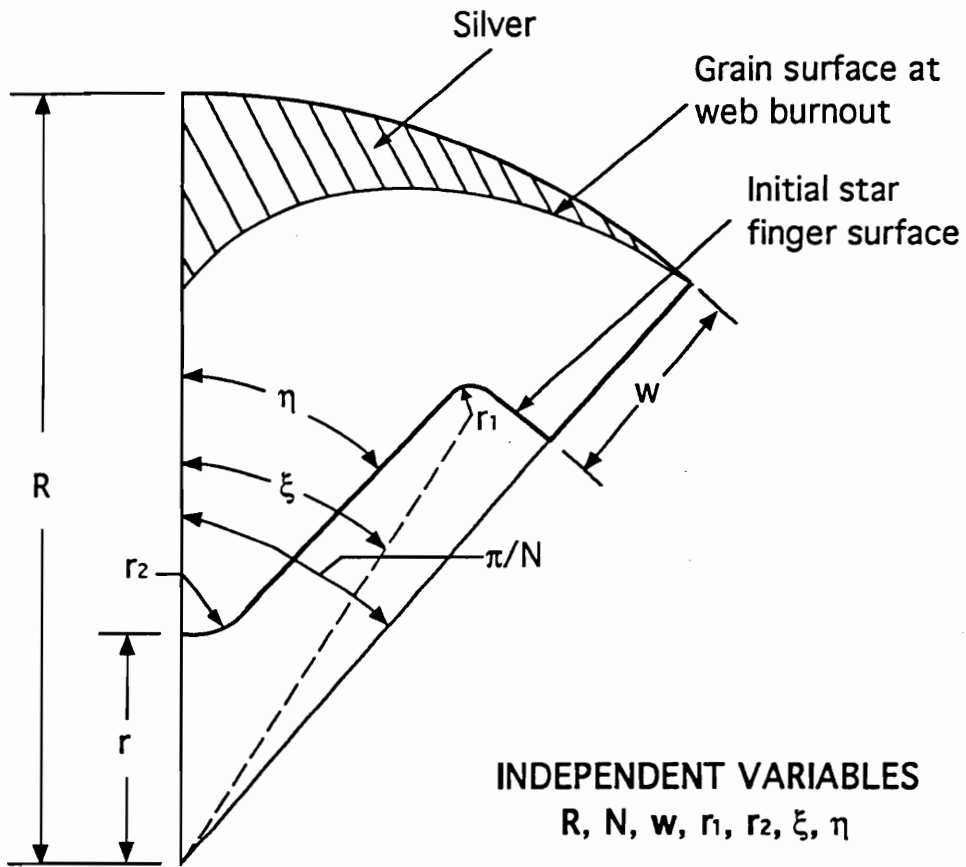


Fig.2.3: Star grain geometry definition.

w: web thickness

$r_1$ : fillet radius

$r_2$ : cusp radius

$\xi$ : star angle (figure 2.3)

$\eta$ : star angle (figure 2.3)

From these geometric factors, some other important quality indexes can be derived:

$V_f$ : silver volume

$V_m$ : chamber volume

$V_p$ : initial propellant volume

$\frac{V_f}{V_p}$ : silver fraction

$\frac{V_p}{V_m}$ : loading density

The term silver, as is indicated in figure 2.3, is the unburned remaining part of the propellant at the time of web burnout. According to the current trend, the effective use of the propellant material and demands for higher thrust have made the silver fraction and loading density two very important design elements. The tradeoffs among higher thrust, less silver fraction and lower stress concentration are becoming decisive factors in determining a

propellant grain's geometry.

In the early days, design charts were plotted by taking the geometric parameters that were mentioned earlier and the targeting parameters, such as thrust, loading density, silver fraction and stress concentration, as independent and dependent variables respectively and selecting the proper design criteria for different purposes. Nowadays, rapid developments in computer capabilities have made the design process more accurate, comprehensive, flexible and efficient. Some two-dimensional and three-dimensional codes have been written based on various design considerations, most of which, however, are essentially non-damage analyses. Nevertheless, these design methods have effectively, if not completely, provided guidelines in determining the proper geometry of the internal star grain with a certain safety margin in the real situations.

## ***2.2 Specimen Description and Preparation***

In the present research, the internal star grain model (figure 2.4) is a 304.8mm (12") long cylinder with six star points. Its length is intentionally made large enough to eliminate the end effect, which not only simulates the real situation, but allows an

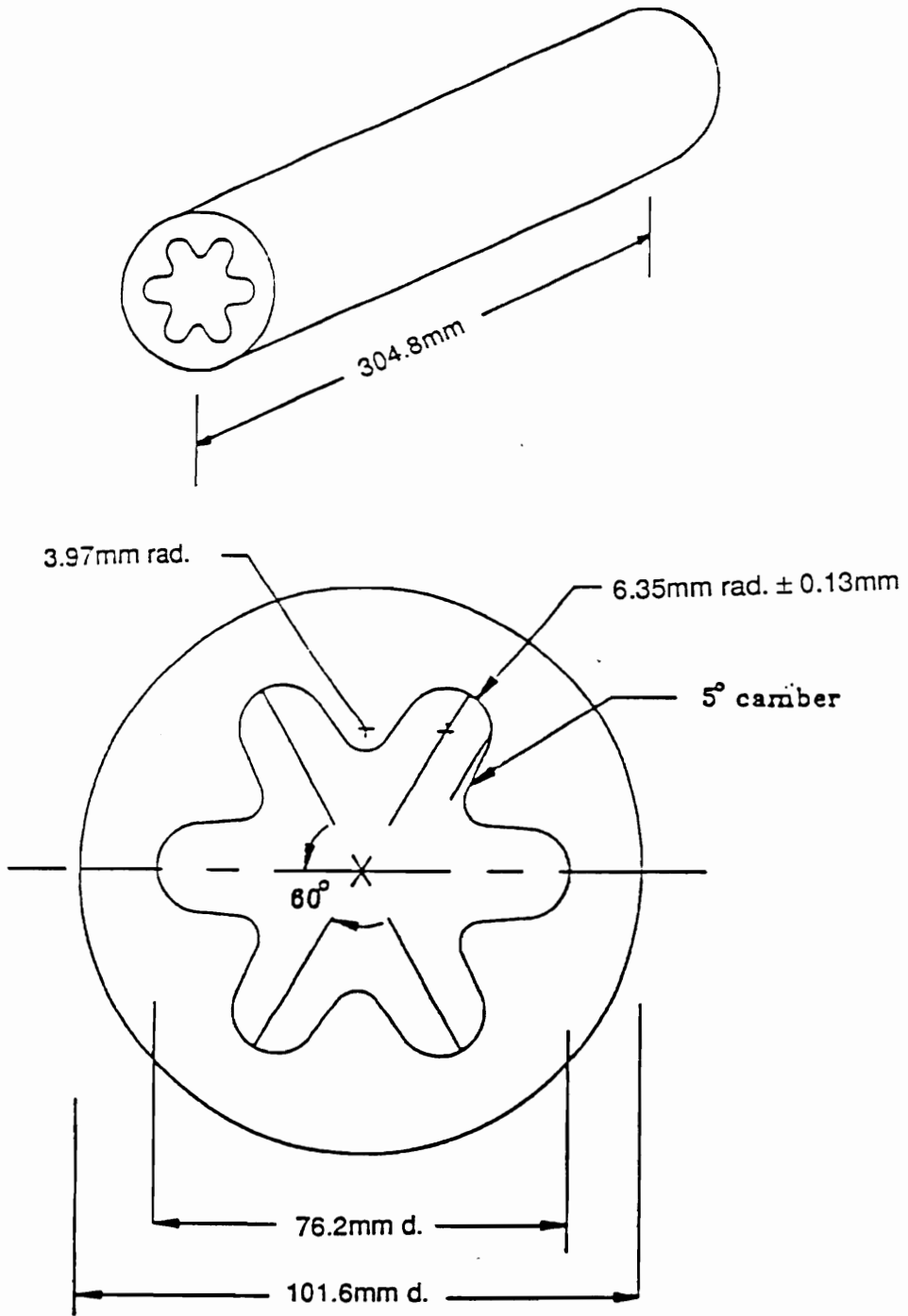


Fig.2.4: Geometry of the tested internal star grain model.

easy plane strain condition to be reasonably applied to the mid-section of the cylinder when the stress analysis is necessary. To be consistent with the previously defined seven independent geometric variables, the following values are calculated:

R: 50.8mm (2")

N: 6

w: 12.7mm (0.5")

$r_1$ : 6.35mm (0.25")

$r_2$ : 3.97mm (0.156")

$\xi$ : 30°

$\eta$ : 25°

The material of the model is one type of epoxy, PLM-9, provided by the Photolastic Division of Measurement Group and the major material properties are listed in table 2.1. It needs to be mentioned that this kind of so-called "photoelastic" material exhibits diphasic mechanical and optical characteristics. More specifically, its mechanical response, at room temperature, is viscoelastic, which can be described by the Kelvin spring-dashpot model, while above its critical temperature which is around 250°F, the material's behavior changes into the elastic regime with its Young's modulus and stress fringe sensitivity being 0.2% and 20

Table 2.1: Material properties of PLM-9 provided by Photolastic Inc.

Temperature Condition	Elastic Modulus E 1000 psi (GPa)	"C"-Stress Optical Constant psi/fringe/in (kPa/fringe/m)	Tensile Strength psi (MPa)	Coef. of Expansion PPM/°F (PPM/°C)	v
Room Temperature (72°F or 22°C)	480 (3.3)	60 (10.5)	7500 (50)	39 (70)	0.36
Stress-Freezing Temperature 230-250°F (110-120°C)	6.0 (0.041)	2.7 (0.50)	>150 (>1.0)	90 (162)	0.50

times of those at room temperature. These characteristics have made the material be much more sensitive to the loading above the critical temperature, and if the load is kept unchanged during the cooling process back to room temperature, the elastic recovery due to the removal of the load is negligible because of its relatively higher stiffness and lower stress fringe sensitivity at room temperature. Meanwhile, the Poisson's ratio of this material is increased to 0.5 above the critical temperature, and thus the material shows incompressibility which is also the case for a typical undamaged solid propellant material.

As far as the loading is concerned, internal pressure, which is one of the major types of forces due to the burning of the propellant, was applied to the model cylinder. For this purpose, two PSM-9 plates were bonded to both ends of the cylinder with a hole drilled at one side through which the air pressure could be applied (figure 2.5). The hole was threaded and a copper pipe connected to the air control valve was extended into the cylinder with Teflon tape wrapped around it to avoid leakage. Meanwhile, because of the similarity of the major mechanical properties between PSM-9 and PLM-9, the mismatch between the end caps and the cylinder due to the change of temperature was minimized, and thus possible stress concentration at these critical bonding areas was greatly reduced. Also, a sanding process of the bonding surfaces of the plates and cylinder was proved to be very helpful to enhance the bonding capability, and it is strongly recommended in the tests where

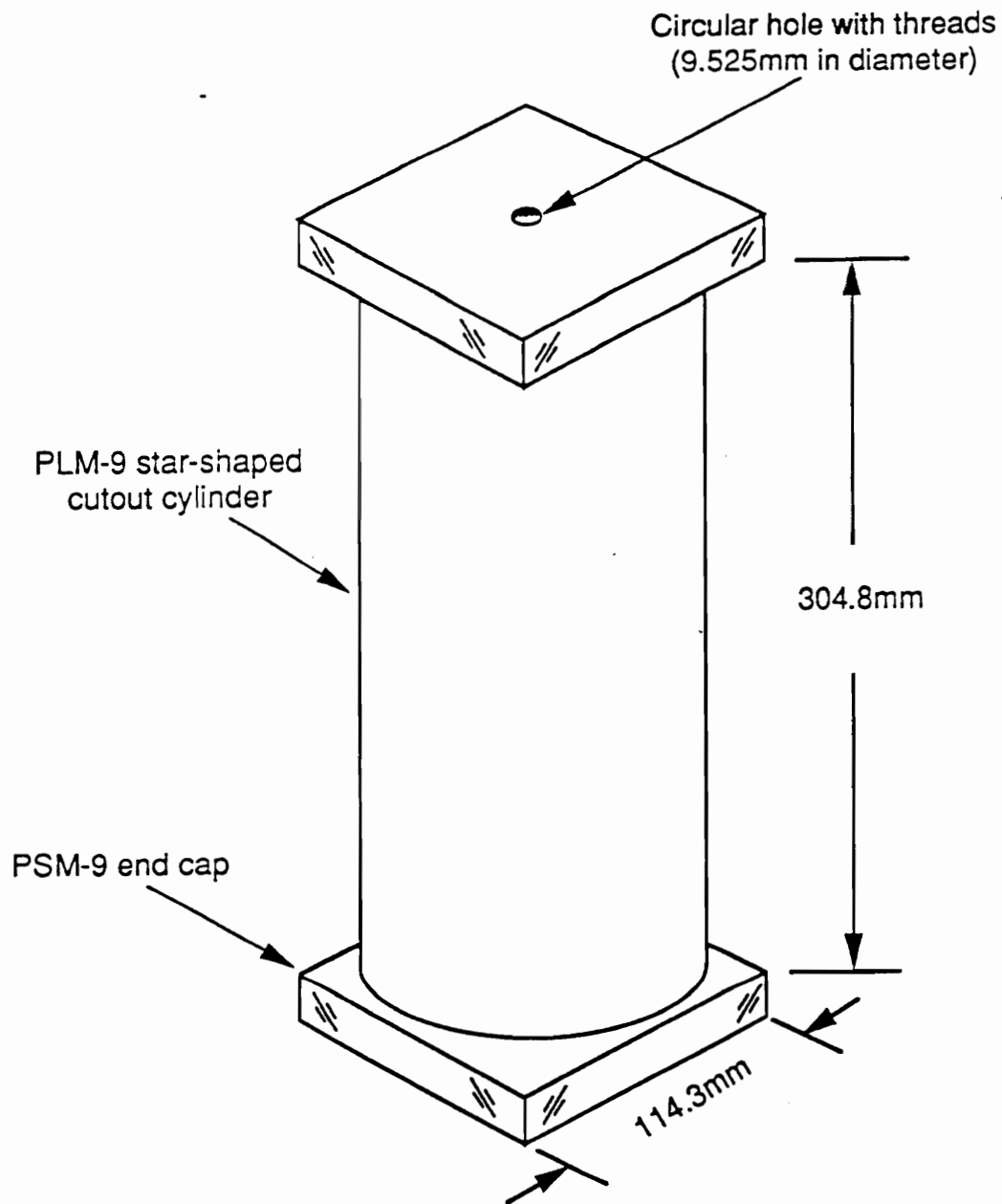


Fig.2.5: Prepared internal star grain model.



relatively high pressure is needed. Detailed description of material characteristics and specimen preparation can be found in reference (45).

## **2.3 *Stress Analysis of the Motor Grain***

### **2.3.1 Experimental Stress Analysis**

Once the specimen was prepared, it was left in a thermal control oven and the stress-freezing cycle was conducted with a 47.4kPa (6.9psi) internal pressure applied to the cylinder. The stress-freezing cycle was a predetermined heating-soaking-cooling process where the material's critical temperature was reached through heating, pressure was applied after the specimen was fully soaked and remained unchanged till its removal at room temperature. The heating and cooling processes should be slow enough to avoid any possible thermally-induced stress inside the specimen which would cause error if one only wants to study the influence from the mechanical loading.

Upon the completion of a test, a 12.7mm (0.5") thick ring specimen was removed from the mid-section of the cylinder and the

isochromatic fringes, which represented the in-plane maximum shear stress contours, were revealed through a circular polariscope setup with dark background (figure 2.6).

Although the isochromatic fringes are directly related to the in-plane maximum shear stress,  $\tau_{\max}$ , it is very easy to figure out the stress variation along the inner surface of the cylinder by noticing that one of the in-plane principal stresses is actually the internal pressure acting normal to the boundary. First of all, the in-plane maximum shear stress can be evaluated from the stress-optical law:

$$\tau_{\max} = \frac{nf}{2t} \quad (2.1)$$

where  $n$ =isochromatic fringe order

$f$ =material fringe value

$t$ =specimen thickness

The material fringe value was predetermined by two four-point bending calibration tests and the detailed procedure for conducting such tests can be found in reference (45). Thus, by counting the fringe order at a certain point, the expected in-plane maximum shear stress can be determined. Meanwhile, for a plane problem, the in-plane maximum shear stress can be related to the principal stresses as:

$$\tau_{\max} = \frac{1}{2} |\sigma_1 - \sigma_2| \quad (2.2)$$

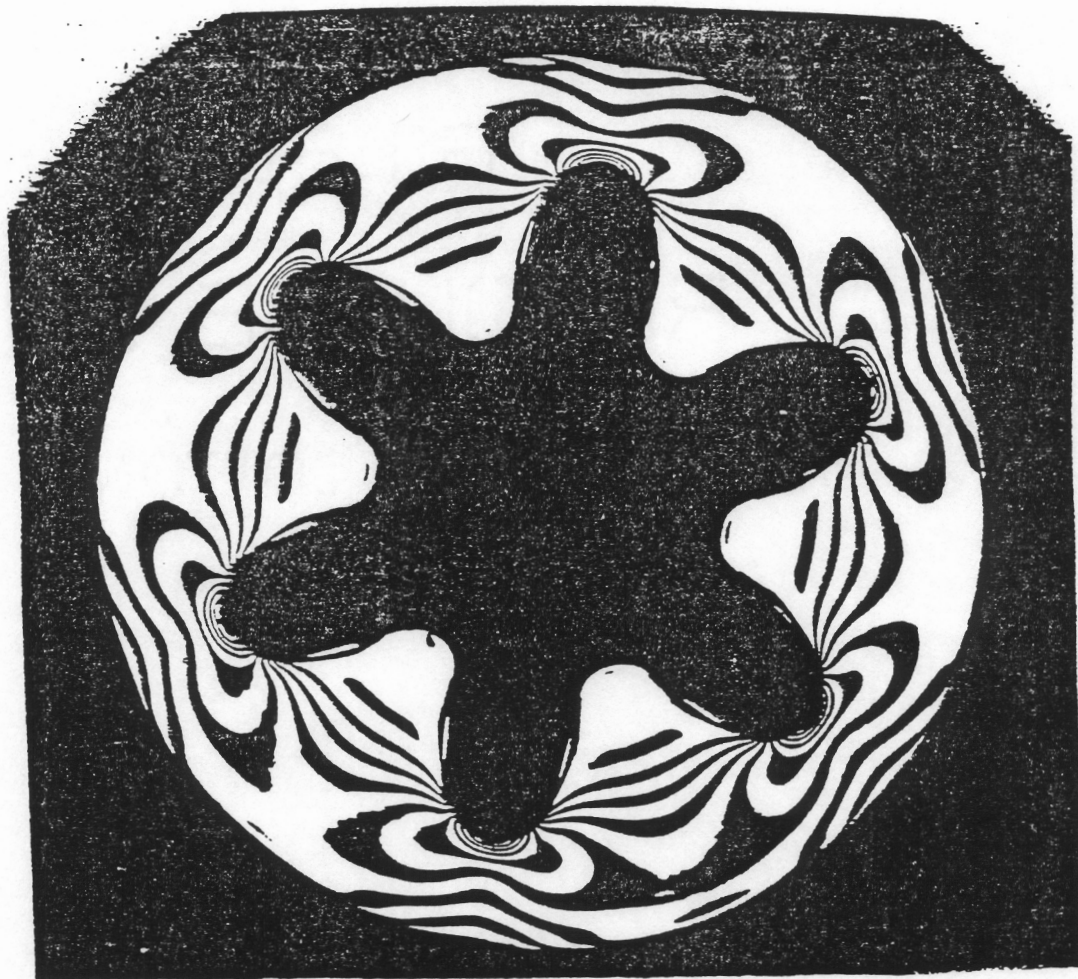


Fig.2.6: Isochromatic fringe pattern in a transverse slice of the propellant model subjected to internal pressure.

Thus, by connecting equations (2.1) and (2.2), the difference between the two principal stresses can be obtained. Since the applied pressure was identified as one of the principal stresses along the inner boundary, the next step of determining the other principal stress became a fairly simple process.

Following the above reasoning, one could obtain the variations of  $\sigma_1$ ,  $\sigma_2$ , and  $\tau_{\max}$  along the inner surface of the cylinder starting from the star finger tip (figure 2.7). If one sets up a local coordinate system moving along the inner surface (figure 2.8), the principal stress in the tangential direction ( $x_1$  direction) is influential in causing possible cracks because it tends to open up the surface micro-defects that were created in the earlier stages, such as the manufacture, transportation and storage processes. It is interesting to see, from figure 2.7, how this tangential stress varies from the maximum tensile stress at the star finger tip down to a compressive stress as one moves away from the groove. This alternation has a large gradient in the curved section, which suggests a very local stress concentration due to the top part of the star finger. On the other hand, a nearly biaxial compressive stress state was present in the straight line section (A-A' in figure 2.8), indicating a less dangerous situation compared with the curved section. These observations, in practice, not only illustrated the stress concentration effect, but provided informative insight into propellant material testing. First of all, because the propellant grain experiences different stress states at different locations, it

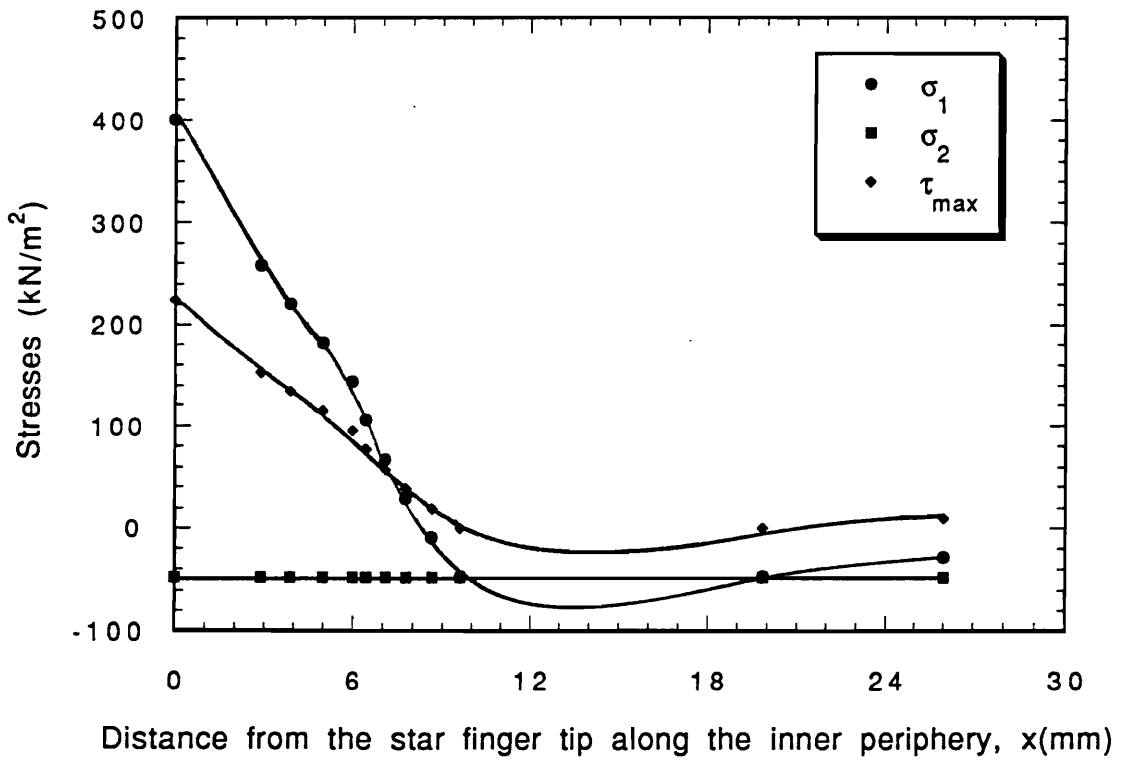


Fig.2.7:  $\sigma_1$ ,  $\sigma_2$  and  $\tau_{max}$  variations along the inner periphery of the star grain model under a 47.4kPa (6.9psi) pressure.

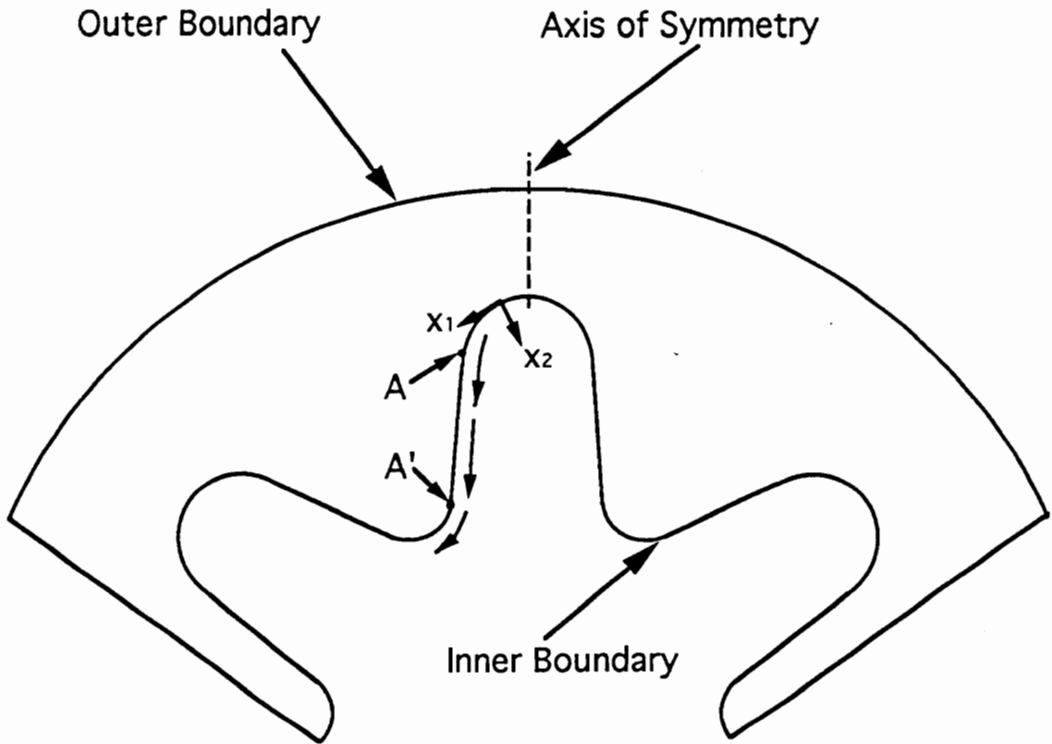


Fig.2.8: Local coordinate system along the inner boundary of the grain model.

is obviously worth testing whether the mechanical response of the propellant material is the same for tensile and compressive stresses, which is definitely beneficial for predicting the whole grain's behavior upon loading. In reality, experiments (13) showed dissimilar material properties when the propellant was loaded under different stress conditions, including tension and compression stress states. Secondly, since a large section of the inner surface of the grain was under a nearly biaxial (or even triaxial if the third direction is considered) stress state, the biaxial or triaxial specimens with simpler geometries are expected to provide valuable data because of the similar stress state in the real grain. Through the years, various kinds of specimens were developed based on similar considerations of analyzing the stress distribution inside the grain, and more detailed information can be found in reference 4.

Theoretically speaking, the principal stresses at every point can be obtained from the isochromatics pattern by certain separation techniques, such as the shear difference method and Filon's method (46). In reality, it could be tedious and not accurate enough due to the difficulty in precisely locating the broad isoclinic bands and measuring their intersection angles with a certain direction. Therefore, this step is omitted in the experimental analysis, but will be supplemented in the following finite element analysis. At the same time, the previously obtained experimental results are to be used to check the correctness and accuracy of their numerical counterparts.

### **2.3.2 Finite Element Stress Analysis**

Since the first formal presentation of the finite element method (FEM) more than thirty years ago, this numerical approach has been widely applied to various practical problems, which are not only in the fields of aerospace and mechanical engineering, but the studies of biology, geology, atmospheric physics and many more. The foundations of FEM lie in the employment of various simple "elements" to simulate a complex domain so as to easier formulate the approximate variational forms of solution in these subdivisions. Because of its high flexibility and vast applicability, an enormous amount of work has been performed towards better usage of FEM in either new subjects or complex problems of the conventional fields.

Stress analysis is one of the fundamental tasks in mechanical testing and evaluation. Different stress states and amplitudes of the stresses are expected to be achieved through this process, which not only serves as guidelines for safety control but provides valuable information for material testing. As far as the propellant grain is concerned, numerical stress analysis that will be performed later in this section is desired to check the previous experimental results and further provide more details in stress distribution and deformation of the grain.

First of all, because the specimen is long enough in its



longitudinal direction, the assumption of a plane strain condition is expected to be a reasonable choice if one wants to neglect the end effect. Secondly, due to the symmetry of the grain cross-section, only one-twelfth of the whole geometry needs to be considered (figure 2.9).

In the FEM analysis, preprocessing, processing and postprocessing are the common three stages that one has to go through. In the preprocessing stage, geometry input, mesh generation, boundary condition application and material coefficients identification are to be furnished. In the processing stage, where the finite element concepts are really applied, generation of element matrices using numerical integration, assembly of the element equations, imposition of the predetermined boundary conditions, and solution of the global equations for primary variables at the nodal points are performed. Finally, in the postprocessing stage, the desired results are displayed in a formatted form with certain secondary variables evaluated from the obtained solutions. In the present studies, the commercial FEM package PATRAN was used as the preprocessor and postprocessor, while ABACUS was chosen to be the processor.

For the geometry shown in figure 2.9, the uniformly distributed pressure of 47.4kPa (6.9psi) was applied normal to the inner periphery, while the outer boundary was free of any load. Although they were allowed to move in the local tangential

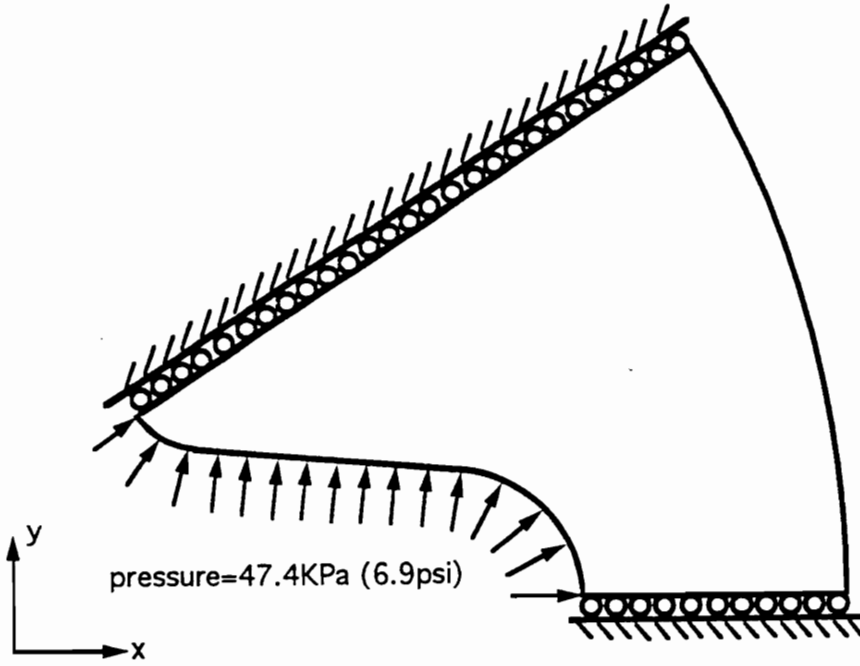


Fig.2.9: Boundary conditions used in FEM model.

directions, the two straight flanks of the whole section were prevented from moving in their local normal directions due to the consideration of symmetry. Meanwhile, the whole section was divided into six subsidiary areas with three of them closely following the curved contour of the inner boundary, which assured good element behavior, and thus accurate output, despite the complex geometry. Rectangular elements were used for every subdivision because of their better performance in providing much smoother and realistic stress distributions compared with the triangular elements which were taken as the first attempt. Furthermore, in each subdivision, a proper element number was chosen to maintain a good length-to-width ratio of the rectangular element so as to preclude very small acute angles (figure 2.10). More specifically, regions 1-6 were divided into:

Region 1:  $3 \times 5 = 15$  elements

Region 2:  $3 \times 15 = 45$  elements

Region 3:  $3 \times 20 = 60$  elements

Region 4:  $15 \times 5 = 75$  elements

Region 5:  $15 \times 15 = 225$  elements

Region 6:  $15 \times 20 = 300$  elements

The boundary condition and mesh information together with the material properties were compiled into an input file to ABACUS

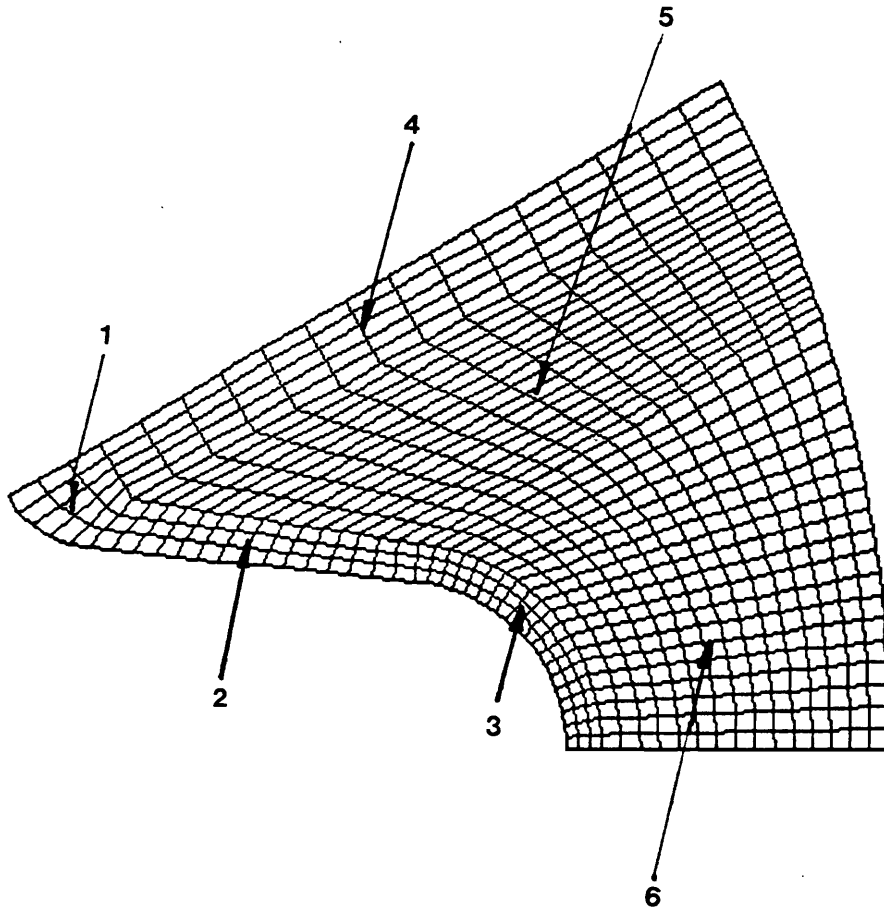


Fig.2.10: Finite element mesh for stress analysis of the uncracked grain model subjected to internal pressure.

processor from which the output file was generated and then translated by PATRAN postprocessor. The output file included the x, y stress components at each nodal point due to the internal pressure loading, from which contour maps of the stress components could be obtained (figure 2.11-2.13).

First of all, the variation of the principal stress in the tangential direction along the inner boundary can be plotted against the distance from the star finger tip (figure 2.14) together with the experimental data, from which the high stress occurring at the tip clearly illustrates the curvature effect with the stress concentration factor ( $SCF = \sigma_y / p$ ) being around 8.2. Although the experimental result of the SCF at the finger tip was obtained by an extrapolation process, it shows a good correlation with the numerical analysis, which, in another way, confirms the validity of the numerical calculation. Meanwhile, the transition of the tangential stress from tension to compression with a large gradient in the curved section of the inner boundary is again revealed in the numerical solution. Also, as was expected, the low shear stress contours imply a nearly biaxial stress state at the bottom of the fillet of the star.

One big advantage of applying numerical analysis is that once the problem is well formulated (based on proper physical considerations and experimental support), an enormous amount of detailed information can be available all at one time. As was

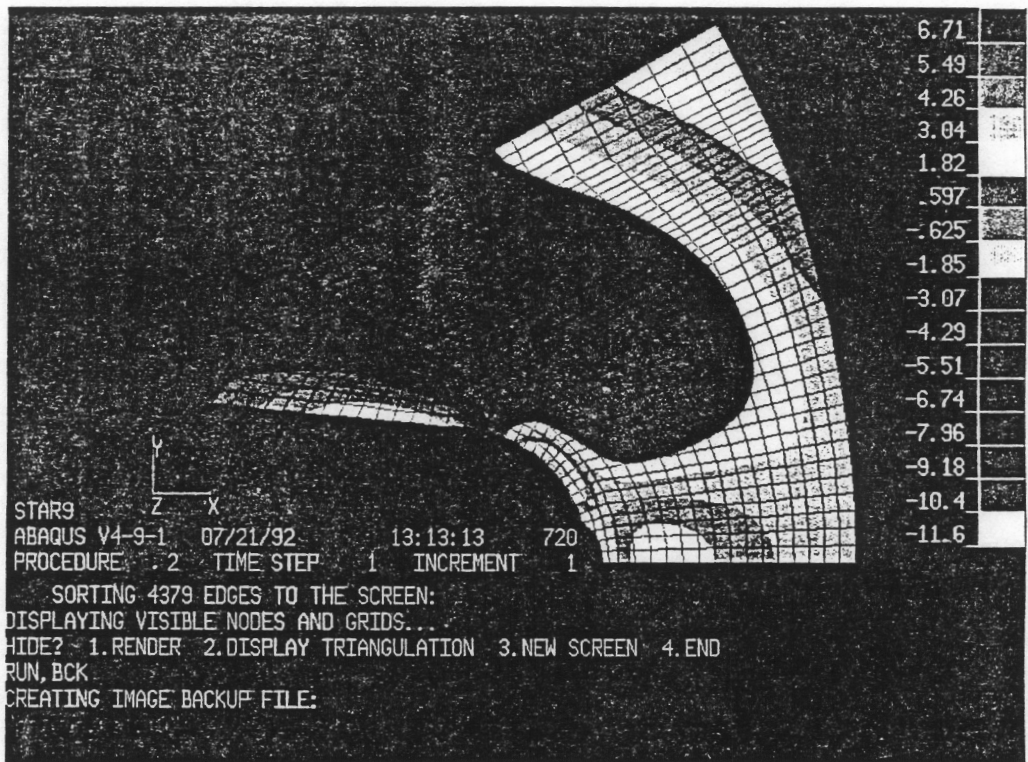


Fig.2.11:  $\sigma_x$  contour map of the pressurized uncracked grain model by FEM analysis.

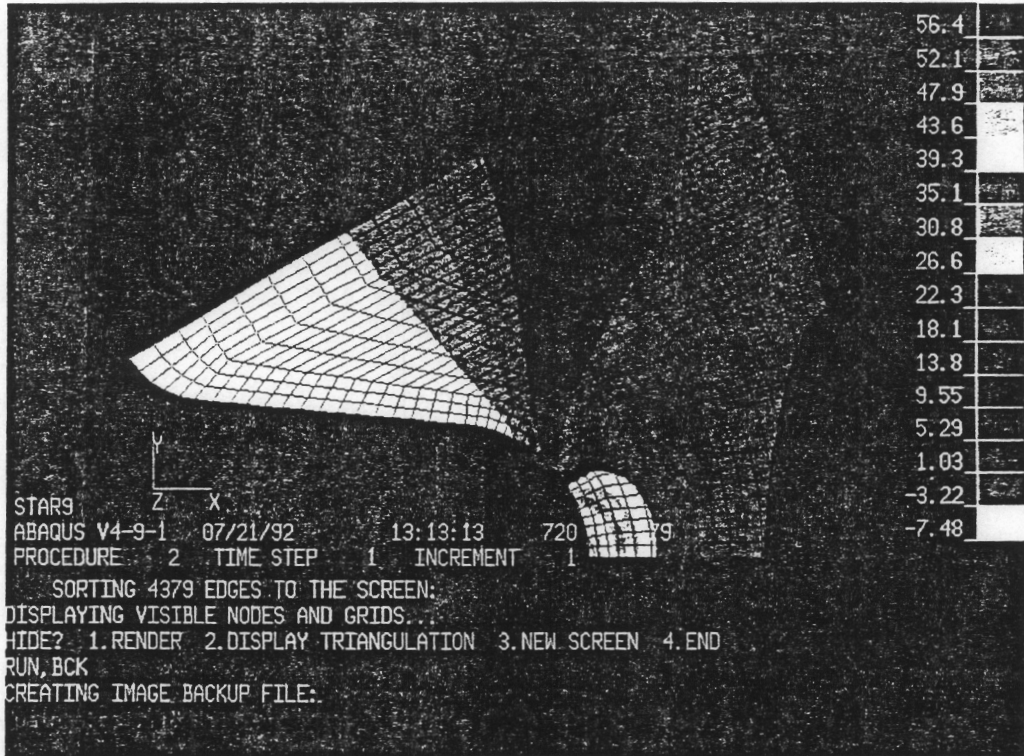


Fig.2.12:  $\sigma_y$  contour map of the pressurized uncracked grain model by FEM analysis.

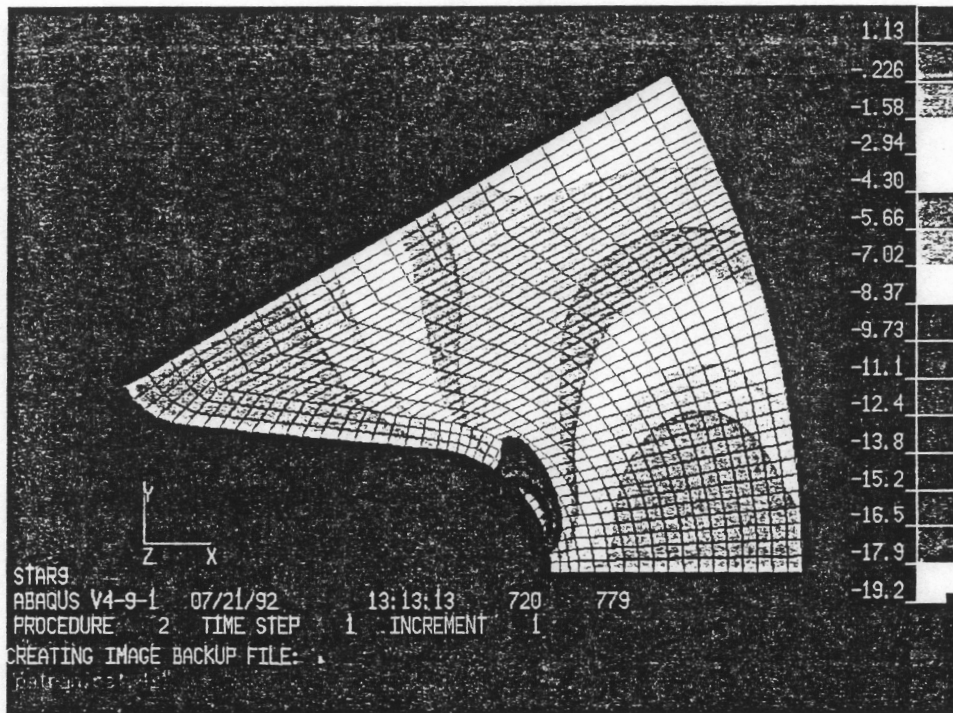


Fig.2.13:  $\tau_{xy}$  contour map of the pressurized uncracked grain model by FEM analysis.



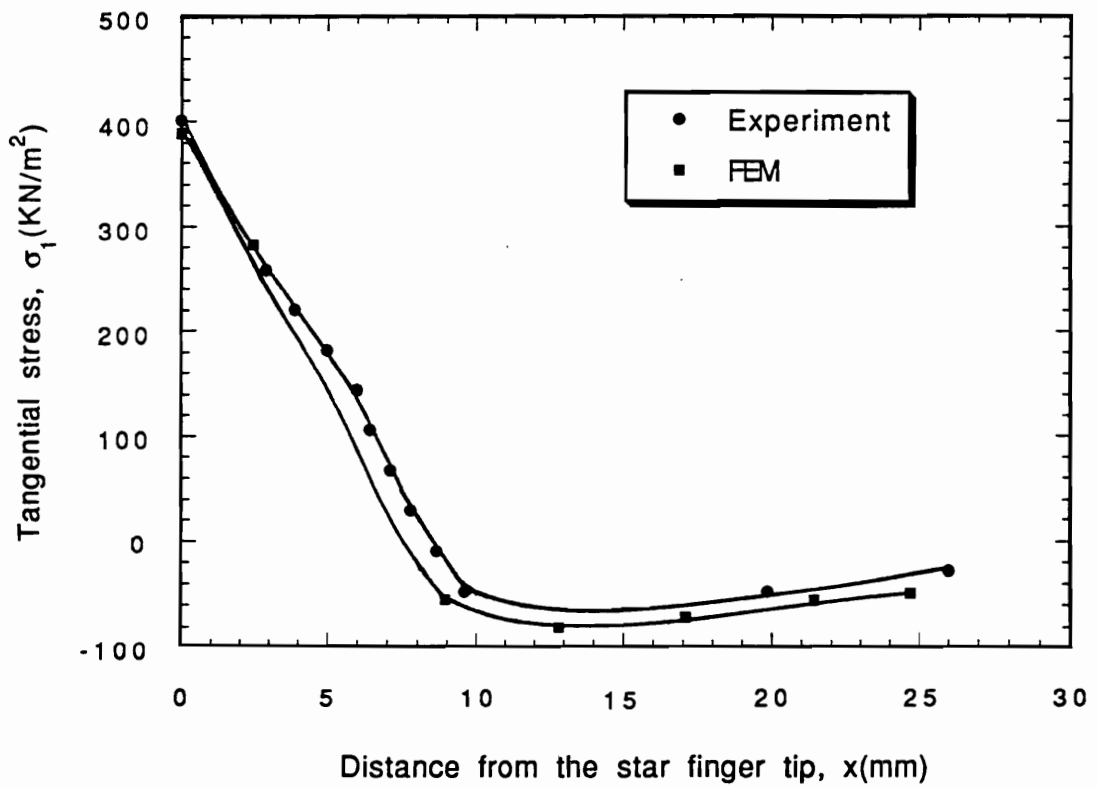


Fig.2.14: Comparison of  $\sigma_1$  variation between experimental and FEM analysis along the inner periphery of the star grain model under a 47.4kPa (6.9psi) pressure.

mentioned in the earlier section, principal stress separation could be a tedious and time-consuming process in the photoelastic analysis, but became fairly easy in the finite element analysis. In fact, the principal stresses were given as a direct output at each nodal point and one only needs to correlate the node number with certain principal stress pairs, and then determine the locations of these nodal points so that the principal stress distribution can be acquired in the whole specimen. The knowledge of the principal stress distribution can not only illustrate the stress concentration effect from which safety control can benefit, but also can provide useful information in predicting the existing crack growth direction. Detailed discussion will be presented in later chapters.

Besides the stress variation along the inner boundary of the cylinder, it is also of interest to study how the principal stress varies through the thickness of the wall of the cylinder, especially along the line of symmetry which starts from the tip of the star finger. Because the finger tip is the location where the highest stress concentration occurs, it becomes the most likely place for the pre-existing micro-defect to grow into a macro-crack which is expected to propagate along the axis of symmetry upon pressurization. Meanwhile, the high curvature effect is to elevate the stress distribution around the finger tip, and the finite element results can precisely demonstrate how large this effect is by comparing the results with the thick-wall cylinder Lamé solution. Furthermore, the stress analysis of the uncracked specimen can be

readily adopted in the weight function method of determining SIF in cracked bodies, which is to be explained in the next chapter.

By identifying the nodal points along the axis of symmetry, the principal stress variations were plotted in figure 2.15 in addition to the Lamé solution for a thick-wall circular cylinder under internal pressure, where the thickness and outer radius, 12.7mm (0.5") and 50.8mm (2"), were chosen to be the same as those of the internal star model. It is seen that, compared with the internal star grain, the hoop stress,  $\sigma_2$ , in Lamé's solution bears a gradual transition from its maximum value at the inner boundary down to the minimum at the outer border, and the difference between these two solutions is most significant within 20% of the wall thickness. In other words, the stress elevation due to the high curvature effect near the star finger tip dies out as one goes beyond 20% of the wall thickness, which is really an indirect support of modeling the internal star grain by an "equivalent" circular cylinder when the region of interest is far away from the highly curved finger tip area. In fact, this observation is to be adopted in the next chapter's discussion of developing a rationale to predict the SIF's of a cracked specimen. Meanwhile, the radial stress,  $\sigma_1$ , in the internal star grain shows an interesting sign change from compression to tension at around 10% of the net wall thickness from the tip of the star finger, which cannot be predicted by the thick wall circular cylinder solution. Since the loading conditions and the outer boundary were assumed to be the same in these two cases, this difference in the

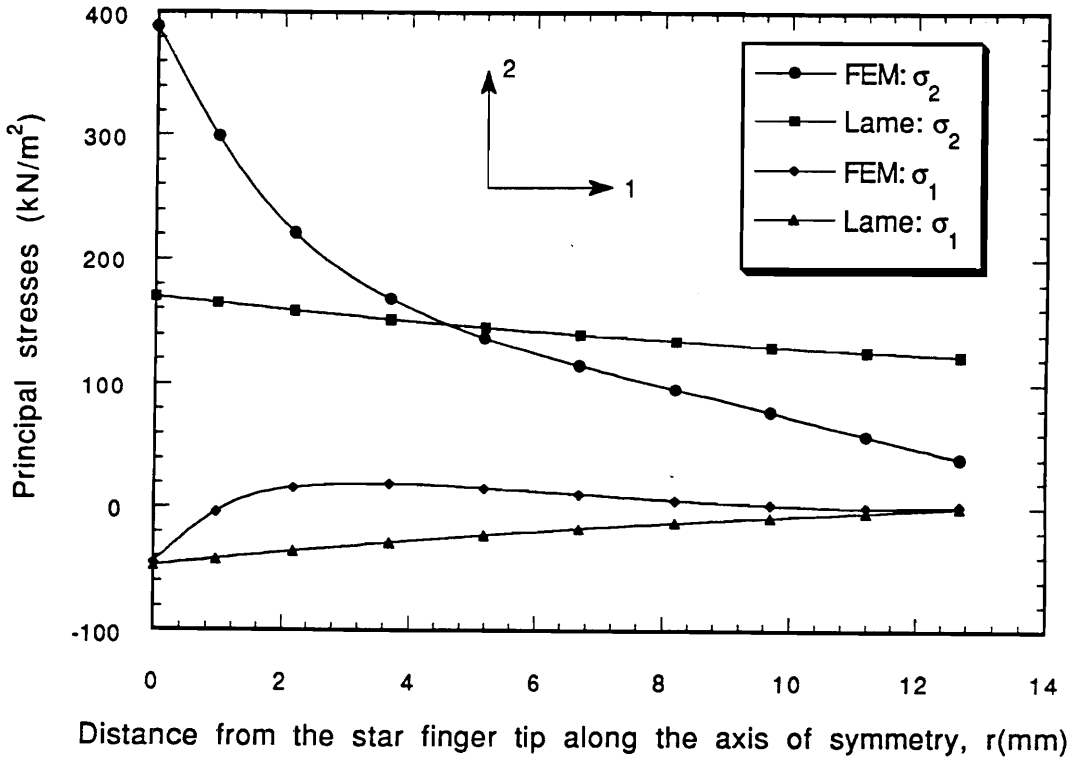


Fig.2.15: Comparison of  $\sigma_1$  and  $\sigma_2$  variations between FEM results of the internal star grain and relevant Lamé solution to the circular cylinder along the axis of symmetry.

radial stress can only be induced from the geometric difference of the inner periphery, i.e. the presence of the star finger. However, the radial stress is not very influential in the analysis concerning radially oriented cracks due to both its small magnitude and direction.

In order to further confirm the experimental results, the maximum shear stress can be obtained from the finite element calculations, since the two in-plane principal stresses are known. More specifically, along the axis of symmetry, the maximum shear stress variation from FEM is plotted together with the result from the isochromatics pattern (figure 2.16) and the difference appears to be within an acceptable margin. Meanwhile, if the whole cross-section of the grain is expected to satisfy equilibrium (figure 2.17), one should have (by assuming unit thickness quantities):

$$p \times AA' = 2 \int_A^B \sigma_2 dx \quad (2.3)$$

Through a curve-fitting process, the variation of the hoop stress,  $\sigma_2$ , can be expressed by the following polynomial with the correlation factor of 0.99:

$$\sigma_2 = 58.0 - 437.8x + 1917x^2 - 4017x^3 + 3037x^4 \text{ (psi)} \quad (2.4)$$

By substituting equation (2.4) into the right side of equation (2.3), the integration can be evaluated as:

$$2 \int_A^B \sigma_2 dx = \int_0^{0.5} \sigma_2(x) dx = 20.74 \text{ (lb/in)} = 3632 \text{ (N/m)} \quad (2.3.1)$$

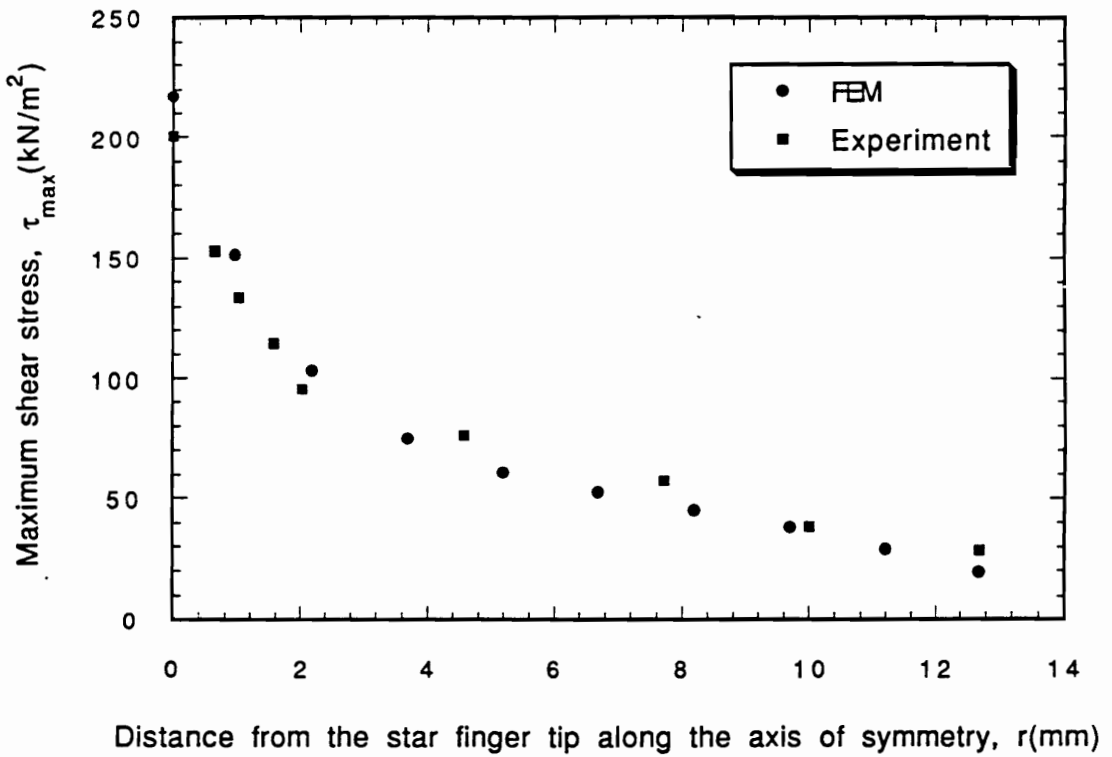


Fig.2.16: Comparison of the maximum shear stress along the axis of symmetry between the FEM data and experimental results.

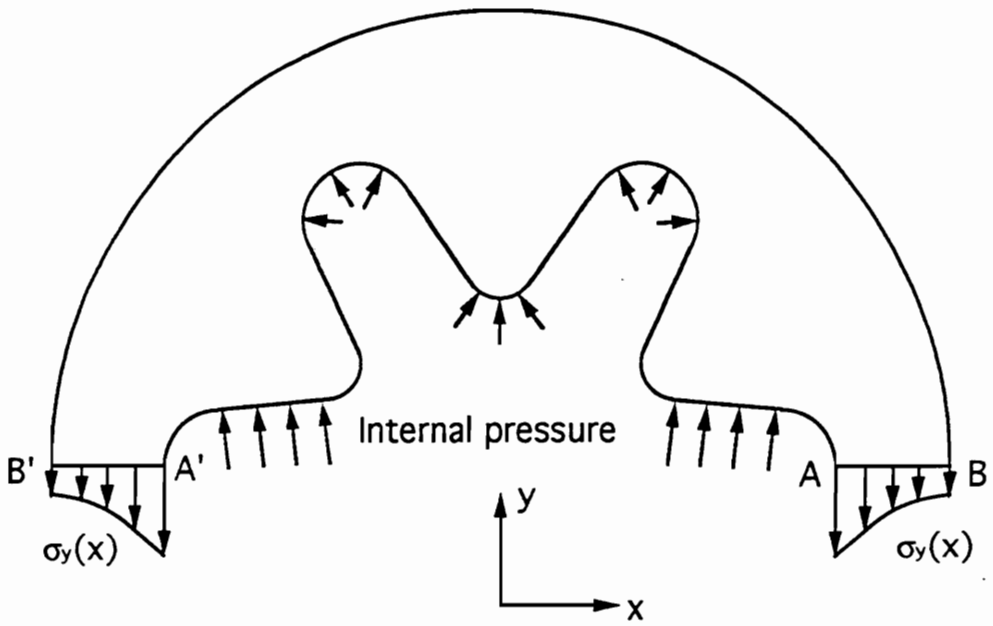


Fig.2.17: Force balance diagram of the internal star grain model.

Meanwhile, the left side of equation (2.3) is:

$$p \times AA' = 6.9 \times 3 = 20.7(\text{lb/in}) = 3625(\text{N/m}) \quad (2.3.2)$$

The relative error of equations (2.3.1) and (2.3.2) is 0.2%, which, in a way, proves the correctness of the FEM analysis.

Another interesting issue is the deformation of the grain upon loading, especially the behavior of the outer boundary which is bonded by the case. Upon ignition, the grain starts to endure high pressure and the nonuniform deformation due to the varying wall thickness causes a nonuniform compressive load onto the case. The configurations of the studied section before and after loading were compared in figure 2.18 along with the radial displacement variation along the outer boundary. It is expected that the location of the largest deformation has the maximum interphase compression between the grain and the case if only the pressure loading is considered. It is also seen, from figure 2.18, that the radial displacement,  $U_r$ , increases as the angle,  $\theta$ , increases, which shows the smallest radial displacement at the thinnest section and the largest value at the thickest part. This observation appears to be counter-intuitive, but rigorous proof shown in appendix B further confirms the FEM results. In reality, the present analysis can be combined with other factors, such as the mismatch in thermal expansion between the grain and the case due to the change of temperature, to further optimize the design of the grain case, such as where and how to apply the reinforced stiffeners onto the case.



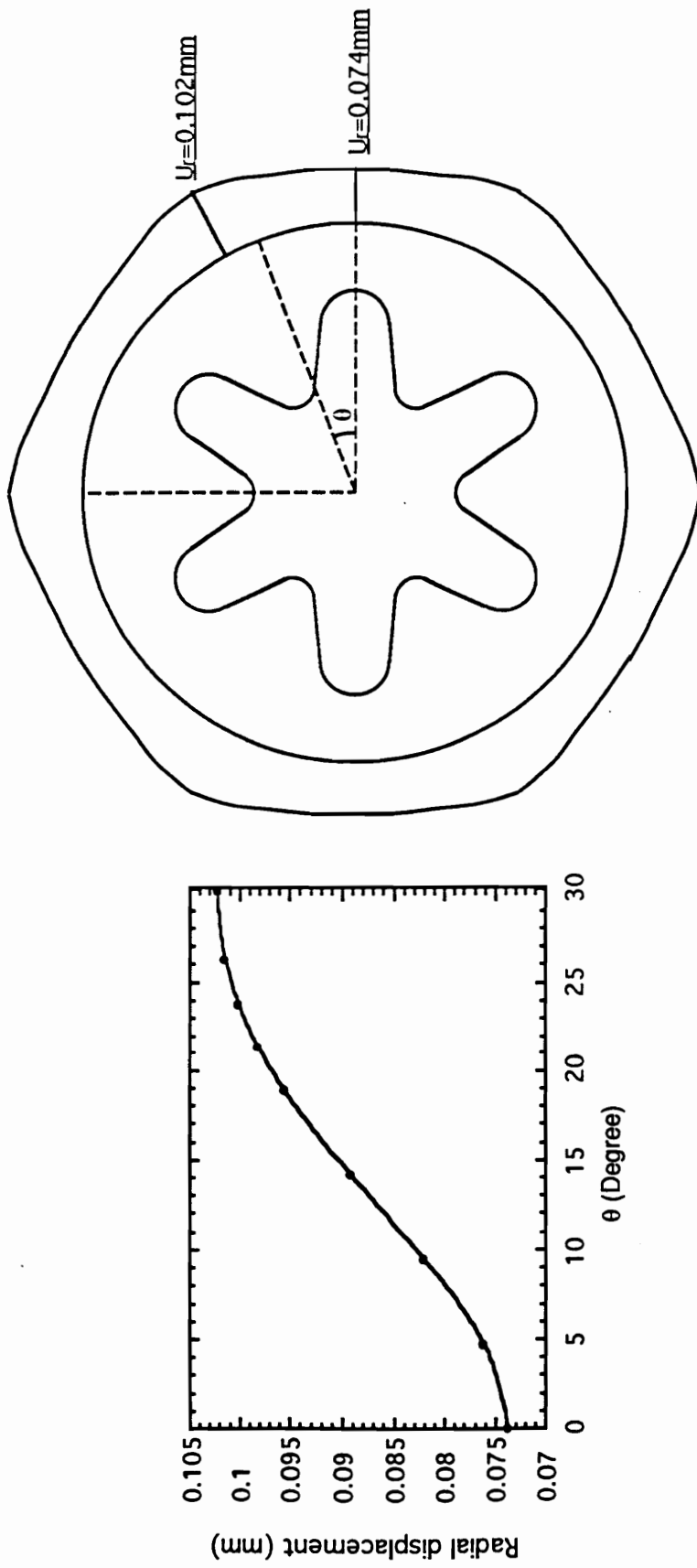


Fig.2.18: Outer surface deformation of the grain model subjected to internal pressure.

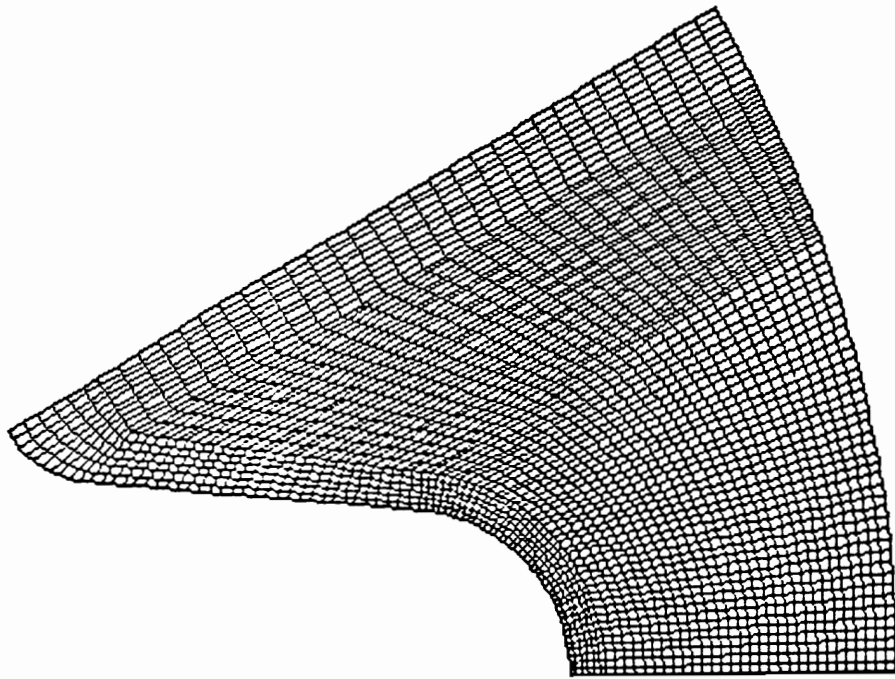


Fig.2.19: Refined finite element mesh for stress analysis of an uncracked star-shaped cylinder section under internal pressure.

Finally, the sensitivity of the stress analysis towards the density of the mesh needs to be briefly mentioned. To explain this, another finer mesh (figure 2.19) was used and the exact same procedure was followed as for the first coarser mesh. Being a representative example, the comparison between the principal stress variations using these two sets of meshes was sketched in figure 2.20. Although the element number in the second set was quadrupled (2880 elements instead of 720 elements), the hoop and longitudinal stresses along the axis of symmetry were altered by a very small amount, which suggests the good suitability of using FEM in the grain model's stress analysis without a significant amount of computation.

Before closing this section, several remarks need to be addressed on the FEM analysis. First of all, although the numerical method had been widely and successfully used in the area of stress analysis, one has to keep in mind the importance of experimental support. The experimental results can not only provide the first-hand information on stress distribution in the real situation, but guide the numerical analysis in the right direction, which, in this particular case, included the manner of dividing subsidiary regions and selecting element type, etc. Secondly, the boundary conditions that are imposed on the model are critical for the final results and they should be strongly based on physical considerations of the real situation. In other words, extreme care should be taken if one tends to apply solutions derived from one set of boundary conditions to

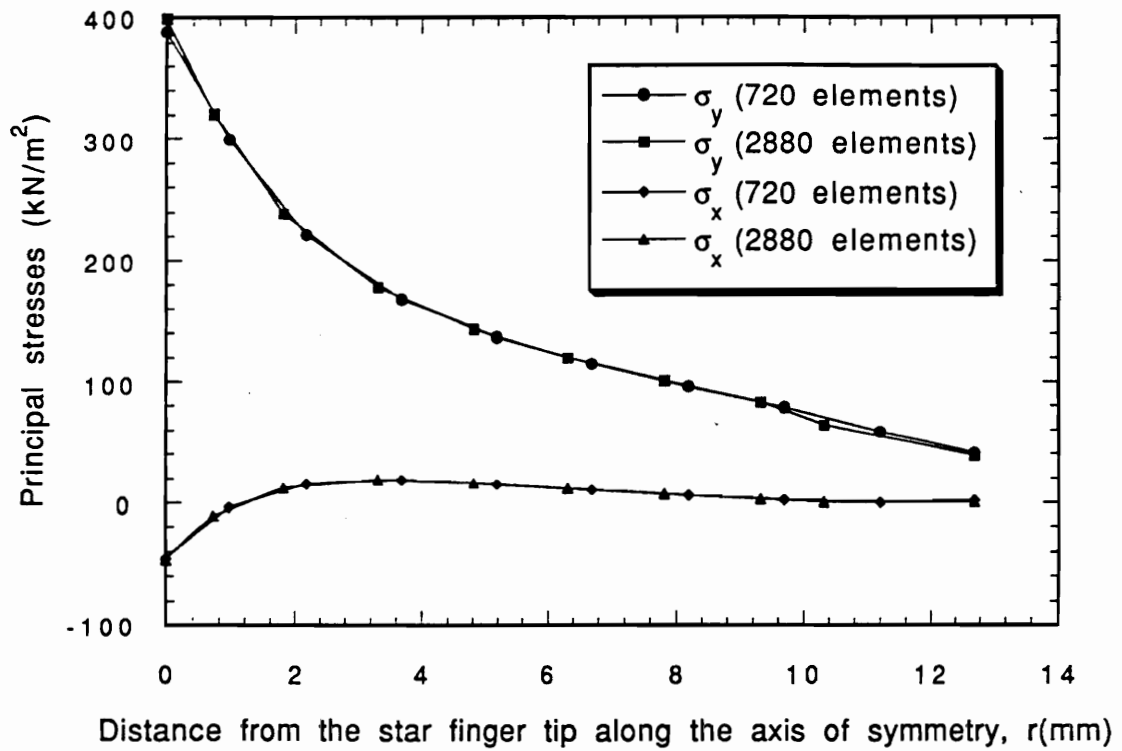


Fig.2.20: Comparison of the principal stress variations along the axis of symmetry by using two sets of meshes shown in figures 2.10 and 2.19.

another similar problem. Thirdly, it is always helpful to make as many correlations as possible between the experimental results and numerical calculations so that more reliable conclusions can be drawn. Finally, the CPU time and difficulties in correctly formulating or modeling the real problems in the numerical analysis should be seriously considered before running any major computation, since considerable cost could be possible, especially in studying complex fracture problems.

## Chapter 3: Stress Intensity Factors (SIF's) Prediction for Symmetric Surface Cracks

### **3.1 Problem Definition**

As was stated earlier, research on propellant grain analysis has been mainly focused on the studies of the "perfect" ("no-defect") models or at most those with two-dimensional through-cracks. However, surface cracks, in reality, are the major defects that have been detected inside the grain. Meanwhile, due to the size of the rocket propellant grain, it is very unusual to have the cracks all the way along the grain's longitudinal direction. Thus, further efforts are needed to investigate the three-dimensional nature of the surface cracks so as to provide a more realistic insight into propellant fracture behavior and deliver a rational prediction of the onset of failure based on the experimental results.

From the stress analysis performed in the last chapter, it is natural for one to give a first look at the star finger tip where the highest stress concentration occurs. Due to the presence of the high

stress, the pre-existing micro-defects close to this area are much easier to be developed into macro-cracks compared with those in the lower stressed regions. Meanwhile, since the principal stress direction along the inner boundary is either in the local tangential or normal direction, the possible cracks are expected to grow perpendicular to the inner periphery. Hence, the first attempt is to study surface cracks emanating from the star finger tip and propagating along the axis of symmetry (figure 3.1). In this phase of study, cracks with different depths are to be studied, from which the curvature effect due to the star finger can be evaluated. Furthermore, analytical and numerical models are to be constructed based on the knowledge of experimental results to predict the SIF of a symmetric surface crack with an arbitrary depth.

### ***3.2 Experimental Procedure and Analyzed Results***

An internal star grain model with the same geometry as the one described in the last chapter was taken to be the test specimen and the only difference was the addition of an initial surface crack at the middle of the cylinder. To do this, a hole with 12.7mm (0.5") diameter was drilled at the opposite side of the location where the crack was to be made. A sharp-tip blade with its holding fixture

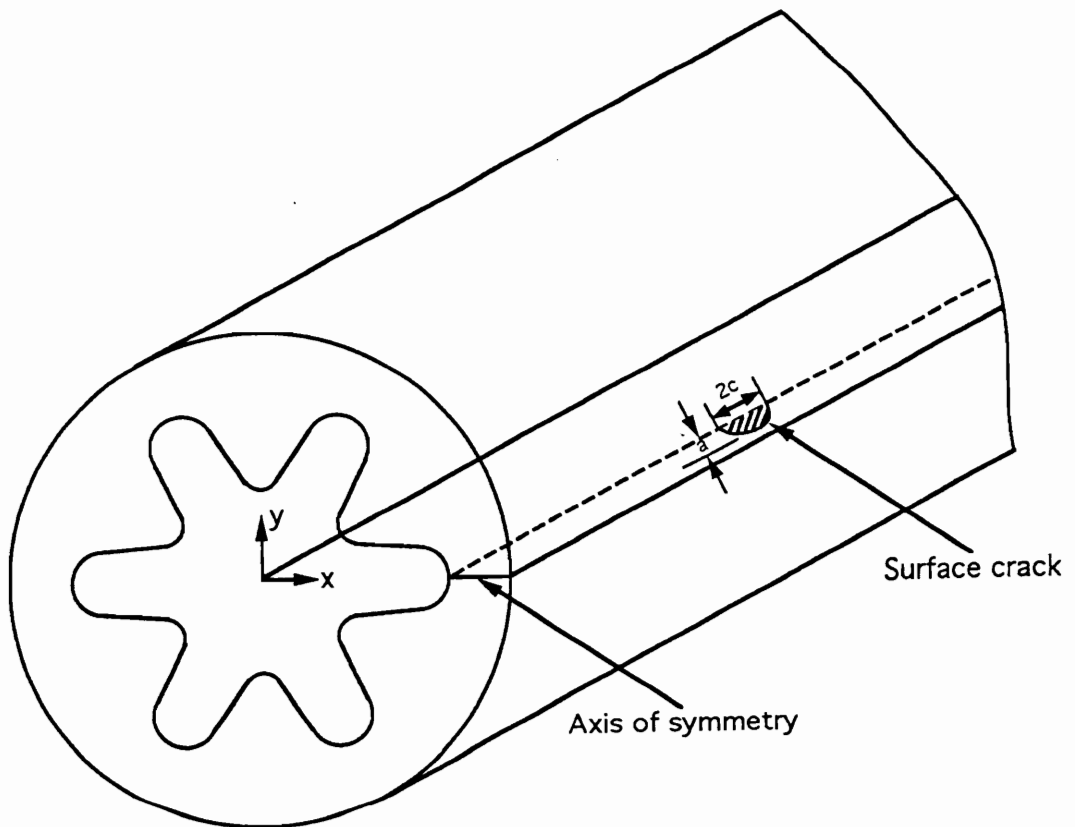


Fig.3.1: Internal star grain model containing a surface crack emanating from the star finger tip along the axis of symmetry.



was then extended through the hole until it touched the inner surface of the cylinder. By firmly holding the fixture rod, the hammer strike could dynamically insert an initial crack into the grain model with the crack surface normal to the inner boundary (figure 3.2). After sealing the hole and the two ends of the cylinder with PLM-9 epoxy, the grain model was left inside a thermal control oven to experience the frozen stress cycle. After the specimen was above the critical temperature and fully soaked, a relatively high pressure of 99kPa (14.4psi) was applied to grow the starter crack to the desired depth, at which time the pressure was lowered to 47.4kPa (6.9psi) till the end of the cooling process. Thin slices mutually orthogonal to the crack border and crack surface along the crack front were removed from the specimen (figure 3.3) and fed into a specially designed polariscope (47) for data extraction. Since the cracks were aligned along the axis of symmetry, a Mode I stress condition prevailed in this case. Thus, by using the proper algorithm (see appendix A), the photoelastic readings from different slices could finally yield the SIF distribution around the crack front. More detailed experimental procedure was recorded in reference (45).

From the analyzed results (48), a fairly uniform distribution of SIF (figure 3.4) was observed along the crack front for different crack geometries (table 3.1). This observation actually allows one to estimate the SIF value only at one location along the crack border (usually the deepest penetration point) which can represent, to a large extent, the whole crack behavior. The following discussion of

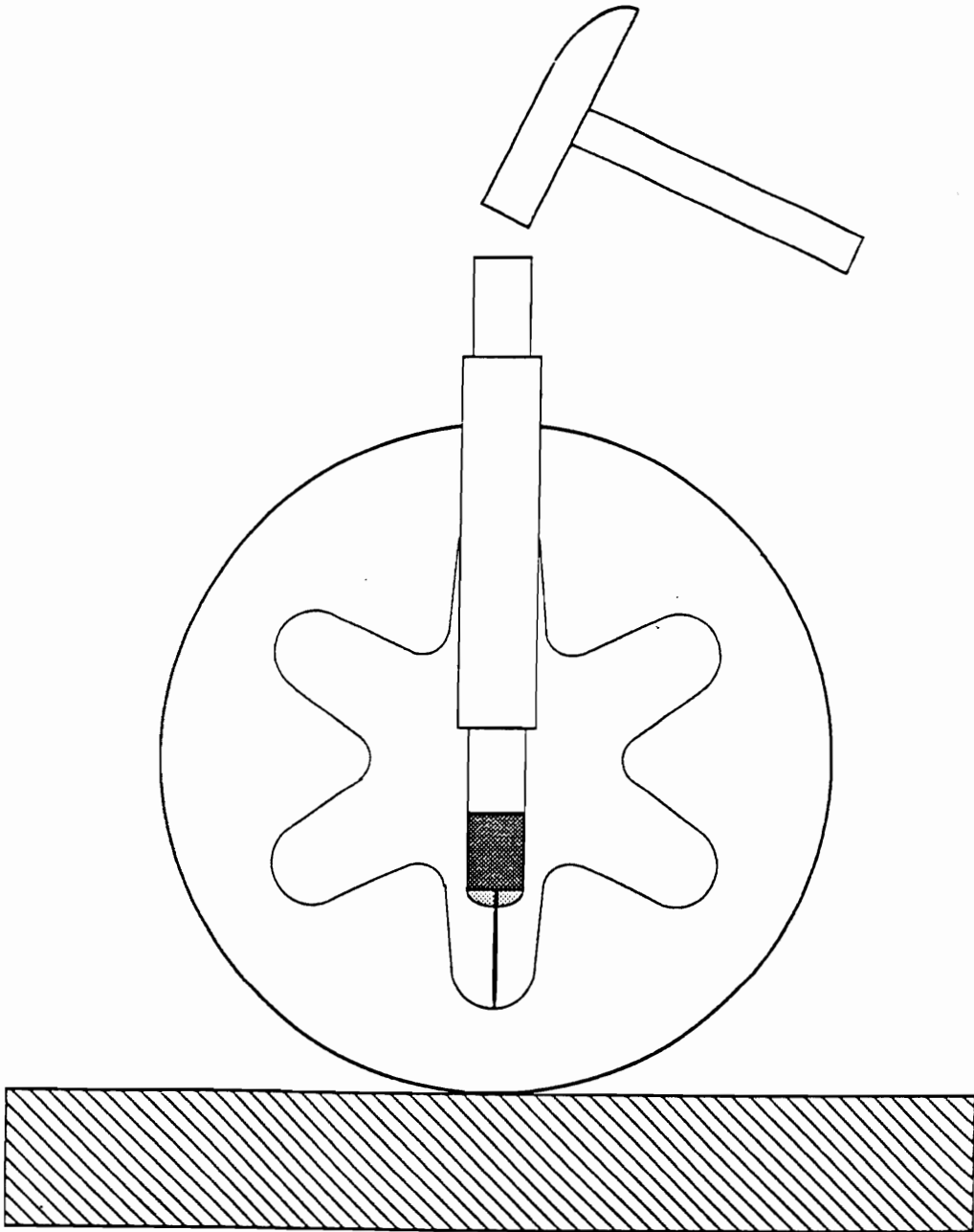


Fig.3.2: Fixtures for making a symmetric crack.

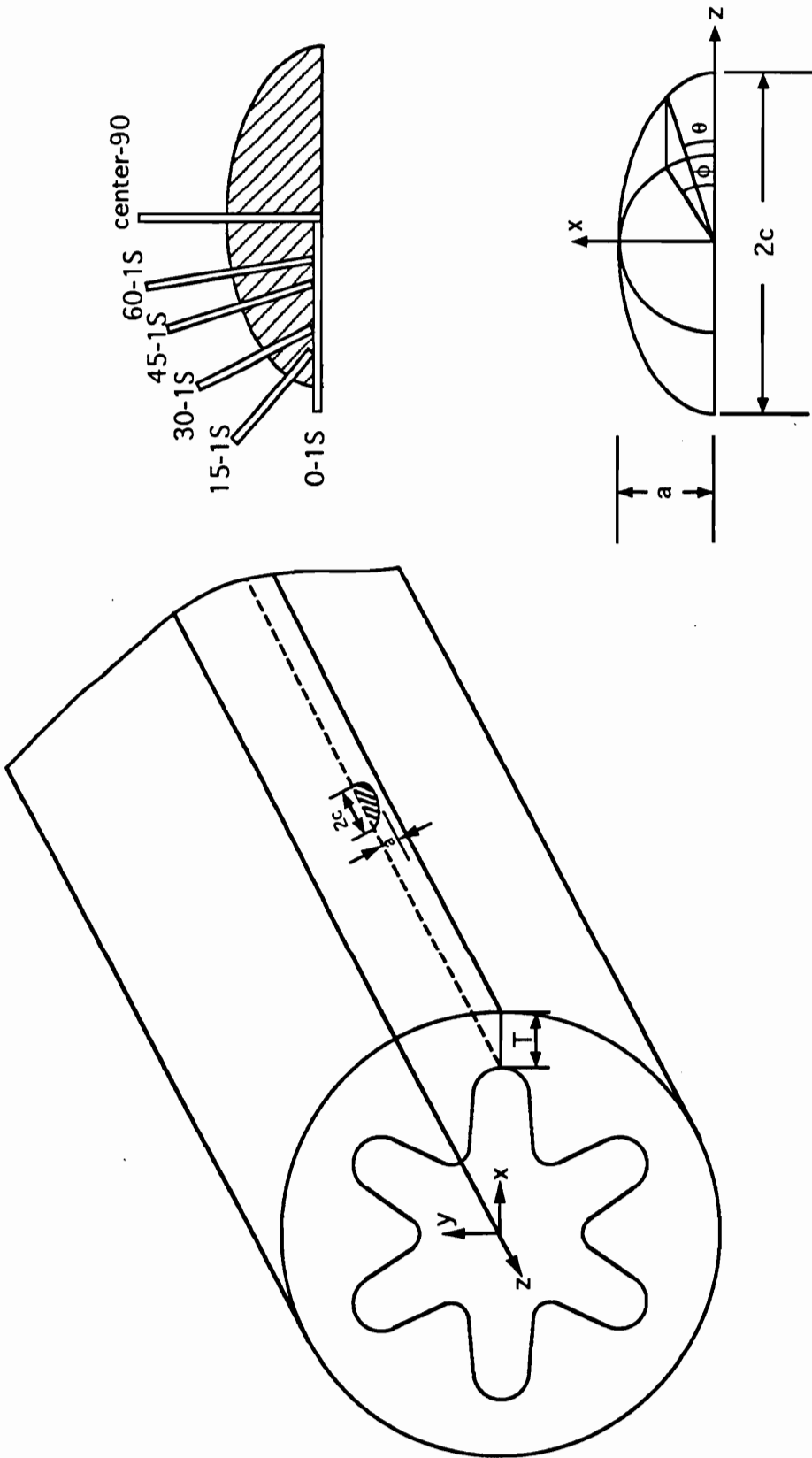


Fig.3.3: Schematic demonstration of the slice-cutting process.

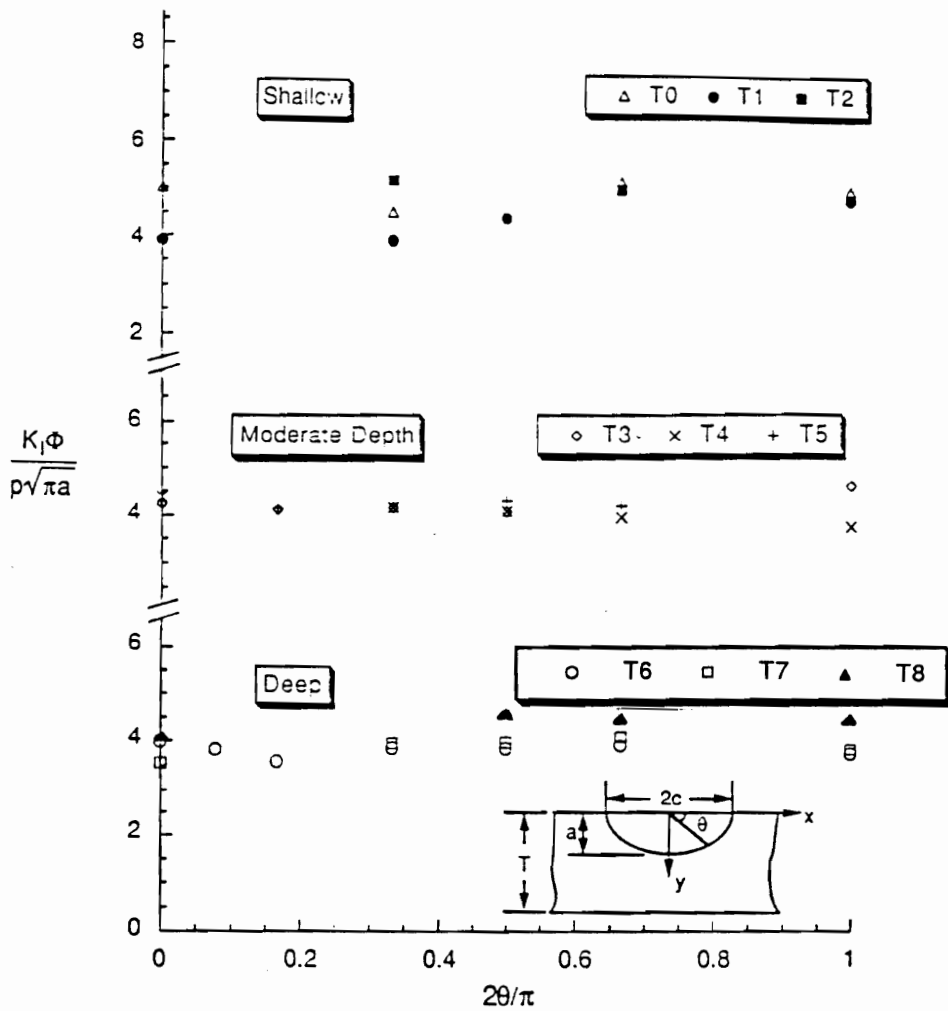


Fig.3.4: Analyzed results showing SIF distributions for symmetric cracks with different depths.

Table 3.1: Tested symmetric crack geometries.

Test No.	a(mm)	c(mm)	a/c	a/T	$\Phi^*$
T0	3.6	6.7	0.54	0.28	1.23
T1	3.2	6.2	0.52	0.25	1.22
T2	4.1	7.5	0.55	0.32	1.24
T3	6.2	13.5	0.46	0.45	1.18
T4	6.6	12.7	0.52	0.52	1.22
T5	7.3	17.0	0.43	0.56	1.16
T6	8.4	19.1	0.44	0.66	1.17
T7	7.9	17.6	0.45	0.62	1.17
T8	9.4	18.8	0.50	0.74	1.21

$$* \Phi = \int_0^{\pi/2} \left( \cos^2 \phi + \left( \frac{a}{c} \right)^2 \sin^2 \phi \right)^{1/2} d\phi \text{ (see figure 3.3 for a, c, T and } \phi \text{)}$$

developing a certain rationale for predicting the SIF for a symmetric crack with an arbitrary depth is based on the experimental results. In this development, the three-dimensional effect has to be taken into account to eliminate the possible elevation of SIF values due to a two-dimensional through-thickness flaw. Meanwhile, physical considerations of specimen geometry and loading conditions should also be highlighted in order to present a valid and meaningful model, and further studies are to be addressed in the next three sections.

As far as the crack geometry is concerned, experiments showed the propagated crack was following the axis of symmetry in a planar fashion, exhibiting a semi-elliptical crack surface. Meanwhile, from table 3.1, it is seen that the ratio of crack depth,  $a$ , to half crack length,  $c$ , decreases as the crack grows deep, which suggests the growth in the depth direction was slightly impeded by the back surface for deep cracks. Nevertheless, the obtained  $\frac{a}{c}$  values are useful in approximately estimating the size of a pre-existing surface crack if, by certain non-destructive testing methods, either the crack length or the crack depth can be measured.

### **3.3 "Equivalent" Radius Model**

Since no analytical or numerical solutions are available in the

literature to deal with the surface flaw problem of the internal star grain from a three-dimensional point of view, it is imperative and challenging to develop such a model to fill this gap. The present and following two sections are to focus on developing this kind of formulation to predict an existing symmetric crack's SIF values without conducting any additional test.

In reference 45, a so-called "equivalent" circular cylinder model was presented to predict SIF's for deep cracks. The idea was to simply replace the internal star grain by a circular cylinder with a certain inner radius (called "equivalent" inner radius) so that the SIF distributions were similar in both cases (figure 3.5).

To do this, Newman-Raju's finite element solution (49) to a circular cylinder with a radial internal surface crack under pressure loading was adopted to create the model with an "equivalent" inner radius. More specifically, the outer radius of the circular cylinder and crack size were fixed in the model and what needed to be done was to alter the inner radius value of the circular cylinder between the tip and valley of the star until a similar trend of SIF distribution compared with the surface crack in the internal star cylinder was achieved.

In Newman-Raju's formulation, internal pressure loading was superimposed by the combination of four base stress distributions, uniform, linear, quadratic and cubic, which led to the following expression for SIF:

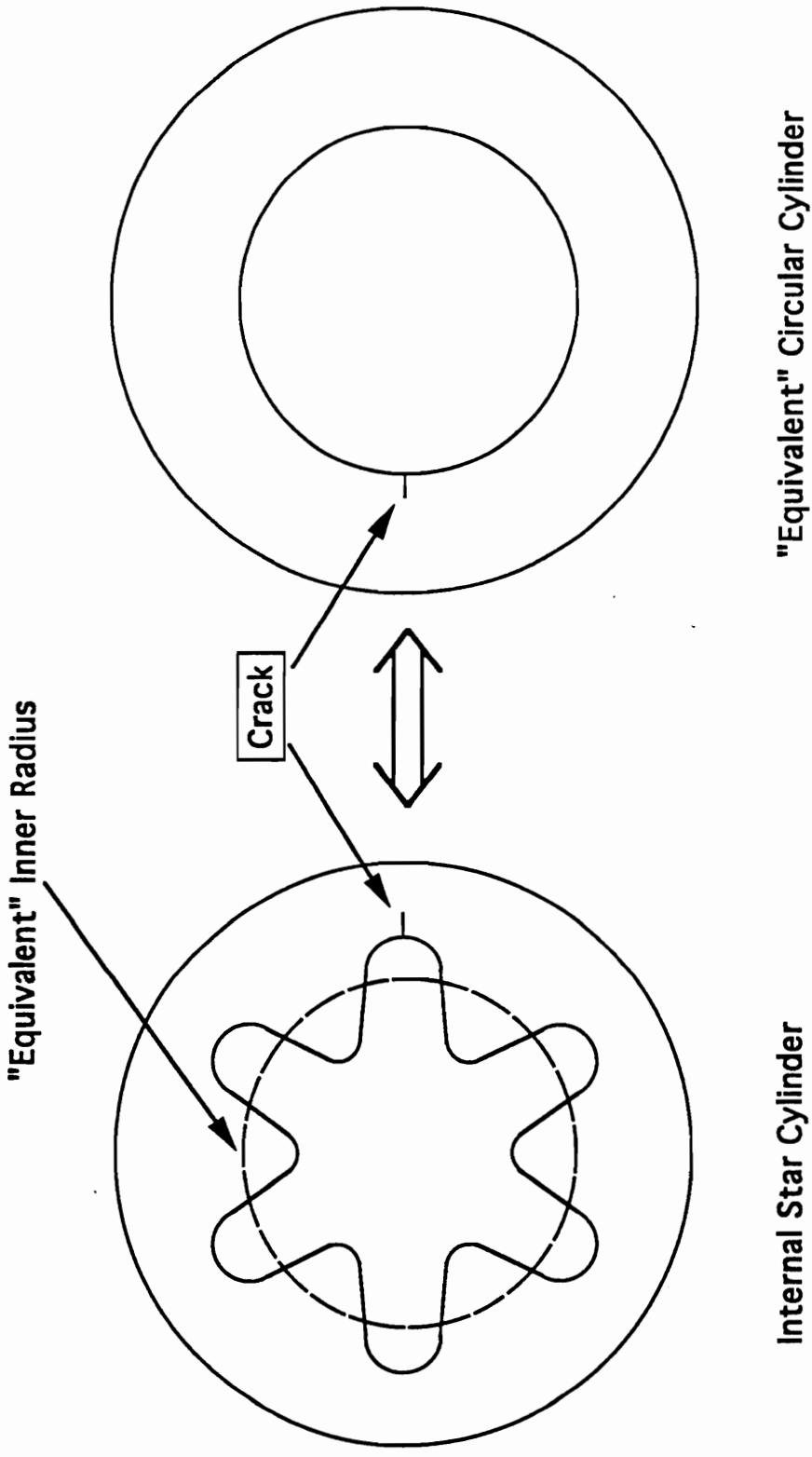


Fig.3.5: Definition of the "Equivalent" Circular Cylinder.



$$K_1 = \frac{pR}{t} \sqrt{\frac{\pi a}{Q}} F_i\left(\frac{a}{c}, \frac{a}{t}, \frac{t}{R}, \phi\right) \quad (3.1)$$

where  $p$ = internal pressure

$R$ = inner radius of the circular cylinder

$t$ = thickness of the circular cylinder

$a$ = crack depth at the mid-point

$F_i$ = boundary correction factor for a surface crack at the inside surface of an internally pressurized cylinder

$Q$ = square of the complete elliptic integral of the second kind

$\phi$ = elliptic angle (figure 3.6)

Furthermore, the boundary correction factors,  $F_i$ , can be expressed in terms of the so-called "influenced coefficients",  $G_j$ , which are dependent on the values of  $\frac{a}{c}$ ,  $\frac{a}{t}$ , and  $\frac{2\phi}{\pi}$ , i.e. crack geometry and the location of interest. The final form of  $F_i$  can be written as:

$$F_i = \frac{t}{R} \left( \frac{R_o^2}{R_o^2 - R^2} \right) \left( 2G_0 - 2\left(\frac{a}{R}\right)G_1 + 3\left(\frac{a}{R}\right)^2 G_2 - 4\left(\frac{a}{R}\right)^3 G_3 \right) \quad (2.5)$$

where  $G_j$ 's ( $j=0,1,2$  and  $3$ ) are computed from the finite element analysis and  $R_o$  is the outer radius of the circular cylinder.

In modeling the internal star grain by the "equivalent" circular cylinder, the inner radius,  $R$ , and the elliptic angle,  $\phi$ , were taken as

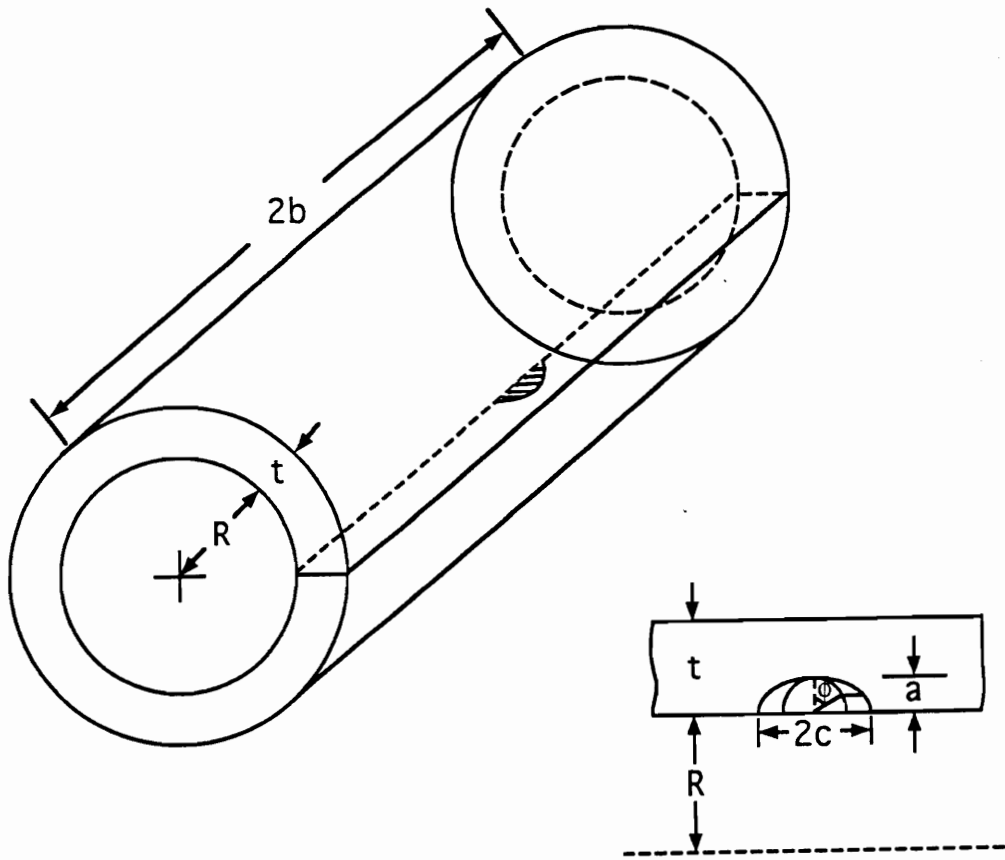


Fig.3.6: Geometry used by Newman and Raju (49).

the independent variables. To evaluate the SIF value at a certain location, one had to fix the value of  $\phi$ . Hence, by changing the value of R between the tip and valley of the star, one could achieve a series of SIF distributions with different cylinder thicknesses, among which one could choose a certain value for the "equivalent" inner radius that yielded the closest SIF distribution compared with the experimental results from the internal star grain.

This model was first applied to the deep cracks in the internal star grain and the final results were encouraging. The SIF distributions along the crack border for both curves were plotted in figure 3.7 and the largest difference was within  $\pm 5\%$ . Also, the "equivalent" inner radius was 35.8mm (1.4") which lay between the tip and the valley of the star perforation just as was expected.

The success of determining the "equivalent" inner radius for deep cracks naturally raised the intention of extending this method to cracks with shallow and moderate depths. Following the same procedure as was stated for deep cracks, by varying the inner radius of the "equivalent" circular cylinder, a similar SIF distribution (figure 3.8) was found compared with the experimental results for the moderate depth cracks in the internal star model. Although the "equivalent" inner radius was pushed closer to the star finger tip in this case, it was still bounded by the region between the tip and valley of the star.

However, the successful extension of "equivalent" circular

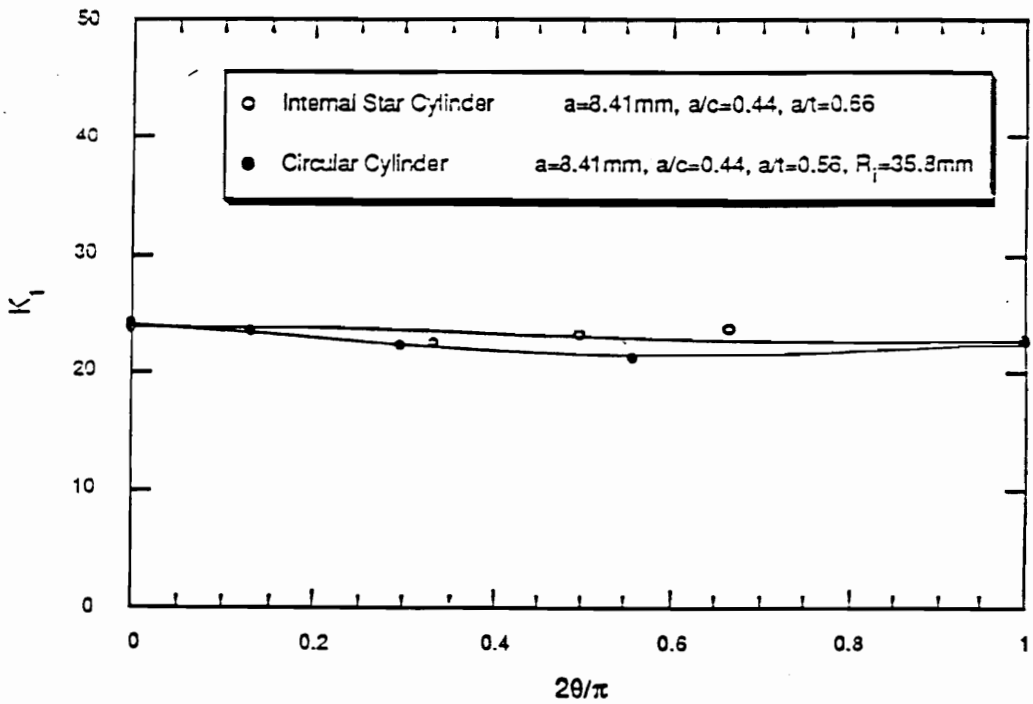


Fig.3.7: Comparison of SIF distributions of deep surface cracks in the internal star cylinder and the "equivalent" circular cylinder.

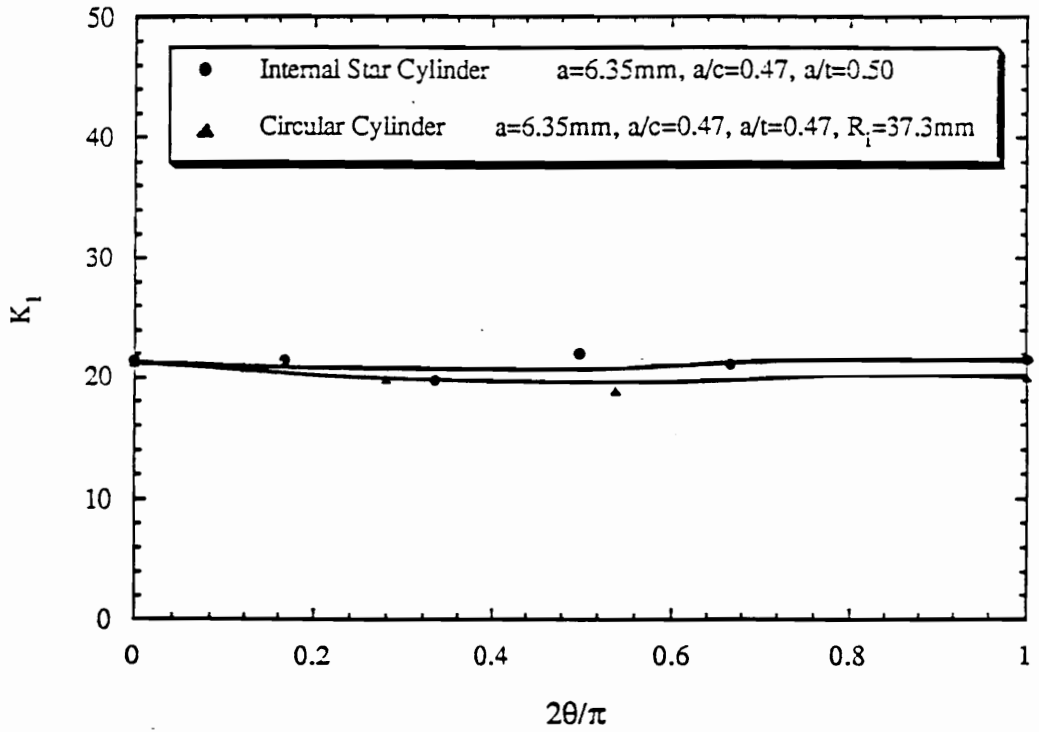


Fig.3.8: Comparison of SIF distributions of moderate depth surface cracks in the internal star cylinder and the "equivalent" circular cylinder.

cylinder concept to moderate cracks was impeded in the shallow crack problem. In fact, one can always mathematically find an "equivalent" inner radius so that the SIF distributions in the "equivalent" circular cylinder and the internal star cylinder are similar. But, at the same time, one has to keep in mind the physical consideration and practical applicability of the model. For shallow cracks, the inner radius of the circular cylinder was found to be longer than the distance from the center of the cylinder to the tip of the star, which is physically less persuasive and practically more difficult to apply. Actually, the failure of applying the "equivalent" inner radius concept to shallow cracks would not be surprising if one had not forgotten the fundamental difference between the "equivalent" circular cylinder and the internal star grain model. As was stated earlier, the replacement of the star inner periphery by a circle basically neglected the high curvature effect, especially in the region close to the star finger tip. Also, it was mentioned in the stress analysis that the difference in stress distributions along the axis of symmetry between the thick-wall cylinder solution and the internal star cylinder solution was profound within 20% of the wall thickness, which implied that, if a circle with a lower curvature were to replace the star finger with a higher curvature, large error could be introduced in the region near the finger tip, and this was exactly the case when cracks with different depths were considered. Since the moderate depth and deep cracks had propagated far away from the finger tip, the influence of the highly curved boundary

gradually diminished so that the "equivalent" circular cylinder concept could be reasonably applied. On the other hand, shallow cracks were located in the curvature-dominated region, which made the "equivalent" circular cylinder model physically invalid. Hence, further considerations are needed to deal with the shallow crack problem, which is actually one of the major motivations of the work discussed in the next two sections.

### ***3.4 Weight Function Method***

Although the "equivalent" circular cylinder model has met success for deep cracks by providing a three-dimensional SIF distribution along the crack border, its lack of physical background for shallow cracks inevitably induced further investigation to fill this void. In fact, it is natural for one, by taking advantage of the uniform SIF distribution found from the experiments, to conclude that if the SIF value could be correctly obtained at one location along the crack border, it would representatively reflect the trend of the SIF of the entire surface flaw. In most of the cases, it is the easiest to study the mid-point, i.e. the deepest penetration point, of the crack. Meanwhile, it has to be clarified that, even though only one point is to be studied, it does not mean that the pure two-

dimensional analysis is applicable. In fact, from a physical point of view, the through-thickness crack in two-dimensional analysis yields higher SIF values than what is originally expected due to the geometric difference. Hence, some adjustments need to be made in the two-dimensional analysis in order to truly reflect the three-dimensional nature. In this section, the weight function method is to be employed to fulfill the task of predicting the SIF at the midpoint of the flaw with an arbitrary depth.

The weight function method largely depends on the development of the so-called "weight function" which has been found to be a property of a cracked body geometry and independent of loading. In other words, once the weight function has been obtained for one type of loading imposed on a certain cracked body, it remains the same for another kind of loading on the same geometry provided no new load symmetry results. Thus, this method is very suitable to deal with complex loading problems where the weight function can be derived from a rather simple loading condition.

The mathematical formulation of the weight function method can be written as

$$K_{wt} = \int_0^a P(x)m(x,a)dx \quad (3.3)$$

where  $P(x)$  is the stress distribution normal to the crack surface at the crack site in the uncracked body and  $m(x,a)$  is the weight function that takes the following form for the plane strain condition:



$$m(x,a) = \frac{E}{2K_1(1-\nu^2)} \frac{\partial u_y(x,a)}{\partial a} \quad (3.4)$$

where  $K_1$  and  $u_y(x,a)$  are the SIF and crack opening displacement (COD) for the reference problem where a simpler loading condition is considered, while  $E$  and  $\nu$  are Young's modulus and Poisson's ratio of the studied body.

From equations (3.3) and (3.4), it is quite clear that  $P(x)$ ,  $K_1$  and  $u_y(x,a)$  are the three key factors in the whole formulation. For our present problem,  $P(x)$  has been obtained from the finite element analysis in chapter two, and therefore the present emphasis should be focused on deriving proper  $K_1$  and  $u_y(x,a)$ . The theoretical way of doing this is to consider the cracked internal star grain model under certain simple loading, from which  $K_1$  and  $u_y(x,a)$  can be derived without significant difficulty. However, this process may be troublesome since the COD expression may not be easily formulated, especially for the present geometry; and if one can compute  $K_1$  for a simple loading condition, say polynomial stress state,  $K_1$  for the pressure loading in the internal star grain may be directly computed by superposition of those polynomial loading conditions without knowing the expression for COD, which actually deviates from the initial intention. Hence, approximations will be adopted to simplify the process of calculating  $K_1$  and  $u_y(x,a)$ , and a correction is to be made at the end to correlate the predictions with the experimental results. In this case, a circular cylinder is chosen to be the

reference geometry.

In fact, from the "equivalent" circular cylinder model, it is seen that the "equivalent" inner radius is very close to the distance from the center of the internal star cylinder to the tip of the star finger, which suggests the adoption of this length as the inner radius of the reference circular cylinder in weight function calculations. As far as the loading is concerned, a ring specimen with a single radial notch loaded by a line force above the crack plane was selected (figure 3.9).

To model the crack shape upon loading, a conic section was assumed and the general expression (50) of a cone with the origin at the vertex can be written as:

$$\left(\frac{u}{u_0}\right)^2 = \frac{2}{m+2}\left(\frac{y}{a}\right) + \frac{m}{m+2}\left(\frac{y}{a}\right)^2 \quad (3.5)$$

where  $u$  is COD,  $u_0$  is COD at tip of the crack (CTOD),  $a$  is the crack depth,  $y$  is the coordinate originating from the crack tip and  $m$  is the conic section coefficient.

Meanwhile, Orange (50) also gave two expressions for CTOD and the radius at the crack tip,  $r$ :

$$(u_0)^2 = a r(m+2) \quad (3.6)$$

$$r = \frac{4}{\pi} \left( \frac{1-\nu^2}{E} \right)^2 K_1^2 \quad (3.7)$$

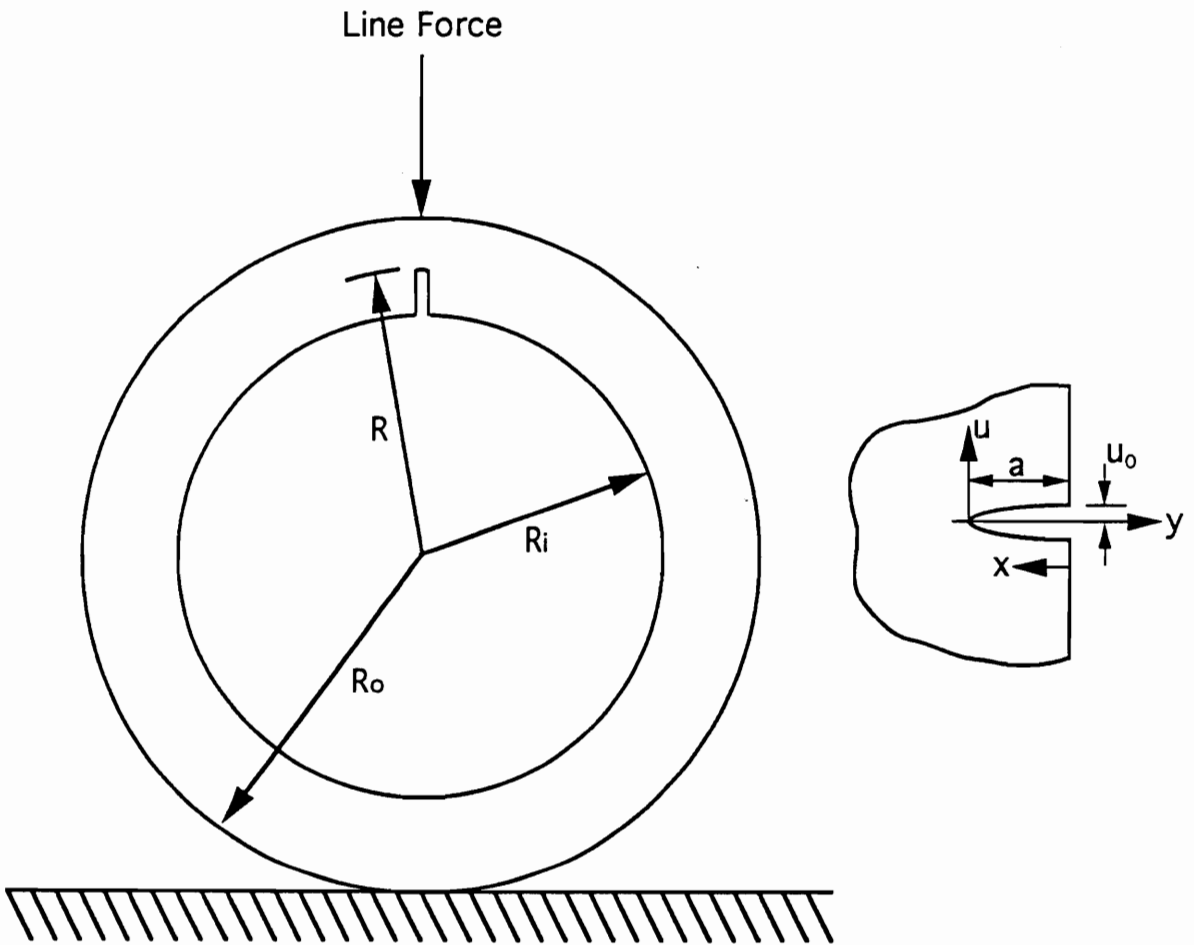


Fig.3.9: Ring specimen with a radial crack used in constructing the weight function.

It is apparent that, from equation (3.6), the conic coefficient can be expressed by

$$m = \frac{u_0^2}{ar} - 2 \quad (3.8)$$

and substitution of equations (3.7) and (3.8) into (3.5) yields

$$u^2 = \frac{8}{\pi} \left( \frac{1-v^2}{E} \right)^2 K_1^2 y + \frac{1}{2} \left( \frac{u_0 y}{a} \right)^2 - \frac{8K_1^2}{a\pi} \left( \frac{1-v^2}{E} \right)^2 y^2 \quad (3.9)$$

or

$$u = \left\{ \frac{8}{\pi} \left( \frac{1-v^2}{E} \right)^2 K_1^2 y + \left[ \frac{u_0^2}{2a^2} - \frac{8K_1^2}{a\pi} \left( \frac{1-v^2}{E} \right)^2 \right] y^2 \right\}^{1/2} \quad (3.9')$$

which is the expression for COD.

Since the differentiation of COD is needed in the weight function formulation, the following expression needs to be derived from equation (3.9):

$$2u \frac{\partial u}{\partial a} = T_1 + T_2 + T_3 \quad (3.10)$$

where

$$T_1 = \frac{8}{\pi H^2} \left( 2K_1 \frac{\partial K_1}{\partial a} (a-x) + K_1^2 \right) \quad (3.10.1)$$

$$T_2 = 2u_0 \frac{\partial u_0}{\partial a} \left( 1 - \frac{x}{a} \right)^2 + \frac{2u_0^2}{a^2} (a-x) - 2 \frac{u_0^2 (a-x)^2}{a^3} \quad (3.10.2)$$

$$T_3 = -\frac{8}{\pi H^2} \left[ \frac{2(a-x)^2}{a} K_1 \frac{\partial K_1}{\partial a} + \frac{2K_1^2}{a} (a-x) - \frac{K_1^2 (a-x)^2}{a^2} \right] \quad (3.10.3)$$

and

$$H = \frac{E}{1 - \nu^2} \quad (3.10.4)$$

It is seen that, from equation (3.10), in order to calculate  $\frac{\partial u}{\partial a}$  to obtain the weight function,  $m(x,a)$ ,  $\frac{\partial K}{\partial a}$  and  $\frac{\partial u_0}{\partial a}$  need to be evaluated first. In fact, Jones (51) considered this type of problem and provided necessary data to fulfill this task. By identifying the  $\frac{R}{R_0}$  ratios for shallow, moderate depth, deep and very deep cracks in the internal star grain, the individual weight function for different depths of cracks can be generated by combining equations (3.4), (3.9') and (3.10) with appropriate material constants:

$$m_{\text{shallow}}(x) = \frac{0.01142 + 0.5246(0.14 - x) + 0.387(0.14 - x)^2}{[0.0013(0.14 - x) + 0.0067(0.14 - x)^2]^{1/2}} \quad (3.11.a)$$

$$m_{\text{medium}}(x) = \frac{0.0221 + (0.255 - x) + 6.119(0.255 - x)^2}{[0.0031(0.255 - x) + 0.062(0.255 - x)^2]^{1/2}} \quad (3.11.b)$$

$$m_{\text{deep}}(x) = \frac{0.02835 + 1.985(0.32 - x) + 11.17(0.32 - x)^2}{[0.0050(0.32 - x) + 0.15(0.32 - x)^2]^{1/2}} \quad (3.11.c)$$

$$m_{\text{verydeep}}(x) = \frac{0.02788 + 2.504(0.37 - x) + 14.00(0.37 - x)^2}{[0.0049(0.37 - x) + 0.22(0.37 - x)^2]^{1/2}} \quad (3.11.d)$$

Knowing the weight functions and stress distribution for the uncracked specimen, one can finally evaluate the SIF's according to equation (3.3) for cracks with different depths, and the results are given in table 3.2 together with the experimental counterparts. The

Table 3.2: Comparison between  $K_{ex}$  and  $K_{wt}$  without correction.

Crack Type	a(mm)	c(mm)	a/c	a/T	$K_{ex}$	$K_{wt}$
Shallow	3.56	6.59	0.54	0.28	17.4	25.0
Medium	6.48	12.7	0.51	0.51	21.5	56.4
Deep	8.13	18.3	0.44	0.64	22.4	89.6
Very Deep*	9.40	18.8	0.50	0.74	23.7	96.7

\* Internal pressure was 41.2kPa (6.0psi) instead of 47.4kPa (6.9psi) in this case.

difference between the SIF values obtained from weight function method and experiment, i.e.  $K_{wt}$  and  $K_{ex}$ , can be attributed to several sources:

- 1) Weight function itself was generated based on two-dimensional considerations
- 2) Circular cylinder instead of internal star model was selected in constructing the weight functions
- 3) Approximation in COD expression
- 4) Numerical error in calculating  $\frac{\partial K}{\partial a}$  and  $\frac{\partial u_0}{\partial a}$  from reference (51)

Except the first one, the last three sources are all related to the consideration of avoiding the internal star geometry, which is consistent with the initial intentions and will be taken into account by a polynomial correction factor,  $f(a)$ , at the end. On the other hand, in order to compensate for the elevation of SIF due to the two-dimensional analysis of a through crack, another correction factor can be introduced based on the comparison between Bowie-Freese's solution (52),  $K_{BF}$ , for a two-dimensional radial crack and Newman-Raju's solution (49),  $K_{NR}$ , for a surface flaw at the maximum depth in a pressurized circular cylinder. The final form of this correction process is given as:

$$K_1 = f(a)K_{wt} \frac{K_{NR}}{K_{BF}} \quad (3.12)$$

where  $K_1$ =predicted SIF at the flaw's mid-point

$K_{wt}$ =SIF obtained from equation (3.3)

$f(a) = 7.82a^2 - 6.74a + 2.03$ , a polynomial correction factor to account for the use of  $u_y$  due to a through crack in a circular cylinder

It is found that, by using the formulation of equation (3.12), the SIF value at a symmetric crack's mid-point in the internal star cylinder can be estimated within 10% error. Figure 3.10 shows the variation of  $f(a) (= \frac{K_1 K_{BF}}{K_{wt} K_{NR}})$  as a function of crack depth, which yields a correlation factor of 0.98 between the fitting curve and the experimental results. In reality, the developed model can be directly applied to a crack with an arbitrary depth by identifying the proper  $f(a)$  from figure 3.10, checking  $K_{BF}$  and  $K_{NR}$  from SIF handbook and evaluating  $K_{wt}$  with the given crack depth. Apparently, the weight function method has extended the range of application compared with the "equivalent" circular cylinder model, and the error of the predicted SIF is within the engineering tolerance.

### **3.5 Notch-Root Crack Model**



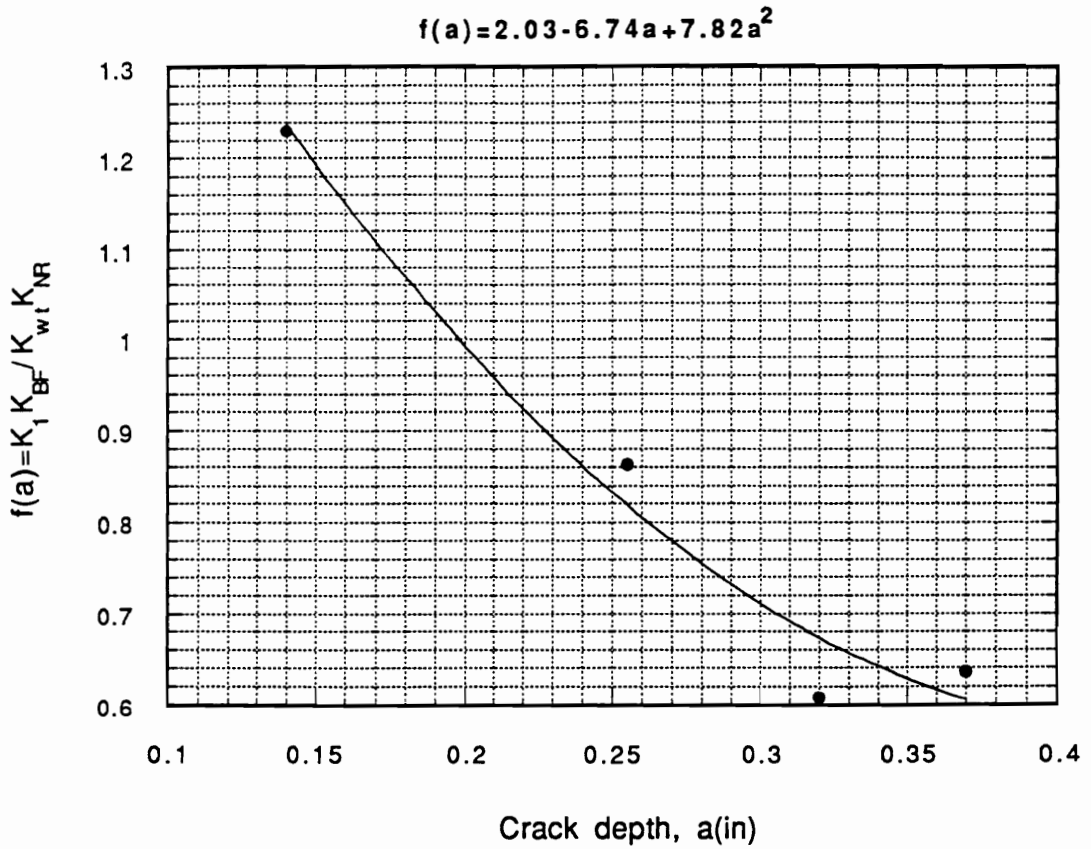


Fig.3.10: Variation of the correction function,  $f(a)$ , used in the weight function model.

Although the two presented models have provided an initial breakthrough of analytically predicting the SIF of a surface flaw in a pressurized internal star grain model, both of them were more or less based on regarding a circular cylinder as the reference problem. Geometrically speaking, these two models did not fully reflect the high curvature effect due to the star finger, since the previously used inner radius of the circular cylinder was noticeably larger than the root radius of the star finger. Thus, from a physical point of view, it might be more meaningful to develop a model in which the curvature effect is taken into account, and this is exactly the motivation for presenting the notch-root crack model.

In 1986, Murakami and his colleagues (53) proposed a solution to calculate the SIF at the mid-point of a small semi-elliptical crack at a notch root (figure 3.11). Although, in their analysis, the external loading was uniaxial tension, the local notch geometry and crack shape were very close to those of the internal star grain. Furthermore, it is the local, not global, stress fields that need to be used in the SIF calculation, and these stresses are expected to be obtained from the analysis of the relevant uncracked specimen, which makes this model extremely convenient to utilize since the stress distribution of the uncracked internal star grain was already obtained in chapter two.

In this formulation, the SIF was contributed from two parts:

$$K_1 = K_{IT} + K_{IB} \quad (3.13)$$

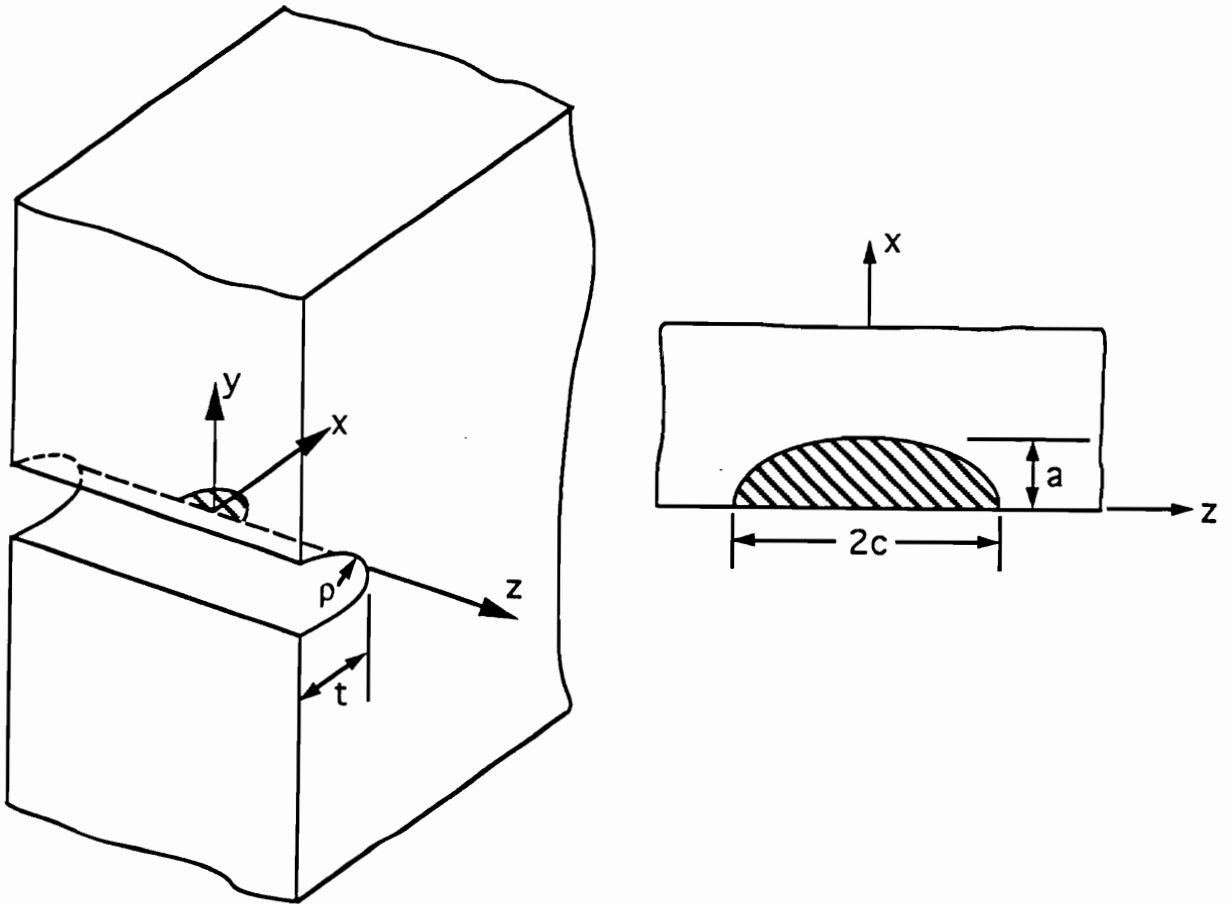


Fig.3.11: Geometry of a small semi-elliptical notch-root crack used by Murakami et. al. (53).

$$K_{IT} = \sigma_1 \sqrt{\pi a} \left[ 1.122 - 0.230 \left( \frac{a}{c} \right) - 0.901 \left( \frac{a}{c} \right)^2 + 0.949 \left( \frac{a}{c} \right)^3 - 0.280 \left( \frac{a}{c} \right)^4 \right] \quad (3.13.1)$$

$$K_{IB} = (\sigma_2 - \sigma_1) \sqrt{\pi a} \left[ 0.443 - 0.310 \left( \frac{a}{c} \right) - 0.104 \left( \frac{a}{c} \right)^2 + 0.206 \left( \frac{a}{c} \right)^3 + 0.061 \left( \frac{a}{c} \right)^4 \right] \quad (3.13.2)$$

where  $\sigma_2$  is the maximum hoop stress at the notch root and  $\sigma_1$  is the hoop stress corresponding to the deepest point of the surface flaw when the crack does not exist, while  $a$  and  $c$  are the crack depth and half crack length, respectively.

Thus, once the crack geometry is known,  $\sigma_1$  and  $\sigma_2$  can be obtained from the finite element analysis of the uncracked specimen, and further combination of equations (3.13), (3.13.1) and (3.13.2) will yield the predicted SIF for the symmetric crack with an arbitrary depth in the internal star cylinder.

Following this procedure, one can calculate the SIF values for shallow, moderate depth, deep and very deep cracks, and the final results together with the geometric factors are listed in table 3.3. It is seen that, from the table, the predicted SIF's agree reasonably well with the experimental data, especially for shallow and moderate depth cracks, which does reflect the initial desire of highlighting the high curvature effect due to the star finger. However, as the crack gets deep, the predicted value tends to be

Table 3.3: Comparison of SIF's from the experiments and the notch-root crack model at the mid-point of the surface cracks.

Crack Type	a(mm)	c(mm)	a/c	a/T	$K_1$	$K_{ex}$
Shallow	3.56	6.59	0.54	0.28	20.0	17.4
Medium	6.48	12.7	0.51	0.51	24.1	21.5
Deep	8.13	18.3	0.44	0.64	26.6	22.4
Very Deep	9.40	18.8	0.50	0.74	24.8	23.7

deviating from the experimental result, which could be attributed to the lack of back surface and a different global loading condition in the notch-root crack model.

### **3.6 Summary**

In this chapter, three models for predicting SIF of a surface crack in a pressurized internal star grain specimen have been presented. The purpose of developing these models is to provide supporting information for safety control of the propellant grain from the fracture mechanics concept. Once these models are formed based on the experimental results, they can be directly applied to the practical problems with more flexibility than the test data. In reality, if a similar problem arises, no additional experiment is necessary; instead, these analytical models are expected to offer reliable predictions of what might happen to the propellant grain upon pressurization. Meanwhile, with the three models at hand, it is necessary to address their pros and cons so that they can be complementarily used in a real design problem.

First of all, every one of the presented algorithms bears the three-dimensional or pseudo-three-dimensional nature, which is desired in simulating a surface crack behavior. Although the SIF

values at any point around the crack border can be obtained from the "equivalent" circular cylinder model, the fairly uniform SIF distribution observed from the experiments provides a physical basis for the weight function model and notch-root crack model where the SIF needs to be evaluated only at the deepest penetration point. Meanwhile, the "equivalent" circular cylinder model seems to be applicable only to relatively deep cracks where the influence of the curvature effect due to the star finger is negligible. In fact, the "equivalent" circular cylinder model served as an indirect support for the weight function model since the inner radius of the reference circular cylinder was chosen to be the distance from the center of the star grain to the finger tip, which was found to be very close to the predicted "equivalent" inner radius. Nevertheless, for certain geometries, the "equivalent" circular cylinder concept could offer a quick estimation of the SIF along the crack border, and this prediction is considered to be slightly conservative if the "equivalent" inner radius is selected to be the distance from the center of the grain to the tip of the star finger. Also, the "equivalent" inner radius is the only variable in the entire model, so that the computation is reduced to a minimum.

As far as the weight function method is concerned, it employs a pseudo-three-dimensional concept by considering only the mid-point of the surface crack and adopting the COD expression from the reference problem containing a through crack. However, the three-dimensional nature was reflected by adding two correction factors

to account for the elevation of the SIF due to the selection of a through crack as the reference and the approximation of the COD. This model covers any size of symmetric crack with an acceptable error (less than 10%) in estimating the SIF values, and is believed to have no preference towards either shallow or deep cracks. On the other hand, the weight function model needs quite a few intermediate steps to reach the final predictions, among which are finite element stress analysis of the uncracked specimen, COD approximation, weight function formulation, and evaluation of the correction factors. Also, it has to be pointed out that the polynomial correction factor for compensating the approximation of the COD is an empirical expression rather than a supplement with a strong physical basis. Nevertheless, the weight function model is a practical method that can be helpful for engineering purposes, and because of its wide range of applicability and small errors in estimation, it is a more accurate prediction algorithm compared with the "equivalent" circular cylinder model.

As was shown earlier, the stress analysis of the uncracked specimen can not only be used in the weight function model, but also was essential in the notch-root crack model. In fact, the latter formulation focuses on the local geometric characteristics of the star where high curvature is present near the finger tip, and neglects the external source of creating such a local stress condition. Although the calculations that are needed for SIF estimation at the mid-point of the surface crack are considerably



less than those in the weight function model, it gives a reasonably good prediction within the range studied. Differences in global geometry and loading conditions, which are not included in the notch-root crack model, might be influential in altering the SIF value for rather deep cracks, but this effect seemed to be tolerable up to 74% of the wall thickness. It is fair to say that the notch-root crack model is an effective approach of predicting the SIF at the mid-point of a surface crack in a pressurized internal star grain with a quite large range of applicability when different sizes of cracks are to be studied.

Finally, one common requirement that is needed to apply the three existing models is the knowledge of the crack size, which is expected to be largely dependent on the development of non-destructive testing (NDT) techniques. In fact, the progress in one field is often connected and influenced by many other factors, and further possible improvements are to be addressed in the last chapter.

## Chapter 4: Off-Axis Crack Problem

### **4.1 Problem Definition**

Although the star finger tip bears the highest stress concentration in the entire cross-section of the grain, it does not mean that the crack will always start from this location. In fact, the anisotropy and heterogeneity of the material and unbalanced loading during manufacturing, transportation and storage stages make it possible to initiate cracks off the axis of symmetry. Previously, intensive investigations were conducted on cracks along the axis of symmetry to assess the SIF distribution around the crack front, while the crack propagation path was not an important issue since the crack always followed its original direction if it was perfectly aligned normal to the specimen inner surface. In the experiments conducted on the symmetric cracks inside the internal star grain models, one of the initial cracks was slightly oriented off the axis of symmetry (figure 4.1); however, once the cracks started to propagate upon loading, it tended to reorient itself and come back to the desired path. This interesting observation actually raised the

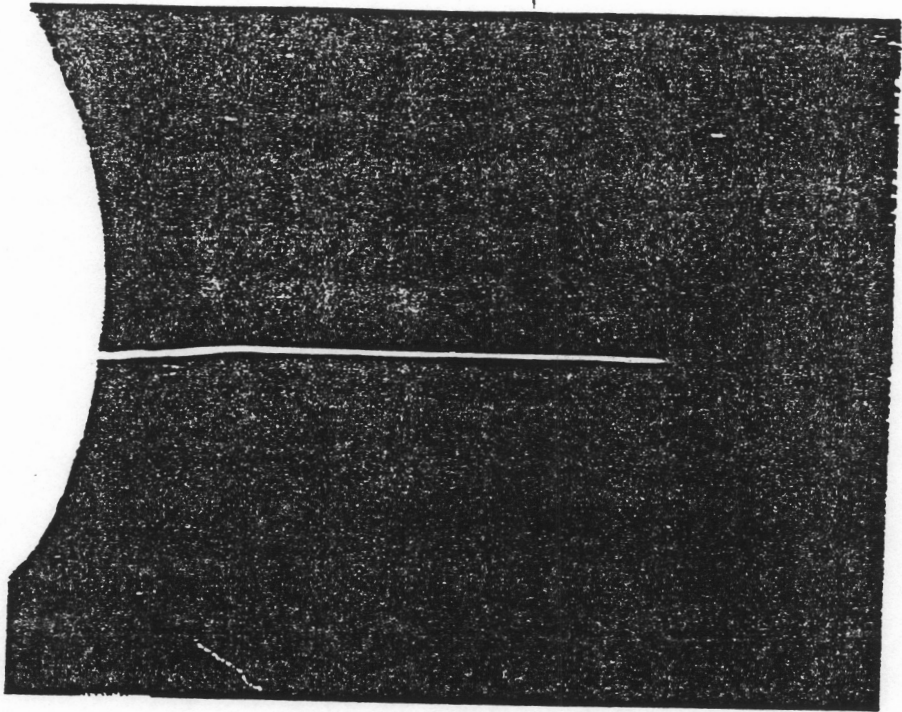


Fig.4.1: Misaligned crack propagation path from the star finger tip.

question of how the crack would propagate if it were far away from the axis of symmetry, and furthermore, how the SIF distribution would be affected by different locations of the cracks.

From the finite element stress analysis of the grain model, a sharp stress gradient was noticed close to the star finger tip and the local hoop stress even changed from tension to compression as one went from the tip of the star to the bottom of the fillet. If a crack is located in the low stress gradient region, the value of the local tangential stress (which is believed to be influential in determining possible crack growth) is quite low, or even tends to close the existing crack rather than open it up. Hence, attention should be focused on the high stressed region where the curvature is high, and, at the same time, the crack should be kept reasonably away from the finger tip so as to distinguish itself from the symmetric crack and reflect the characteristics of an off-axis crack.

Based on these considerations, the problem including a crack with an off-axis angle,  $\beta$ , normal to the inner surface of the cylinder (figure 4.2) is to be studied. In particular, the crack shape, propagation path and SIF distribution are the key issues to be investigated, and the off-axis angle is chosen to be either  $30^\circ$  or  $45^\circ$  in the present research. The initial crack is intentionally aligned normal to the inner surface so that it is also perpendicular to the local tangential stress, which is one of the principal stresses and is responsible for initial crack opening and growth.

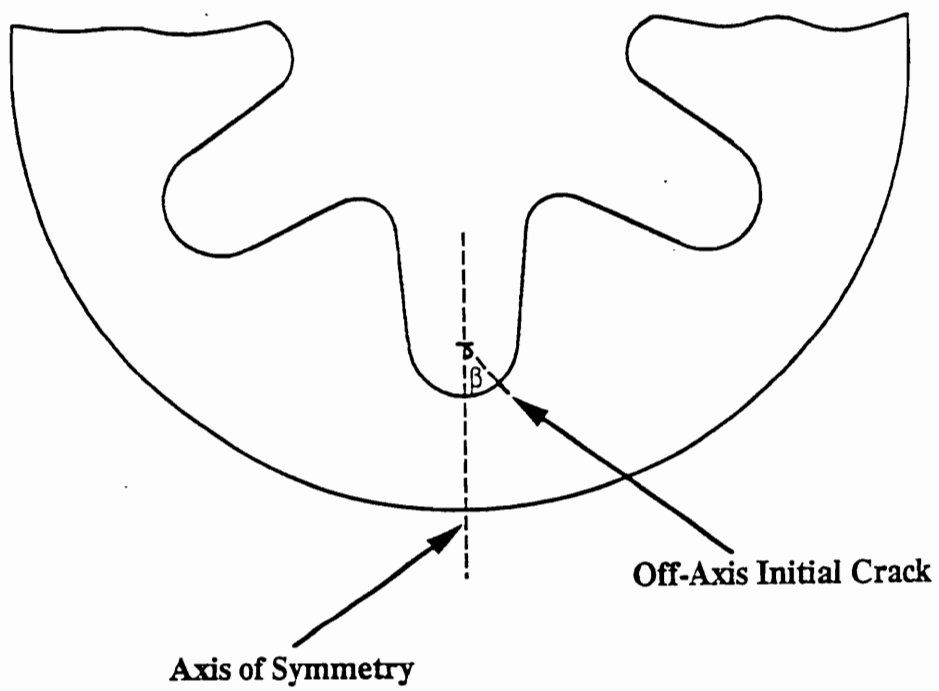


Fig.4.2: Definition of the off-axis crack problem.

## **4.2 Experimental Procedure and Data Extraction**

The first difficulty that was encountered in the off-axis crack problem was how to insert the initial crack into the grain model with a specific off-axis angle and have it normal to the inner surface as well. To do this, a specially designed fixture (figure 4.3) was made with the same holding shaft as before, but different blade alignment. In this fixture, the removable shaft head was made to hold two blades with a specific angle,  $2\beta$ , in between. These two blades have the same length of 6.35mm (0.25") but different sharpness at the tip. In fact, one of them was machined to be blunted to serve as the supporter of the other sharp blade when the holding shaft was hit by the hammer at the end. The length of the blades and the angle between them ought to be precisely measured to ensure that the initial crack enters the specimen at a right angle with either  $30^\circ$  or  $45^\circ$  off the axis of symmetry. The width of the sharp blade is chosen to be 10mm to ensure a reasonable initial crack length, which is not too small to propagate and has little influence on the fully propagated crack at the same time. Meanwhile, the head of the shaft is removable so that, by replacing the head with a different angle for holding the blades, one can make the initial crack with a desired off-axis angle.

After sealing the hole opposite to the crack location, one could bond the two ends of the cylinder to the end caps just as was done

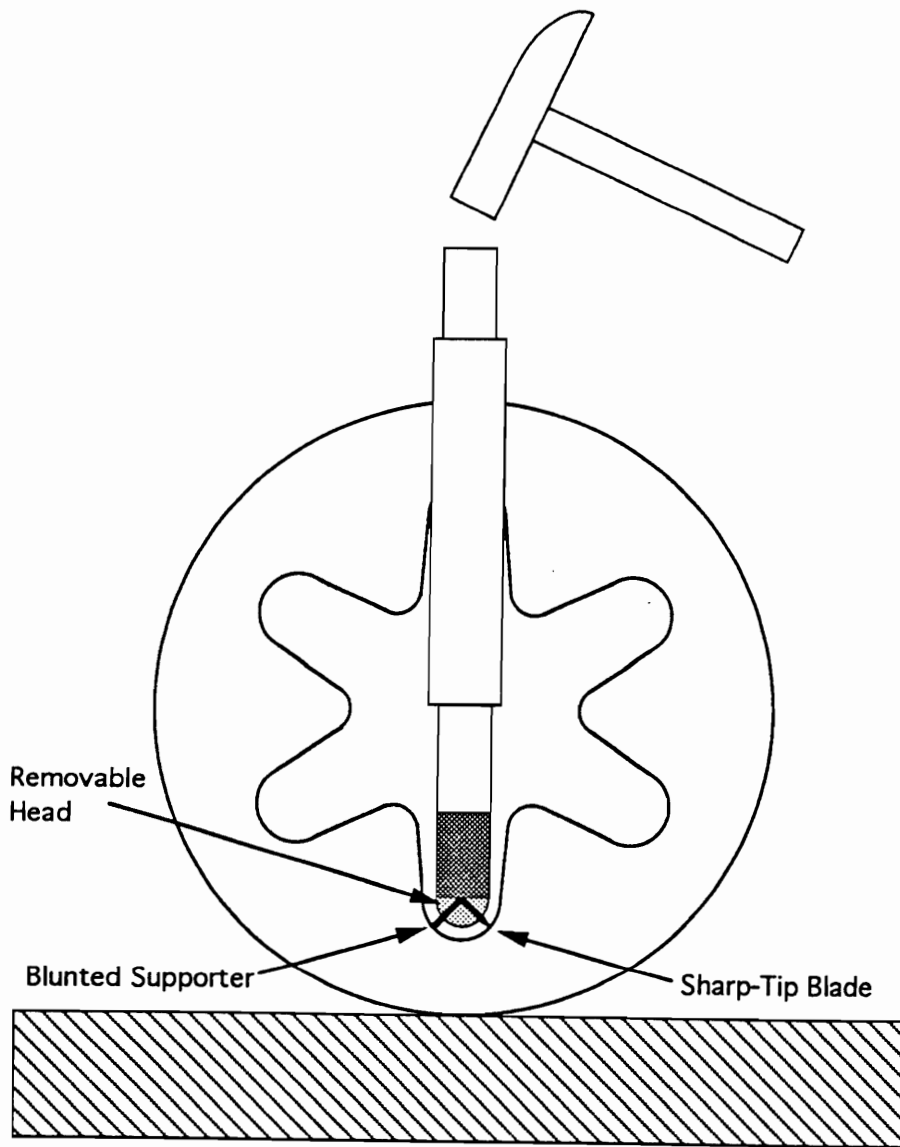


Fig.4.3: Fixtures for making off-axis cracks.

in the symmetric crack case. Then, the specimen was left in the thermal control oven for the frozen-stress cycle, during which the crack was pressurized to grow above the material's critical temperature. Since the off-axis cracks were located away from the finger tip, the degree of difficulty to grow the initial crack was expected to be higher than that of the symmetric crack, which implied higher pressure might be needed. In fact, when the specimen was fully soaked above the critical temperature, an air pressure as high as 124kPa (18psi) was applied to promote the initial growth of the starter crack until the desired crack length was reached; then the pressure was reduced to 41.2kPa (6psi) and kept constant to room temperature. This constant pressure in the later slice analysis proved to be high enough to provide adequate fringes for data extraction, and thus one need not take the risk of using higher pressure and worry about the control of the crack growth.

After the thin slices along the crack border were removed from the specimen, they were again fed into the polariscope where the Post fringe multiplication method (54) and Tardy compensation method (55) were used in tandem to extract the photoelastic data. Since the crack surface is not planar, extreme care needs to be taken in cutting the slices normal to the crack border and crack plane so that the developed two-dimensional algorithm (see appendix A) is applicable. In fact, the other preliminary requirement of applying the algorithm in appendix A is that the stress state for the propagated crack has to be Mode I. It was found that the initial off-



axis crack is not aligned perpendicularly to the local maximum principal stress direction and a mixed-mode stress state is present before the crack growth. However, earlier experiments (56) showed a change in direction once the crack began to grow, and the dominance of Mode I stress state was restored for the propagated crack. In the off-axis crack test, the isochromatic fringe pattern of the removed slices directly verified the previous argument by leaning forward on both up and down sides of the crack surface (figure 4.4).

### **4.3 Crack Propagation Characteristics**

In the process of studying off-axis cracks, five tests were conducted in total, with the test conditions being kept as close as possible for easy comparison. Among these five experiments, three of them dealt with the cracks with a 30° off-axis angle, while 45° off-axis crack were studied in the other two tests. The initial crack depth in these five tests varied from 1.27mm (0.05") to 2.54mm (0.1") and it seemed to have little effect on the final analysis since the dimensions of the initial crack were much smaller than those of the propagated crack. The initial crack was dynamically inserted into the specimen by the impact load and displayed a planar semi-

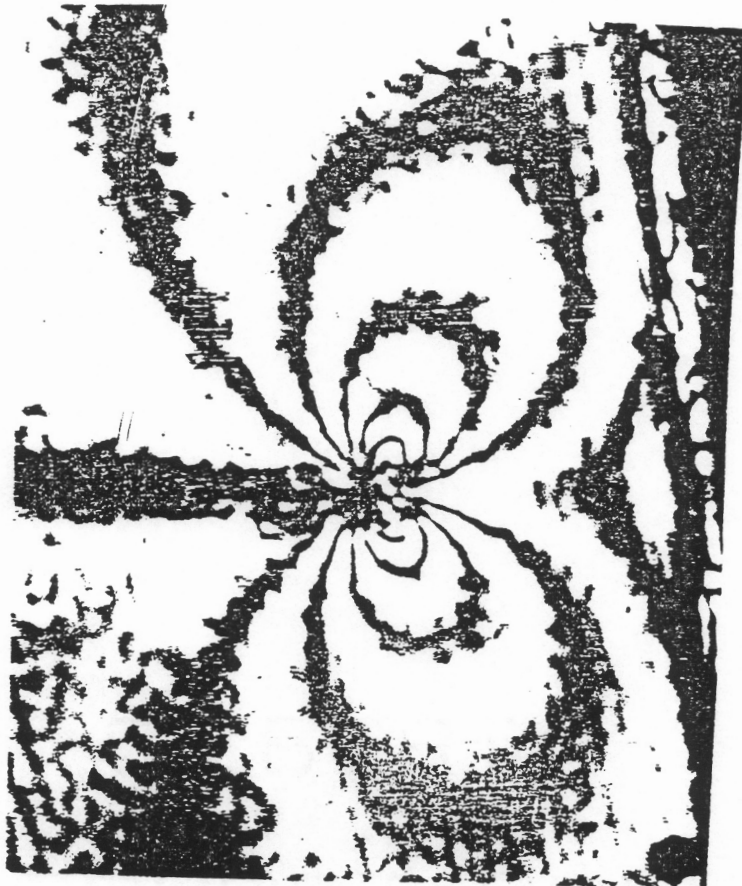


Fig.4.4: Isochromatic fringe pattern of a slice cut from the internal star grain model with an off-axis crack.

elliptical shape. Since the initial crack was formed almost instantaneously after the impact, it was not controlled by the local stress fields that were obtained from the stress analysis of the uncracked specimen, and that was why its shape and propagation path were quite different from the case of a quasi-static growth.

Upon enough loading, the initial crack started to propagate. In this situation, the crack growth was slow and, therefore, well controlled by the local stress condition. Since the initial crack plane was made off the local principal stress direction, self-adjustment was expected to occur in the gradual propagation process. Taking the propagation path of the crack's mid-point, one can have a basic idea of how the crack extends from a two-dimensional point of view. In fact, a sharp change in direction is observed in every test right after the initial crack growth (figure 4.5), and this reorientation is believed to be related to the crack's tendency of abandoning the initial mixed-mode stress condition. This phenomenon was discussed by Cotterell and Rice (57) and they concluded that the crack tended to adjust its propagation direction according to the local stress state, or more specifically, the crack would take the direction that was perpendicular to the local maximum principal tensile stress. They further stated that the larger the difference between the two in-plane principal stresses, the sooner the direction change occurred. Theoretically speaking, if the crack is aligned perfectly with the minor principal plane, it will follow its original direction. However, in reality, any kind of

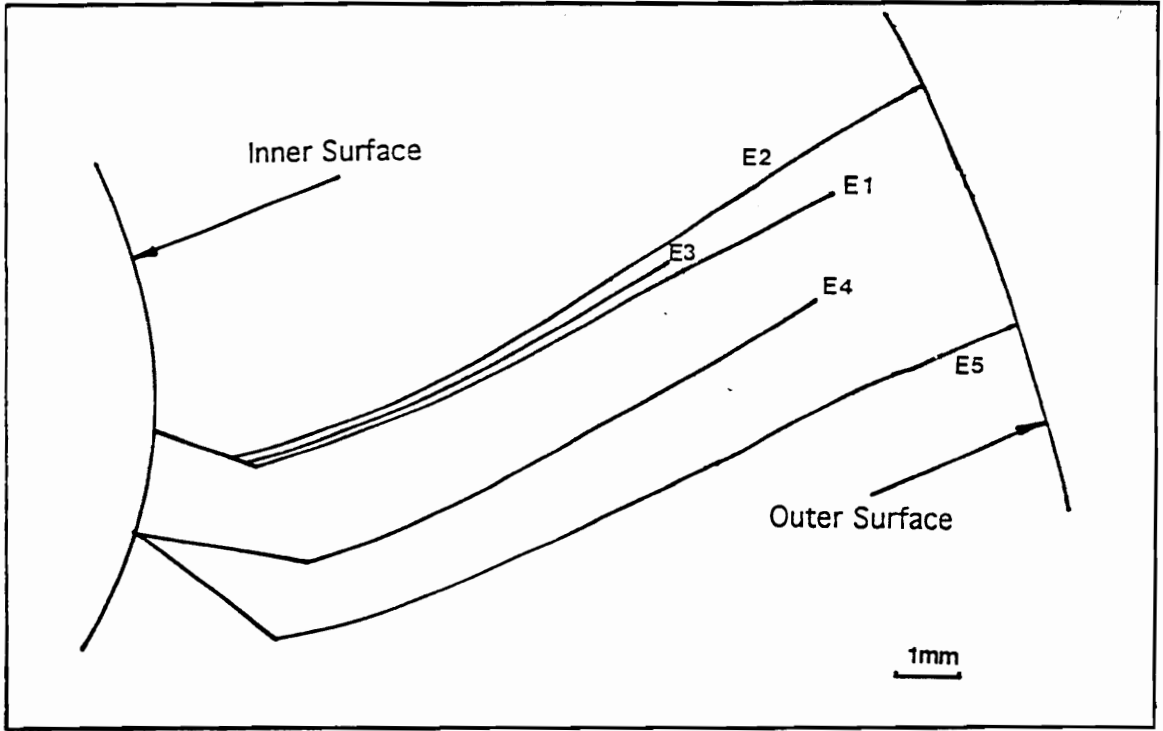


Fig.4.5: Off-axis cracks' mid-points propagation paths under internal pressure loading.

material is not isotropic or homogeneous on a microscopic level, and this small difference is more than enough to give the crack an opportunity to reorient its growth direction. Although the mid-point of the surface crack followed a curved path even after the sharp direction change, the smooth growth trajectory indicated a gradual transition of the local stress conditions, which was also verified by the previous finite element analysis.

Among these five tests, two of them involved the penetrated cracks with one for each off-axis angle, while three others treated cracks only partially through the specimen thickness. From the penetrated crack (E2 and E5), the entire propagation path of the crack's mid-point can be clearly revealed. It is interesting to notice that, by studying the crack growth path, the presence of an inflection point close to the outer boundary of the grain model may be observed. In other words, the direction to which the crack propagation path curved changed along its way to the outer surface and this made the crack not come back to the axis of symmetry before it broke through the wall. Meanwhile, by judging the cracks with the same initial inclination angle, it is seen that the small difference in the initial crack depth actually induced the difference in the entire crack propagation path; this is totally unlike the cracks made near the axis of symmetry where all the misaligned cracks would reorient themselves and grow back to the axis of symmetry even though their initial depths and inclination angles were slightly different. This observation actually suggests the presence of a

transition zone which controls whether or not the off-axis crack comes back to the axis of symmetry upon pressurization.

Undoubtedly, the symmetric crack is expected to grow in its original direction due to the presence of symmetry. Meanwhile, the axis of symmetry is the trajectory perpendicular to the maximum principal tensile direction, which leads to the intention of studying the crack propagation path based on the determination of local maximum principal stress direction of the relevant uncracked specimen. It is almost universally known that the stress distribution in an uncracked body is closely related to its possible failure, and the highest stressed area is believed to be the most probable place for the failure to start. Although theories such as the maximum normal stress criterion and the strain energy density criterion have been developed to predict crack extension direction, previous photoelastic experiments on nozzle corner cracks in a pressurized vessel (58) and the slightly misaligned cracks near the axis of symmetry in the internal star grain model suggest a close relationship between the crack growth direction and the principal stress direction in the uncracked body at the location where the crack is going to be. In the present study, the stress analysis of the uncracked model is to be applied to the analysis of not only where the crack might occur, but also how it might grow after its initiation. To do this, certain assumptions need to be made in advance:

- 1) The cracked specimen bears a similar principal stress direction distribution compared with the relevant uncracked specimen.
- 2) Upon critical loading, the crack grows perpendicular to the maximum tensile stress direction at the crack tip location.

In fact, these assumptions are also consistent with the experiments conducted on cracked plate specimens under biaxial tensile load (57) and are believed to be practical from an engineering point of view.

Since the major issue is to deal with the crack propagation path, emphasis should be focused on the principal stress direction rather than its magnitude. One way to determine local principal stress direction is to use the isoclinic fringe pattern, which displays the contours of the points which have the same principal stress direction. In practice, a 12.7mm (0.5") thick uncracked ring specimen was removed from the internal star grain model after the frozen-stress cycle so that the deformation caused by the internal pressure was preserved inside the specimen. Then, this ring was left in a plane polariscope system from which the isoclinics could be obtained with a magnification factor of 10. According to the previous discussion, an initial point was chosen at the place where the mid-point of the presumed crack was located and it was regarded as the starting point of the crack propagation trajectory. The axis of symmetry was covered by  $0^\circ$  isoclinics through the

adjustment of the specimen position. Then, by continuously changing the angle of the plane polariscope setting, a certain isoclinic fringe could be moved to pass through the previously selected point on the ring specimen. Due to the special characteristics of the plane polariscope system, the principal stress direction at the point of interest would be known to deviate from the axis of symmetry by the same angle as the rotation of the polarizer which was also the angle of isoclinics. Upon the knowledge of the local principal stress direction, the presumed crack could be extended in the major principal plane by a small amount (e.g. 1mm) based on the consideration of a minor change in the principal stress direction within this small region. The next step was to perform the same procedure of determining the principal stress direction at the newly extended crack tip so that further crack growth could be estimated. By repeating this small-segment extension process, one could obtain the entire propagation path at the mid-point of a presumed crack. Practically speaking, certain non-destructive evaluation (NDE) techniques can be employed to detect initial crack location, and later crack growth under pressure can then be predicted by the previously developed procedure. As an example, figure 4.6 shows the comparison between the predicted crack growth path and the experimental result for a 30° off-axis crack.

Reasonably close estimation of the crack growth path was achieved based on the determination of the local principal stress direction, which was considered to be normal to the crack growth



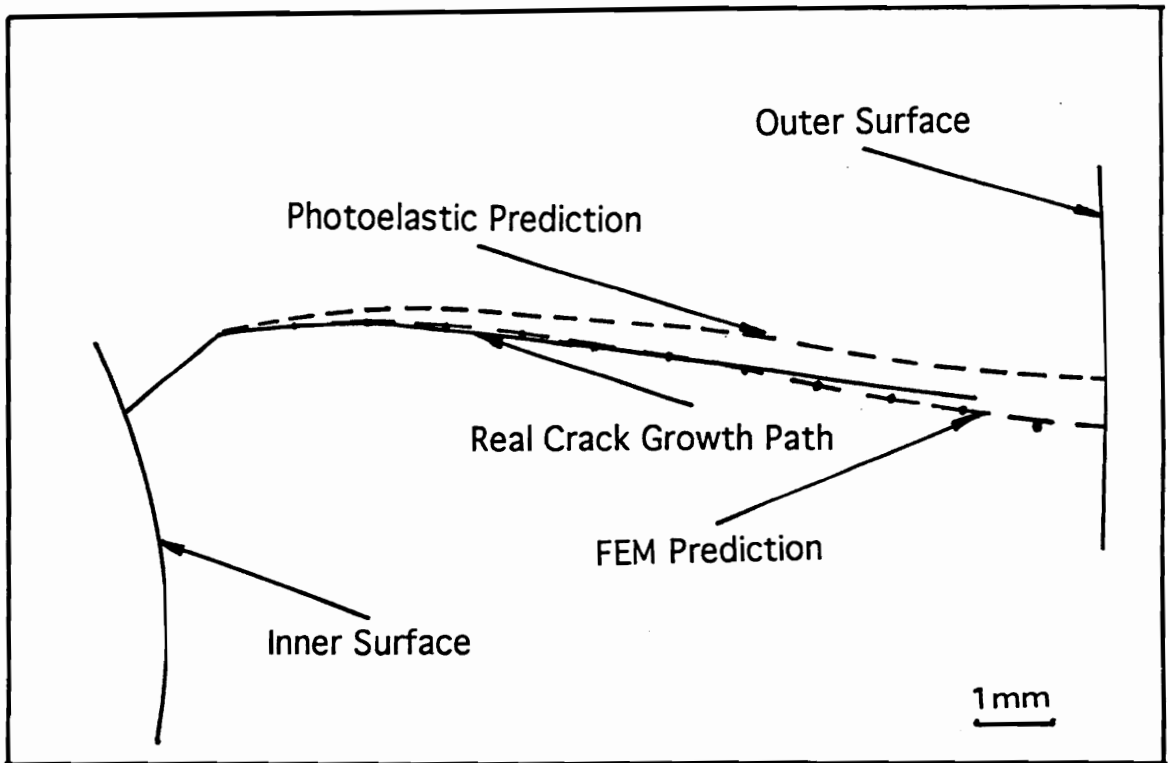


Fig.4.6: Comparison of a 30° crack propagation path between the experiment and predictions.

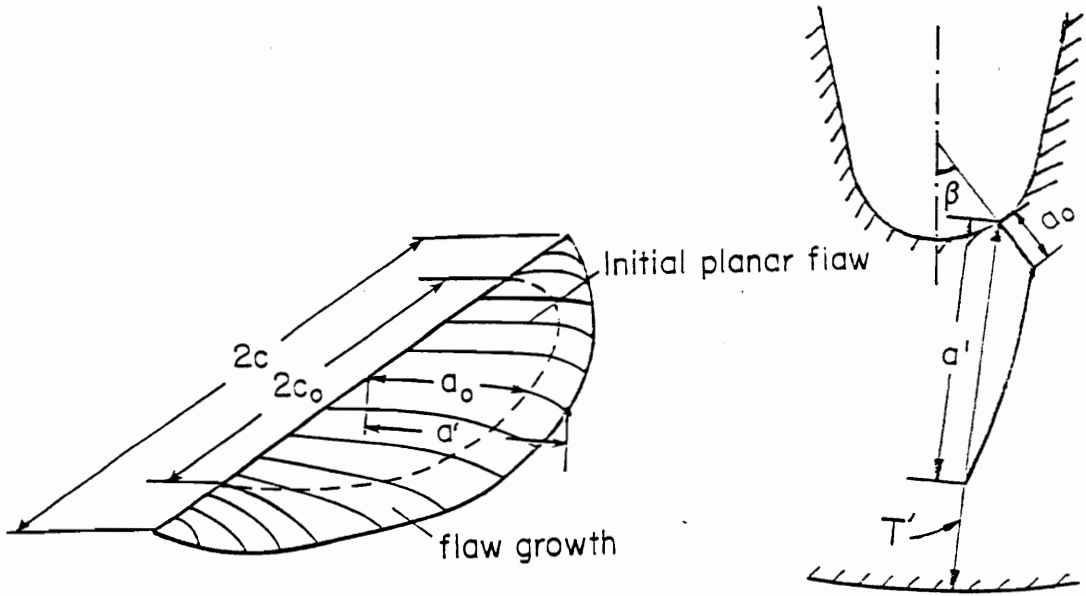
direction. The inflection point was also observed in the predicted path, which somewhat turned the crack away from the axis of symmetry. Since the normal and tangential directions at the grain's outer boundary are the principal directions, the predicted crack path should have a normal penetrating angle at the outer surface, which was quite consistent with the experimental observation for E2 and E5.

Except for the method of using isoclinic patterns to determine the local principal stress direction, the whole-field stress distribution obtained from the FEM analysis can also serve to fulfill this task. In reality, the width of the isoclinics limited the accuracy in locating the central position of the band and thus possible error could be involved. On the other hand, the FEM analysis directly provides pointwise information on the principal stress direction and is suitable to more precise estimation of the crack growth path. Following the same basic ideas as the small-segment extension model, one could use the FEM results instead of the isoclinics pattern to generate another predicted crack extension path, which is also shown in figure 4.6.

It is seen that the method of emphasizing the role of the local principal stress direction in controlling the crack propagation path has met success from an engineering point of view. The use of isoclinic patterns can provide a quick look of where the crack will propagate upon pressurization, and this method is considered to be a

practical way of foreseeing the behavior of an existing flaw when it is combined with proper NDE techniques. FEM analysis is a more accurate method in determining the local principal stress direction, but it requires more time in formulating the problem, writing computer codes and analyzing the final output. Thus, the FEM method is recommended to serve as a backup to the photoelastic prediction in the small scale grain problem where the minor error due to the photoelastic estimation can be tolerated, while for the large scale grain problem, FEM results might be essential in a total safety control procedure and is worthwhile to be adopted to predict possible crack growth paths since more reliable results are expected in this case.

When considering a surface crack, one needs to study its behavior not only in the depth direction, as should be done for a through crack, but also in the length direction, which accounts for the three-dimensional nature of the surface flaw. In fact, the off-axis crack shows a doubly-curved surface as it propagates. In other words, crack growth in both the depth and length directions was curved and yet illustrated a symmetric pattern with respect to the center line (figure 4.7). Since the crack did not grow in a straight line, the conventional crack depth concept does not hold in this case. As a geometric parameter to describe the crack shape, the pseudo-crack depth,  $a'$ , is defined as the distance from the inner penetrating point to the tip of the crack (figure 4.7). This crack depth is easy to measure, and actually very close to the total length of the initial



Early Crack Growth  
(a)

Path of  
Crack Midpoint  
(b)

$2c_0, a_0$  - Plane Starter Crack Dimensions.  
 $a'$  - Projected Final Crack Depth.

Fig.4.7: Off-axis crack shape and definitions of the geometric parameters.

crack and the propagated section since the initial crack is short and the curved path has a very small curvature. By using this pseudo-crack depth, the major geometric parameters in determining the crack shape can be calculated and are given in table 4.1. It is noticed that, for 30° off-axis cracks where the off-axis and penetration angles of the cracks are the same, the ratio of  $\frac{a'}{c}$  varies by a small amount even though the variation in  $\frac{a'}{l}$  is large. More specifically, the 30° off-axis cracks bear the range of change in  $\frac{a'}{c}$  of 12%, while the difference in  $\frac{a'}{l}$  is up to 47%. In fact, this small variation in  $\frac{a'}{c}$  suggests a self-similar growth pattern for different stages of crack propagation. Meanwhile, the  $\frac{a'}{c}$  ratio seems to increase as the crack moves far away from the axis of symmetry. The average value of  $\frac{a}{c}$  or  $\frac{a'}{c}$  rises from 0.49 for symmetric cracks to 0.65 and 1.0 for 30° and 45° cracks, even though the pseudo-crack length,  $a'$ , is slightly less than the total distance from the starting point to the end of the curved path. Physically speaking, the crack growth in its length direction is largely controlled by the stress condition at the inner surface of the grain model. Since the local principal stress directions are normal and tangential to the inner border with the initial crack being made along the longitudinal direction, the crack extension in its length direction is not expected to change, and actually it did not change, from its original alignment. On the other hand, a continuous change in the principal

Table 4.1: Geometric parameters of the off-axis cracks.

Test I.D.	a'(mm)	c(mm)	T'(mm)	a'/T'	a'/c
E1	11.4	18.5	13.0	0.88	0.62
E2	13.2	19.1	13.2	1.0	0.69
E3	7.87	12.4	13.0	0.61	0.63
E4	11.2	14.0	13.7	0.82	0.80
E5	13.9	11.3	13.9	1.0	1.23

stress direction induces the curved propagation path of the crack's mid-point, which, at the same time, turns the crack into a higher stressed area for easier extension. Because the degree of difficulty for crack growth in its length direction increases as the crack is located further away from the axis of symmetry, while self-adjustment in the depth direction alleviates this tendency of rising difficulty, the ratio of  $\frac{a}{c}$  or  $\frac{a'}{c}$  is accordingly expected to increase with larger off-axis angle. In practice, one has to keep in mind the alteration of  $\frac{a'}{c}$  for different types of cracks so that correct estimation of crack size could be determined. In fact, the observation of varying the  $\frac{a'}{c}$  ratio is also useful to control crack propagation in conducting the experiments since the crack length is normally easy to measure, and thus relevant crack depth can be deduced from the obtained trend of how  $\frac{a'}{c}$  changes with the off-axis angle. Finally, although the crack propagation process was assumed to be quasi-static and the crack shape was expected to be fully developed at any instant, various degrees of difficulty for crack propagation in different directions might cause the first growth along the inner border of the crack and leave the extension at the surface behind. From the experiments, small bulges were observed occasionally at the intersection between the crack and specimen inner periphery, which could have resulted from the previously mentioned phase lag between the crack growth along its inner boundary and at the surface.

#### **4.4 SIF Determination for Off-Axis Cracks**

The study of the crack propagation path illustrated how the off-axis flaw could grow when the pressure loading was high enough. It still remains a problem of determining when the crack will grow, or in other words, under certain loading conditions, whether the existing crack will grow or not. It is known that, from a fracture mechanics point of view, the growth of a crack is mainly controlled by the value of the critical stress intensity factor, and the comparison between the SIF of an existing crack and the critical value basically forecasts future crack growth behavior. Hence, determination of the SIF values is essential in failure analysis of a cracked body, and more specifically, the SIF distribution around the surface flaw border for the internal star grain model is expected to reveal the three-dimensional effect on the SIF variation and provide a valuable data base for global structural integrity assessment.

The first problem that was encountered in studying the off-axis crack arose from determining the fracture mode. The lack of symmetry and deviation from the local principal stress direction of the initial crack inevitably caused a mixed-mode stress condition around the crack border. The major concern was whether this initial mode would be preserved or replaced as the crack started to propagate. This is important not only in characterizing the stress conditions near the crack tip, but also in determining what type of



algorithm should be applied to the data analysis. Generally speaking, the determination of the SIF for a mixed-mode condition involves the separation of different modes of the SIF by using both the locations and orientations of the fringe loops in the near-tip region (59), while the pure opening mode (Mode I) algorithm only focuses on the locations of the fringes since the extracted data are to be obtained along the same direction which is normal to the crack surface. In the present case, by checking the fringe patterns preserved in the slices around the crack border (see typical pattern of figure 4.4), one could verify that the off-axis cracks reoriented themselves after initial propagation to eliminate the mixed-mode stress state, and from then on, they were controlled by the opening mode all the way to the end. Meanwhile, the forward-leaning fringe loops show a small size difference above and below the crack surface, which is believed to result from the slight non-uniformity of the non-singular term in the stress formulation, or physically speaking, this size difference of the fringe loops suggests a slightly curved growth path if the crack is to extend.

No matter whether the non-singular term in the stress component expression is uniform or not along the line that is normal to the crack surface, the Mode I algorithm for extracting the SIF from the photoelastic data still holds since the value of the SIF is really controlled by the singular stress field. By collecting a series of photoelastic readings from the slice, one could compute the maximum in-plane shear stress based on the stress-optical law, and

further application of the developed algorithm for the Mode I stress state would lead to the SIF value for each slice by identifying a certain linear zone in which the theory of LEFM was valid. Since the slices were thin and distributed along the crack border, the obtained SIF's could be regarded as pointwise values with negligible error, from which the SIF variation around the crack front could be assessed.

Tables 4.2 and 4.3 list the range of the linear zone and the average values of the SIF,  $K_1$ , from both sides of the cracks for each slice with the off-axis angle being  $30^\circ$  and  $45^\circ$ , respectively. The variation of normalized SIF,  $\frac{K_1 \Phi'}{\rho(\pi a')^{1/2}}$  for the five off-axis crack tests are also graphically shown in figures 4.8 and 4.9 from the intersection point of the crack with the inner surface of the grain model to the deepest penetration point. It is noticed that, for both  $30^\circ$  and  $45^\circ$  off-axis crack tests, the previously observed uniform SIF distribution for symmetric cracks is broken down, especially for relatively deep crack tests (E1 and E4) where  $\frac{a'}{T}$  exceeds 0.80. The general trend of SIF variation in the off-axis crack tests shows a relatively high value at the surface, which is followed by a drop in the range around  $\theta=15^\circ$  to  $30^\circ$  and then a rise to the crack's mid-point. It can be concluded that, from both figures 4.8 and 4.9, that maximum SIF occurs either at the surface or the deepest penetration point of the off-axis crack, and as the crack gets deeper into the body, the gap between the maximum and minimum SIF's also expands

Table 4.2: Linear zones and SIF values for three 30° off-axis cracks.

Slice I.D.	E1-0°	E1-15°	E1-30°	E1-45°	E1-60°	E1-90°
Linear Zone ( $r/a$ ) <sup>1/2</sup>	.23-.31	.17-.25	.19-.25	.16-.24	.19-.28	.13-.23
K <sub>1</sub>	28.5	25.0	24.2	29.4	31.4	31.5
K <sub>1</sub> (nor)	5.15	4.52	4.37	5.31	5.68	5.70

Slice I.D.	E2-0°	E2-15°	E2-30°	E2-40°	E2-60°	E2-90°
Linear Zone ( $r/a$ ) <sup>1/2</sup>	.22-.28	.20-.28	.20-.27	.19-.26	---	---
K <sub>1</sub>	33.2	29.1	29.4	30.0	---	---
K <sub>1</sub> (nor)	5.76	5.04	5.09	5.20	---	---

Slice I.D.	0°	15°	30°	45°	60°	90°
Linear Zone ( $r/a$ ) <sup>1/2</sup>	.25-.34	.23-.32	.25-.33	.26-.36	.25-.35	.21-.29
K <sub>1</sub>	23.8	20.4	20.1	19.3	20.7	21.3
K <sub>1</sub> (nor)	5.23	4.49	4.41	4.24	4.55	4.68

Table 4.3: Linear zones and SIF values for two 45° off-axis cracks.

Slice I.D.	E4-0°	E4-15°	E4-30°	E4-45°	E4-60°	E4-90°
Linear Zone ( $r/a$ ) <sup>1/2</sup>	.22-.33	.18-.29	.23-.34	.22-.35	.26-.35	.23-.34
K <sub>1</sub>	28.9	20.9	23.4	23.4	25.2	28.8
K <sub>1</sub> (nor)	5.78	4.17	4.68	4.68	5.03	5.75

Slice I.D.	E5-0°	E5-15°	E5-30°	E5-45°	E5-60°	E5-90°
Linear Zone ( $r/a$ ) <sup>1/2</sup>	.15-.26	.13-.23	.16-.29	.17-.29	.15-.27	---
K <sub>1</sub>	19.8	11.7	15.7	17.2	18.0	---
K <sub>1</sub> (nor)	4.44	2.62	3.52	3.85	4.03	---

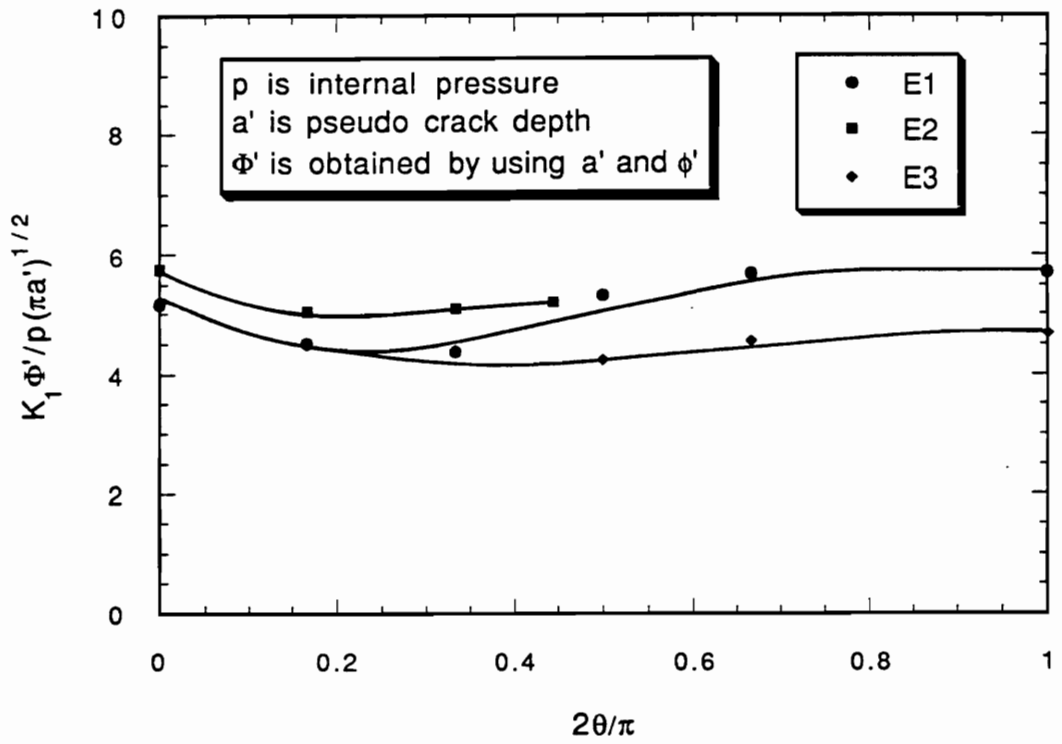


Fig.4.8: Normalized SIF distributions for three 30° off-axis cracks.

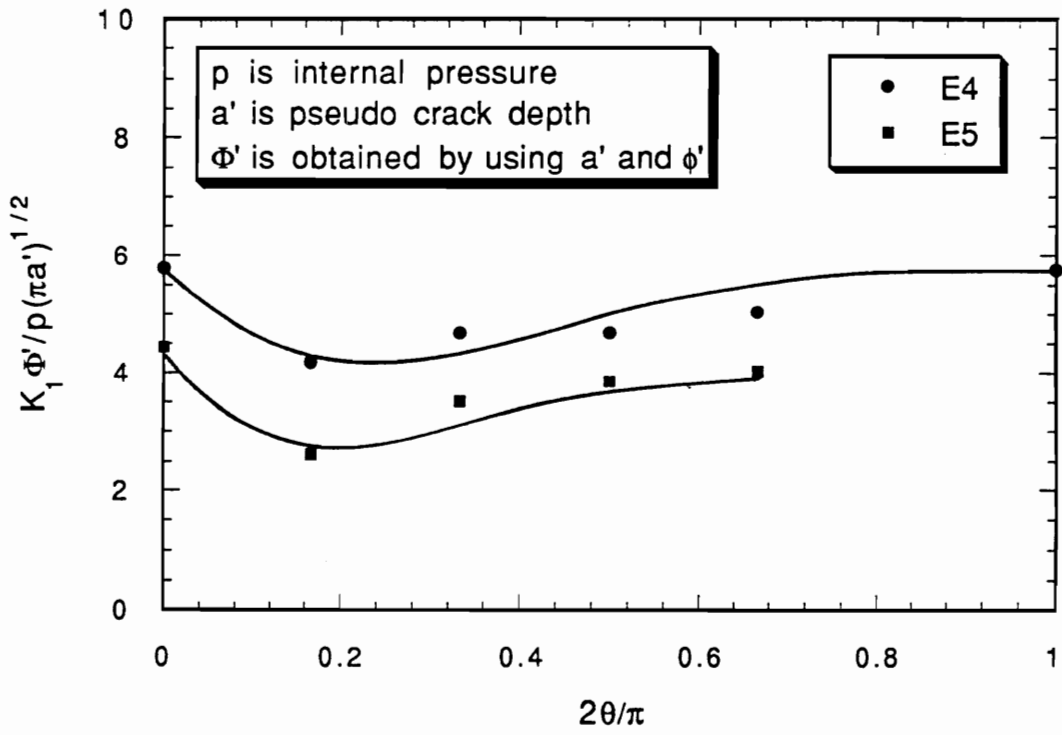


Fig.4.9: Normalized SIF distributions for two 45° off-axis cracks.

up to as large as 51%. Although the penetrated crack tests do not show the SIF variation near its mid-point due to the absence of the necessary slices, the first half of the distribution is consistent with the general trend. Meanwhile, considering the tests with the same off-axis angle, the larger crack usually possesses a higher SIF, which is quite reasonable since these cracks are regarded to be easier to drive compared with the shallower ones. Furthermore, the elevation of the SIF in the mid-portion of the deep cracks can be attributed to the back surface effect, which is quite profound for the crack front when  $\theta$  is larger than  $45^\circ$ . To compare the symmetric cracks with the off-axis ones, E3 is a good selection since it has a similar crack size (or  $\frac{a'}{T}$  ratio) as the deep symmetric cracks. In fact, the largest variation in the SIF for deep symmetric cracks up to 74% of the wall thickness is only  $\pm 7\%$  which is still smaller than that of E3 where a  $\pm 11\%$  variation in SIF is observed even though the ratio of  $\frac{a'}{T}$  is only 0.61 in the latter case. It seems that the uniformity of the SIF distribution for a symmetric crack is broken by a variation of pushing higher values to the mid-portion and surface of the crack, while leaving lower values in between as the crack is moved away from the star finger tip. Moreover, this developed nonuniform SIF distribution has the tendency of increasing variation as the off-axis angle increases, which really serves as the second factor, in addition to the flaw depth, to influence the three-dimensional SIF values around the crack border.

Another thing that is observed from figures 4.8 and 4.9 is the drop of the SIF distribution for the penetrated crack with the off-axis angle of  $45^\circ$  (E5). The two possibilities that might cause this phenomenon are the loading condition and the crack geometry. Since the same internal pressure was maintained during the cooling process of the frozen-stress cycle for each test, the main attention should be directed towards the difference in crack geometry. Comparing the two penetrated crack tests, E2 and E5, one can notice at least two geometric differences. Firstly, the locations of these two cracks which include the off-axis angle and the penetrating angle are different. This location-related influence causes the cracks to follow different propagation paths and form different shapes. Thus the effectiveness of adding the pseudo shape factor,  $F'$ , is reduced since the elliptic angle,  $f'$ , and the pseudo crack depth,  $a'$ , are defined differently in these two cases. Secondly, although both E2 and E5 dealt with penetrated cracks, the aspect ratio,  $\frac{a'}{c}$ , which reflects the crack shape is dramatically different (figure 4.10). It is noted from table 4.1 that the pseudo crack depths are similar in these two cases, while the growth in the length direction is significantly impeded in E5. The low aspect ratio for E2 actually makes it more like a through crack compared with E5, which might induce the gap of the SIF distribution between the two. It ought to be mentioned that these explanations are based on the experimental data at hand, and more tests would be helpful to further confirm the present conclusions.



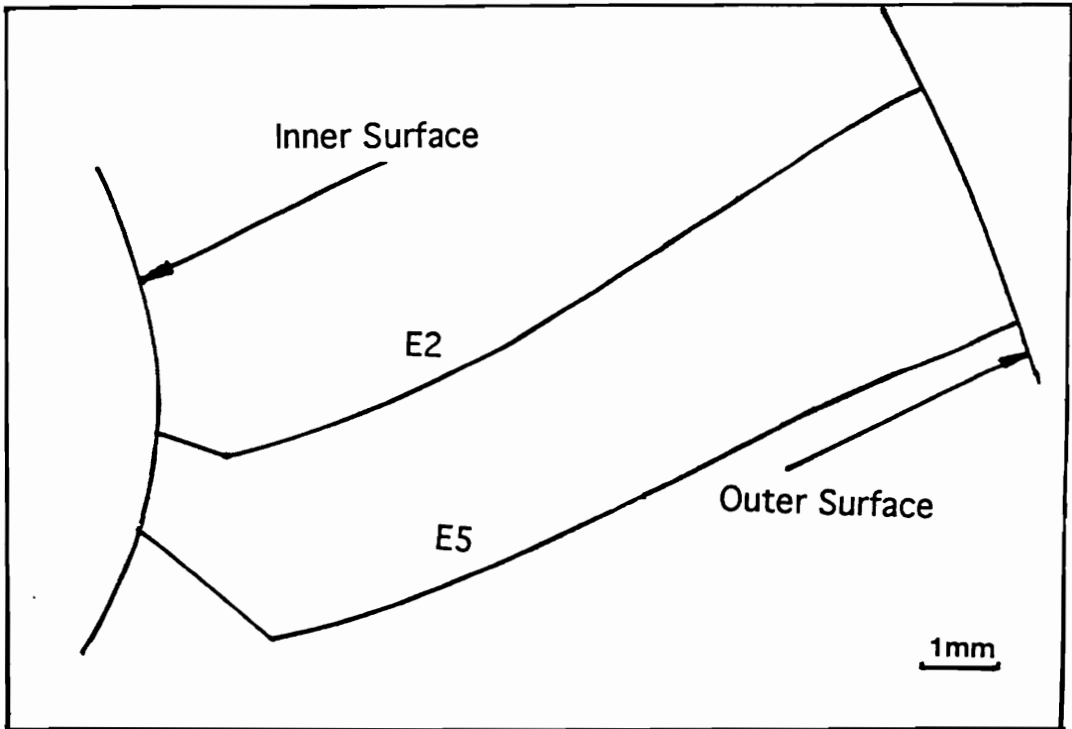
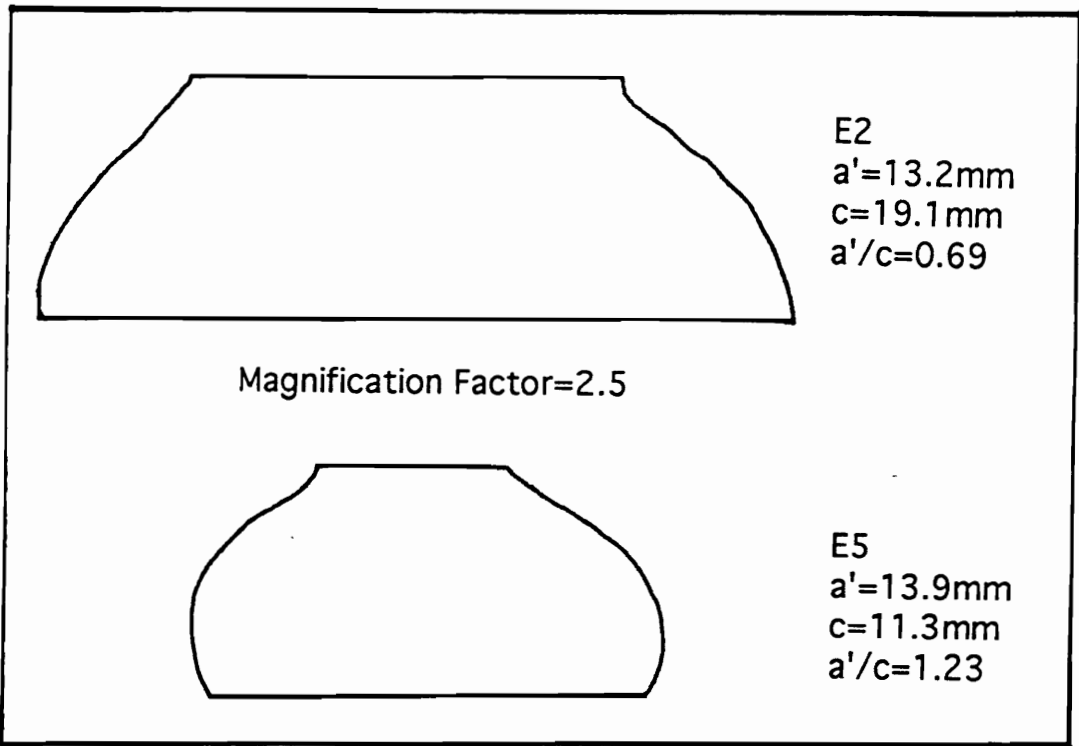


Fig.4.10: Comparison of crack shape and location between the two penetrated cracks, E2 and E5.

## Chapter 5: Closure

### **5.1 Summary**

After reviewing the development of solid rocket propellants, the first chapter evaluated the present status of propellant research and some major concerns about propellant safety control. It was pointed out that material characterization and geometry evaluation would be the two core areas that needed intensive study. The investigation of propellant material can not only determine its material properties but also its failure modes under different simulated loading conditions. Both analytical models and experimental efforts have been made toward better understanding of the material's behavior from the manufacturing stage, through processing, transportation and storage conditions, till the final ignition and burning period. It is beneficial, in the experiments, to consider various environmental and loading conditions so as to clearly quantify the influence on material response from the individual factors. On the other hand, the study concerning the interaction of all the parameters that might be present in the real

situation needs to be strengthened in the experimental propellant research. Meanwhile, analytical considerations are directed towards precise characterization of the material's chemical and mechanical behavior on both micro and macro structural levels. Through the processes of changing the propellant's chemical composition and its mechanical properties, both the ballistic performance and structural integrity of the solid rocket propellant grain can be improved. A more general and realistic constitutive relationship is needed to replace the widely used linear viscoelastic theory to quantify propellants' time-dependency nature.

As far as the propellant grain geometry is concerned, stress analysis is essential, and recent developments of computer application have matured the necessary codes in conducting stress and strain analysis of a grain geometry from both two-dimensional and three-dimensional points of view. The results obtained from the computer output can provide a reasonable basis for critical evaluation of the propellant grain's safety condition and further optimization in structural design. The weak part of studying the role of propellant grain geometry is considered to be the failure analysis, especially surface cracks in complex geometries where a three-dimensional effect is involved. The present research was initiated to launch the first attack on the three-dimensional fracture problem by investigating surface cracks' growth in an internal star grain geometry.

Stress analysis was first conducted by using both experimental and numerical methods to evaluate the stress distribution in the cross-section due to the internal pressure, especially the stress concentration effect at the star finger tip. It was found that the stress concentration was mainly a regional effect around the star finger tip where the curvature was high. In the thickness direction, the high hoop stress at the finger tip died out to a magnitude that was close to Lamé's circular cylinder solution beyond 20% of the wall thickness, which implied the possibility of adopting an "equivalent" circular cylinder model to simulate the internal star geometry when considerations were mainly focused far away from the star finger tip. Along the inner periphery of the grain model, the hoop stress experienced a high gradient transition in the curved region and even changes to compression between the tip and valley of the star. This phenomenon actually revealed the changing degree of difficulty to introduce possible failure under the same pressurized condition along the grain inner border, and the star finger tip was apparently one of the critical areas in which further fracture analysis was needed. Meanwhile, the whole-field stress distribution was obtained from FEM calculations and these results proved to be beneficial in predicting the crack propagation path and estimating the SIF distribution for cracks on the axis of symmetry.

In order to apply the fracture mechanics concept to the critical area in the grain models, a series of photoelastic

experiments were conducted on surface cracks emanating from the star finger tip. Cracks of different depths were analyzed and the SIF distribution showed a very small variation around the flaw border, especially for the fully-developed deep cracks. These experimental data were further used in formulating three analytical models that could be regarded as SIF prediction methods for symmetric cracks with arbitrary depths. The "equivalent" circular cylinder model was mainly designed to deal with medium depth and deep cracks, since the high curvature effect due to the star finger was much less influential compared with the near-tip region. By fixing the crack size and varying the inner radius of the "equivalent" circular cylinder, one could find a similar SIF distribution for medium depth and deep cracks in the circular cylinder model compared with the experimental results for the internal star grain specimen, and the adopted "equivalent" inner radius was evaluated to be close to the distance from the center of the cylinder's cross-section to the star finger tip. Taking advantage of the nearly uniform SIF distribution, the weight function model and notch-root crack model were also developed to predict the SIF value at the deepest penetration point of the surface crack. These two formulations took into account the three-dimensional nature of a surface crack and could offer a close estimation of the SIF within a margin of  $\pm 7\%$ . In the weight function model, the major approximation came from selecting the reference problem for which the COD and SIF solutions were expected to be available. This difficulty was avoided by first dealing with a two-

dimensional circular cylinder solution, and then adding two correction factors to mitigate the initially induced errors. The notch-root crack model focused on the local stress distribution rather than global loading conditions, and the highly curved local geometry was also emphasized in this method. The final results seemed to have confirmed that this idea was practically applicable to estimate the SIF of a symmetric crack up to about 80% of the wall thickness; and the back surface effect could be a factor in bringing possible error for deeper cracks. It needs to be mentioned that, for the latter two models, previously performed stress analysis for the uncracked body was indispensably adopted and proved its usefulness in fracture analysis.

Due to the complex material nature and various processes that the propellant grain has to go through before firing, possible initial flaws can be generated off the axis of symmetry. In order to provide a relatively complete version of fracture analysis of propellant grain, a series of tests was conducted to investigate the fracture behavior of the off-axis cracks under internal pressure loading. The propagated crack surface was found to be doubly curved in both the depth and length directions, while the growth path of the crack's mid-point seemed to closely follow a predictable direction which was normal to the local maximum principal stress direction. Experimental and numerical methods were demonstrated to be feasible to deliver a reasonable crack growth path prediction based on the knowledge of the local principal stress direction using

photoelasticity and the FEM. The growth in the depth direction enabled the crack to extend into a highly stressed zone and caused the increasing ratio of the pseudo-crack depth to length,  $\frac{a'}{c}$ , for an increasing off-axis angle. The continuous change in growth direction also eliminated the mixed-mode condition experienced by the initial crack and caused the crack to be under Mode I condition thereafter. Furthermore, SIF values that were obtained around the crack border showed a larger variation compared with the symmetric cracks, and the maximum SIF was found to occur either at the surface or the mid-point of the crack with the minimum SIF staying in-between. Also, it seemed that the observed variation increased with the increasing off-axis angle. For deep cracks, the back surface effect was found to be non-negligible and actually elevated the SIF value in the mid-portion of the crack which was close to the outer surface. It seemed that, according to the comparison between the symmetric and off-axis cracks, the uniformity in the SIF distribution was mainly controlled by the off-axis angle and the crack depth whose higher values were expected to bring about more variation to the SIF distribution.

## **5.2 Recommendations and Future Work**

The conducted research was mainly focused on the geometrical effect of the internal star grain on the behavior of a surface crack emanating from the inner boundary of the grain model. As was mentioned earlier, propellant material characterization was regarded as the other major aspect of propellant research. The present trend of material study is directed to formulate more general and realistic constitutive relationships of the material and more closely model the material responses including the failure mechanism under combined loading conditions. Meanwhile, the experimental efforts should also be made to simulate the real processes that the propellant material experiences throughout its entire service life and collected data are believed to be extremely beneficial in forming the analytical models. As the final goal, connections between the geometric and material influences on the propellant grain performance are to be made, which, in addition to the analysis of the interactions among rocket motor components, serves to provide general and reliable design criteria and safety control guidelines for the solid propellant grain.

As far as the extension of the present work is concerned, further investigations in several areas can be initiated. First of all, improvements in more accurately analyzing the photoelastic data can be achieved by employing the new image processing technique to enhance the sensitivity and resolution through fringe multiplication and sharpening, from which more precise photoelastic readings of the fringe locations can be acquired so that the error in evaluating



the final SIF value can be greatly reduced. Secondly, different kinds of grain geometries need to be studied so that the developed models and algorithms can be checked and further improved. Thirdly, further study on the interactions between the propellant grain and the case, especially the behavior of the bonding layer (i.e. the liner), can be conducted based on the *status quo*, and thermal loading ought to be included in the analysis due to the mismatch of the coefficients of thermal expansion among the propellant, the liner and the case. From this study, optimizations of the case including the selection of the material between conventional metals and more recent fiber reinforced composites, and also the configuration including the determination of the stiffeners' locations, are expected to be made to improve the structural integrity of the entire rocket motor. Fourthly, to more closely simulate the real situation, the multi-crack problem ought to be addressed, from which the mutual influences among these cracks can be assessed by comparing those results with their counterparts in the single crack case. Finally, motor grain models made of the real propellant material can be employed in three-dimensional fracture analysis based on the knowledge of the geometric effects and material characterizations. Also, different loading conditions including dynamic and transient loading can be added to expand the areas of considerations. Meanwhile, numerical models can be further improved to include three-dimensional fracture analysis, non-linear viscoelastic material response and complex service and environmental conditions

in tandem with the experimental efforts.

In any sense, the research on solid propellant grain will move towards a more comprehensive and practical direction. The advancing requirements on high performance rockets will inevitably raise new problems that need to be solved, and all the "small" efforts in various fields will form a global blueprint for the entire solid propellant grain design evaluation and application.

## Appendix A: LEFM Theories for Determining Mode I SIF from Photoelastic Data

For a three-dimensional surface crack, Sih and Kassir (60) proved that the stress components in the plane that is perpendicular to both the crack front and the crack surface would take the expressions given in classical two-dimensional LEFM theories:

$$\sigma_{ij} = \frac{K_1}{(2\pi r)^{1/2}} - \sigma_{ij}^0(\theta) \quad i, j = n, z \quad (\text{A.1})$$

where  $\sigma_{ij}$ : near tip in-plane stress

$K_1$ : mode I SIF

$r, \theta$ : polar coordinates with origin at the crack tip

$\sigma^0$ : near tip non-singular stress contribution

$n, z$ : local coordinate system along the crack front (figure A.1)

By expanding equation (A.1), each individual stress component can be written as

$$\sigma_{nn} = \frac{K_1}{(2\pi r)^{1/2}} \cos \frac{\theta}{2} \left( 1 - \sin \frac{\theta}{2} \sin \frac{3\theta}{2} \right) - \sigma^0 \quad (\text{A.1.a})$$

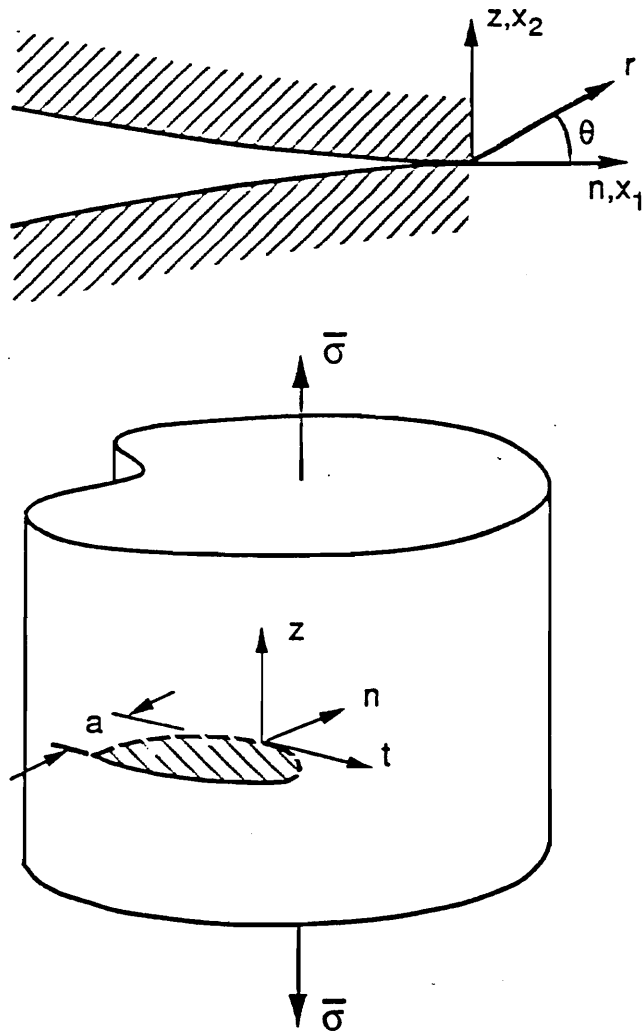


Fig.A.1: Near-tip general problem geometry and notations.

$$\sigma_{zz} = \frac{K_1}{(2\pi r)^{1/2}} \cos \frac{\theta}{2} \left( 1 + \sin \frac{\theta}{2} \sin \frac{3\theta}{2} \right) \quad (\text{A.1.b})$$

$$\sigma_{nz} = \frac{K_1}{(2\pi r)^{1/2}} \sin \frac{\theta}{2} \cos \frac{\theta}{2} \cos \frac{3\theta}{2} \quad (\text{A.1.c})$$

which may yield the in-plane maximum shear stress through the following expression:

$$\tau_{\max}^2 = \frac{1}{4} \left\{ (\sigma_{nn} - \sigma_{zz})^2 + 4\sigma_{nz}^2 \right\} \quad (\text{A.2})$$

After truncating the terms in equation (A.2) and setting  $\theta = \pi/2$ , one can further simplify the form of  $\tau_{\max}$  to:

$$\tau_{\max} = \frac{K_1}{(8\pi r)^{1/2}} + \frac{\sigma^0}{\sqrt{8}} \quad (\text{A.4})$$

If one adopts the following definition

$$(K_1)_{AP} = \tau_{\max} (8\pi r)^{1/2} \quad (\text{A.5})$$

and rearranges equation (A.4), the expression for calculating the SIF,  $K_1$ , can be obtained:

$$(K_1)_{AP} = K_1 + (\pi r)^{1/2} \sigma^0 \quad (\text{A.6})$$

It is seen that the left side of equation (A.6) can be evaluated using the stress-optical law, i.e. equation (2.1), at the locations where the photoelastic data are extracted. Furthermore, if  $K_{AP}$  is plotted against  $r^{1/2}$ , one will obtain the SIF,  $K_1$ , as the interception of the straight line with the y-axis. In fact, the above formulation is based on LEFM theory and one has to identify a linear zone from the photoelastic readings so as to legitimately apply equation (A.6).

Moreover, the normalized SIF can be defined to eliminate the shape effect for planar cracks:

$$K_1(\text{normalized}) = \frac{K_1}{p\sqrt{\pi a}} \times \Phi \quad (\text{A.7})$$

where  $p$ =inner pressure applied to the cylinder

$a$ =crack depth

$$\Phi = \int_0^{\pi/2} \left( \cos^2 \phi + \left( \frac{a}{c} \right)^2 \sin^2 \phi \right)^{1/2} d\phi$$

$\phi$ =elliptic angle of the semi-elliptical surface crack

For a doubly-curved off-axis crack,  $K_1$  can still be normalized by  $p(\pi a')^{1/2}$ . However,  $\Phi$  does not bear the same meaning as it does for a planar crack since the elliptic angle and crack depth are defined differently in the two cases.

## Appendix B: Comments on the Deformation of the Internal Star Grain Model upon Pressurization

It was stated on page 52 that the thinnest section of the grain model experienced the smallest radial displacement, while the thickest part had the largest value. In order to further verify this physical observation and clarify the possible intuitive doubt, the following analytical derivations are presented to prove the radial displacement,  $U_r$ , at point A is larger than that at point B (figure B.1).

It is noted that, from figure 2.6, the fringe order at point A is higher than that at point B, which implies:

$$\tau_{\max}^A > \tau_{\max}^B \quad (\text{B.1})$$

Meanwhile, the principal stresses at both points A and B are the circumferential stress,  $\sigma_{\theta\theta}$ , and the radial stress,  $\sigma_{rr}$  ( $=0$  at the outer boundary), since the shear stress,  $\sigma_{r\theta}$ , is zero in this case. According to the equations (2.2) and (B.1), one can conclude:

$$\sigma_{\theta\theta}^A > \sigma_{\theta\theta}^B \quad (\text{B.2})$$

Using the constitutive relationships in the  $\theta$  direction and the

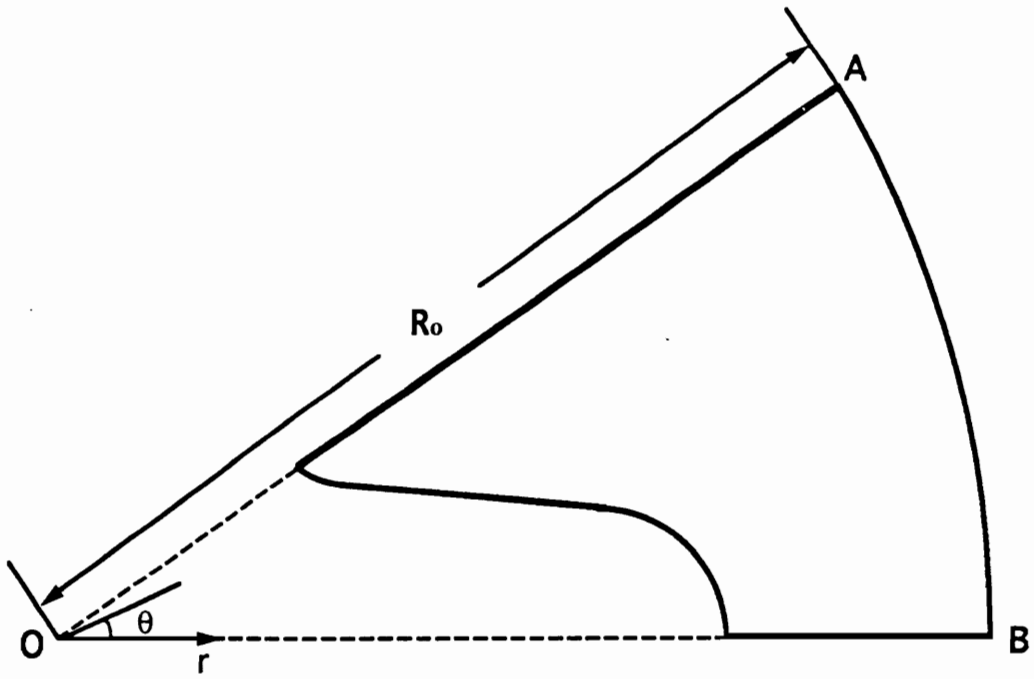


Fig.B.1: Geometry used in the deformation analysis.



z direction

$$\epsilon_{\theta\theta} = \frac{1}{E} (\sigma_{\theta\theta} - \nu(\sigma_{rr} + \sigma_{zz})) \quad (\text{B.3})$$

$$\epsilon_{zz} = \frac{1}{E} (\sigma_{zz} - \nu(\sigma_{rr} + \sigma_{\theta\theta})) \quad (\text{B.4})$$

taking  $\epsilon_{zz}$  to be a constant (based on the plane strain or even generalized plane strain condition occurring in the mid-section of the motor grain model) and noticing  $\sigma_{rr}$  is zero at points A and B, one can come up with

$$\sigma_{zz}|_{A,B} = \nu\sigma_{\theta\theta} + \text{Constant\#1} \quad (\text{B.5})$$

$$\epsilon_{\theta\theta}|_{A,B} = \frac{1-\nu^2}{E} \sigma_{\theta\theta} + \text{Constant\#2} \quad (\text{B.6})$$

Meanwhile, displacement and strain relationship in the polar coordinate system shows:

$$\epsilon_{\theta\theta} = \frac{U_r}{r} + \frac{1}{r} \frac{\partial U_\theta}{\partial \theta} \quad (\text{B.7})$$

which can be simplified to

$$\epsilon_{\theta\theta}|_{A,B} = \frac{U_r|_{A,B}}{R_o} \quad (\text{B.8})$$

at points A and B, since OA and OB shown in figure B.1 are the axes of symmetry.

Combining equations (B.6) and (B.8) yields, at points A and B,

$$U_r|_{A,B} = \frac{(1-v^2)R_0}{E} \sigma_{\theta\theta}|_{A,B} + \text{Constant\#3} \quad (\text{B.9})$$

Finally, comparing equations (B.2) and (B.9), one can easily find

$$U_r^A > U_r^B \quad (\text{B.10})$$

which was shown in figure 2.18.

## References:

- 1) Zucrow, M.J., "*Principles of Jet Propulsion and Gas Turbines*," pp.464-532, New York, John Wiley & Sons, Inc., 1948.
- 2) Warren, F.A., "*Rocket Propellants*," Reinhold Publishing Corp., New York, Chapman & Hall, Ltd., London, 1960.
- 3) Zaehring, A.J., "Propellant Chemistry," *Solid Rocket Technology*, Morton Shorr & Alfred J. Zaehring, Editors, John Wiley and Sons, Inc., 1967.
- 4) Kelley, Frank N., "Solid Propellant Mechanical Properties Testing, Failure Criteria, and Aging," *Propellants Manufacture, Hazards, and Testing*, Robert F. Gould, Editor, American Chemical Society Publications, 1969, pp.188-243.
- 5) Racimor, P. and Nottin, J., "Mechanical Behavior of Solid Propellants During Tensile Test with Variable Temperature," *AIAA Paper 89-2645, AIAA/ASME/SAE/ASEE 25th Joint Propulsion Conference*, Monterey, CA, July 10-12, 1989.
- 6) Saylak, D., "True Stress-Strain Properties for Filled and Unfilled Polymers and Elastomers as Functions of Strain Rate and

- Temperature," *Applied Polymer Symposia*, No.1, 1965, pp.247-260.
- 7) Kruse, R.B., "Laboratory Characterization of Solid Propellant Mechanical Properties," *AIAA Paper No.65-147, AIAA 6th Solid Propellant Rocket Conference*, Washington, D.C., Feb.1-3, 1965.
  - 8) Zak, A.D., "Structural Analysis of Realistic Solid Propellant Materials," *J. of Spacecraft*, Vol.5, No.3, March, 1968, pp.270-275.
  - 9) Meili, G., Dubroca, G., Pasquier, M., and Thepenier, J., "Nonlinear Viscoelastic Design of Case Bonded CMDDB Grains", *J. of Spacecraft*, Vol.18, No.3, May-June, 1981, pp.206-210.
  - 10) Burke, M., Woytowicz, P., and Regqi, G., "A Nonlinear Viscoelastic Constitutive Model for Solid Propellant," *AIAA Paper 90-2213, AIAA/SAE/ASME/ASEE, 26th Joint Propulsion Conference*, July 16-18, 1990, Orlando, FL.
  - 11) Finne, S., Futsaether, C., Botnan, J., and Langtangen, H., "Three-Dimensional Analysis of Solid Propellant Grains Using Nonlinear Viscoelastic Model," *AIAA Paper 90-2090, AIAA/SAE/ASME/ASEE, 26th Joint Propulsion Conference*, July 16-18, 1990, Orlando, FL.
  - 12) Hazelton, I.G., "Effect of Rate and Super-Imposed Pressure on Tensile Properties of Composite Solid Propellant," *Applied*

*Polymer Symposia*, No.1, 1965, pp.217-228.

- 13) Majerus, J.N., and Tamekuni, M., "Effects of Material Nonlinearity and Failure Criteria upon Solid Propellant Integrity," *J. of Spacecraft*, Vol.3, No.3, March, 1966, pp.393-399.
- 14) Zak, A.R., "Structural Failure Criterion for Solid Propellants under Multiaxial Stresses," *J. of Spacecraft*, Vol.5, No.3, March, 1968, pp.265-269.
- 15) Schaeffer, B., "Fracture Criterion for Solid Propellants," *Fracture 1977*, Vol.3, ICF4, Waterloo, Canada, June 19-24, 1977, pp.1145-1151.
- 16) Francis, E.C., "Viscoelastic Rocket Grain Fracture Analysis," *Int. J. of Fracture Mech.*, Vol.10, June, 1974, pp.167-180.
- 17) Kinloch, A.J., and Gledhill, R.A., "Propellant Failure: A Fracture-Mechanics Approach," *J. of Spacecraft*, Vol.18, No.4, July-August, 1981, pp.333-337.
- 18) Chappell, R.N., Jensen, F.R., and Buoton, R.W., "Statistical Service Life Prediction: Minuteman Third Stage Propellant Grain," *J. of Spacecraft*, Vol.5, No.1, Jun, 1968, pp.42-46.
- 19) Schapery, R.A., " A Theory of Crack Initiation and Growth in Viscoelastic Media I: Theoretical Development," *Int. J. of Frac.*, Vol.11, No.1, Feb, 1975, pp.141-158.

- 20) Schapery, R.A., "A Theory of Crack Initiation and Growth in Viscoelastic Media II: Approximate Methods of Analysis," *Int. J. of Frac.*, Vol.11, No.3, June, 1975, pp.369-387.
- 21) Schapery, R.A., "A Theory of Crack Initiation and Growth in Viscoelastic Media III: Analysis of Continuous Growth," *Int. J. of Frac.*, Vol.11, No.4, August, 1975, pp.549-562.
- 22) Schapery, R.A., "Failure Mechanics of Solid Propellants," *Fracture Mechanics, 10th Sym. on Naval Structural Mechanics*, 1978, pp.387-398.
- 23) Schapery, R.A., "A Micro-Mechanical Model for Nonlinear Viscoelastic Behavior of Particle-Reinforced Rubber with Distributed Damage," *Engineering Frac. Mech.*, Vol.25, 1986, pp.845-867.
- 24) Swanson, S.R., "Application of Schapery's Theory of Viscoelastic Fracture to Solid Propellant," *J. of Spacecraft*, Vol.13, No.9, Sept., 1976, pp.528-533.
- 25) Scippa, S., "Propellant Grain Design," AGARD-LS-150, *Design Methods in Solid Rocket Motors*, 1987.
- 26) Zeller, B., "Solid Propellant Grain Design," AGARD-LS-150, *Design Methods in Solid Rocket Motors*, 1987.
- 27) Thrasher, D.I., "State of the Art of Solid Propellant Rocket Motor Grain Design in the United States," AGARD-LS-150, *Design*

*Methods in Solid Rocket Motors*, 1987.

- 28) Sutton, G.P., "*Rocket Propulsion Elements: An Introduction to the Engineering of Rockets*," 5th Edition, John Wiley and Sons, 1986.
- 29) Durelli, A.J., "Experimental Strain and Stress Analysis of Solid Propellant Rocket Motors," *Proceedings of the 4th Symposium on Naval Structural Mechanics*, A.C. Eringen et. al., Editors, April 19-21, 1965, pp.381-442.
- 30) Rastrelli, L.U. and DeHart, R., "Measurements of Strains in Solid Propellant Grains," *20th Meeting Bull., JANNAF*, Vol.II, Nov, 1961.
- 31) Wilson, H.B., Jr., "Stresses Owing to Internal Pressure in Solid Propellant Rocket Grain," *ARS Journal*, Vol.31, No.3, March, 1961, pp.309-317.
- 32) Sampson, R.C. and Campbell, D.M., "Contribution of Photoelasticity to Evaluation of Solid Propellant Motor Integrity," *AIAA Paper, No. 65-190, 6th Solid Propellant Rocket Conference*, Washington, D.C., Feb.1-3, 1965.
- 33) Messner, A.M. and Schliessmann, D.R., "Transient Thermal Stresses in Solid-Propellant Grains," *J. of Spacecraft*, Vol.2, No.4, July-Aug., 1965, pp.565-570.
- 34) Braswell, D.W., Ranson, W.F., and Swinson, W.F., "Scattered Light Photoelastic Thermal Stress Analysis of a Solid-Propellant

- Rocket Motor," *J. of Spacecraft*, Vol.5, No.12, Dec., 1968, pp.1411-1416.
- 35) Dicken, G.M. and Thacher, J.H., "Shear Strain Measurement in Solid Propellant Rocket Motors," *J. of Spacecraft*, Vol.2, No.5, Sept.-Oct., 1965, pp.765-769.
- 36) Jana, M.K., Renganathan, K., and Rao, G.V., "Effect of Geometric and Material Nonlinearities on the Propellant Grain Stress Analysis," *J. of Spacecraft*, Vol.25, No.4, July-Aug, 1988, pp.317-320.
- 37) Francis, E.C., Lindsey, G.H., and Parmerter, R.R., "Pressurized Crack Behavior in Two-dimensional Rocket Motor Geometries," *J. of Spacecraft*, Vol.9, No.6, 1972, pp.415-419.
- 38) Francis, E.C. and Jacobs, H.R., "Fracture Considerations for Surveillance Programs," *J. of Spacecraft*, Vol. 13, No.8, August, 1976, pp.451-455.
- 39) Hoffman, T. and Laheru, K., "Propellant Failure Analysis Using Scanning Electron Microscope," *AIAA Paper 89-2647, AIAA/ASME/SAE/ASEE 25th Joint Propulsion Conference, Monterey, CA, July 10-12, 1989.*
- 40) Liu, C.T., "Evaluation of Damage Fields Near Crack Tips in a Composite Solid Propellant," *J. of Spacecraft*, Vol.28, No.1, Jan-Feb, 1991, pp.64-70.



- 41) Willoughby, D.A., "Heat Conduction in Star-Perforated Solid Propellant Grains," *J. of Spacecraft*, Vol.2, No.2, March-April, 1965, pp.239-243.
- 42) Krishnan, S., "Design of Neutral Burning Star Grain," *J. of Spacecraft*, Vol.12, No.1, Jan., 1975, pp.60-62.
- 43) Messner, A.M., "Final Report on Integrated Structural and Ballistic Design Curves for Star-Perforated Propellant Grains," *AFGPL-TR-70-106*, Oct., 1970.
- 44) Brooks, W.T., "Ballistic Optimization of the Star Grain Configuration," *AIAA 80-1136R, J. of Spacecraft*, Jan., 1982, pp.54-59.
- 45) Wang, L., "Investigations into Deep Cracks in Rocket Motor Propellant Models," M.S. Thesis, VPI&SU, Oct., 1990.
- 46) Dally, J.W. and Riley, W.F., "*Experimental Stress Analysis*," McGraw-Hill, Inc., 2nd Edition, 1978, pp.459-467.
- 47) Epstein, J.S., Post, D., and Smith, C.W., "Three-Dimensional Photoelastic Measurements with Very Thin Slices," *Experimental Techniques*, Dec., 1984, pp.34-37.
- 48) Smith, C.W. and Wang, L., " Stress Intensity Distributions around Surface Flaws in Motor Grain Geometries," *Symposium on Experimental Mechanics of Fracture*, K.S. Kim, Organizer, Joint FEFG/ICF International Conference on Fracture of Engineering

*Materials and Structures*, Singapore, 1991, pp.69-74.

- 49) Newman, J.C. and Raju, I.S., "Stress Intensity Factors for Internal and External Surface Cracks in Cylindrical Vessels," *J. of Pressure Vessel Technology*, Vol.104, Nov., 1982, pp.293-298.
- 50) Orange, T.W., "Crack Shapes and Stress Intensity Factors for Edge-Cracked Specimens," *ASTM STP513*, Part I, pp.71-78.
- 51) Jones, A.T., " A Radially Cracked Cylindrical Fracture Toughness Specimen," *J. of Engr. Frac. Mech.*, Vol.16, 1974, pp.435-446.
- 52) Bowie, O.L. and Freese, C.E., "Elastic Analysis of a Radial Crack in a Circular Ring," *J. of Engr. Frac. Mech.*, Vol.4, 1972, pp.315-321.
- 53) Murakami, Y., Tsuru, H., and Sakamoto, K., "Stress Intensity Factors for Small Surface Cracks at the Site of Stress Concentrations," *J. Soc. Mater. Sci., Japan*, Vol.35, No.396, 1986, pp.998-1003.
- 54) Post, D., "Fringe Multiplication in Three-Dimensional Photoelasticity," *J. of Strain Analysis*, Vol.1, No.5, 1966, pp.380-388.
- 55) Tardy, M.H.L., "Methode Pratique Déxzmen de Mesure de la Birefringence des Verres D'optique," *Rev. Opt.*, Vol.18, 1929.
- 56) Smith, C.W., "Analytical and Experimental Studies of the Surface

- Flaw," *Experimental Mechanics*, June, 1988, pp.194-200.
- 57) Cotterell, B. and Rice, J.R., "Slightly Curved or Kinked Cracks," *Int. J. of Frac.*, Vol.16, No.2, April, 1980, pp.155-169.
- 58) Smith, C.W., Peters, W.H., Hardrath, W.T., and Fleischman, T.S., "Stress Intensity Distributions in Nozzle Corner Cracks of Complex Geometry," *VPI-E-79-2, NUREG/CR-0640, ORNL/SUB/7015-2*, Jan., 1979, 33pp.
- 59) Smith, C.W., "Experimental Methods for the Determination of the Stress Intensity Factor," *Special Issue on Fracture Mechanics (dedicated to Prof. G.R. Irwin), Journal of the Aeronautical Society of India*, August, 1984, pp.173-191.
- 60) Sih, G.C. and Kassir, M., "Three Dimensional Stress Distribution around an Elliptical Crack under Arbitrary Loading," M.K., *J. of Appl. Mech.*, Vol.33, 1966, pp.601-611.

## Vita

The author was born on June 5, 1967 in Shanghai, China to Pei-fang Zhu and Zheng-guo Wang. He spent his first 21 years mainly in Beijing, Chongqing and Shanghai to finish his schooling until he received his B.S. degree in Applied Mechanics from Fudan University. He came to the United States in 1988 to further his graduate study in Engineering Science and Mechanics Department at Virginia Polytechnic Institute and State University (VPI&SU) first as a M.S. student. Upon the completion of his M.S. degree under the guidance of Prof. C.W. Smith in 1990, the author decided to continue his Ph.D. study so as to get a broader and clearer view of the attractive and mysterious scientific world.

For the past four years, the author's major research interests have been focused on fracture mechanics and its applications in engineering problems, especially the failure analysis of solid rocket propellants. The author is working on exploring more applications of fracture mechanics on various kinds of materials by using different techniques, including both experimental and numerical methods, among which three-dimensional fracture problems, macro and micro mechanics failure analysis and environmental effects on material fracture behavior are the main issues to be studied in the near future. After graduation, the author plans to stay at VPI&SU as a research associate and get prepared for the professional career.

